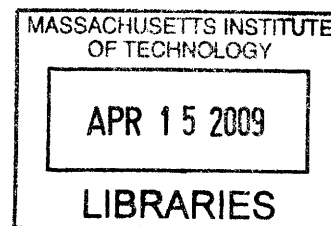


Advances in Targeted Chemotherapy using MRI-guided Focused Ultrasound to Disrupt the Blood-Brain Barrier

by

Lisa Hsu Treat

B.S. Physics, French
Dickinson College, 2000



ARCHIVES

Submitted to the Division of Health Sciences and Technology
in Partial Fulfillment of the Requirements for the Degree of

Doctor of Philosophy in Nuclear Science and Medical Engineering

at the

MASSACHUSETTS INSTITUTE OF TECHNOLOGY


February 2009

© 2009 Massachusetts Institute of Technology. All rights reserved.

Signature of Author:

Harvard-MIT Division of Health Sciences and Technology
October 28, 2008

Certified by:

 Kullervo Hynynen, Ph.D.
Professor of Medical Biophysics, University of Toronto
Director of Imaging Research, Sunnybrook Health Sciences Centre
Thesis Supervisor

Accepted by:

Ram Sasisekharan, Ph.D.
Edward Hood Taplin Professor of Health Sciences and Technology
Director, Harvard-MIT Division of Health Sciences and Technology

Advances in Targeted Chemotherapy using MRI-guided Focused Ultrasound to Disrupt the Blood-Brain Barrier

by

Lisa Hsu Treat

Submitted to the Division of Health Sciences and Technology
on October 28, 2008 in Partial Fulfillment of the
Requirements for the Degree of Doctor of Philosophy in
Nuclear Science and Medical Engineering

ABSTRACT

The clinical application of chemotherapy to brain malignancies has been severely limited because many potential therapeutic agents are typically unable to penetrate the blood-brain barrier (BBB). A novel approach to overcome this barrier uses focused ultrasound to induce localized BBB disruption in a targeted region of the brain and magnetic resonance imaging (MRI) to guide and monitor the procedure. The purpose of this thesis was to develop a technique using MRI-guided focused ultrasound for trans-BBB drug delivery applications.

This thesis demonstrates that MRI-guided focused ultrasound can be used to achieve consistent and reproducible BBB disruption without invasive craniotomy in rats, to enable doxorubicin to accumulate in normal brain at clinically therapeutic levels, and to increase the antitumoral efficacy of doxorubicin in a rodent model of aggressive glioma. Using a microbubble-based ultrasonographic contrast agent, focal BBB opening was consistently achieved using transcranial focal pressures of 1.2 MPa or greater; locations in the posterior brain exhibited consistent BBB disruption with applied focal pressures of 0.8 MPa or greater. When combined with systemic administration of liposomal doxorubicin, we achieved local drug concentrations of 900 ± 300 ng/g tissue in the brain with minimal tissue effects, and up to 5400 ± 700 ng/g tissue with more significant tissue damage, while accumulation in non-targeted contralateral brain tissue remained significantly lower ($p < 0.001$). In addition, MRI signal enhancement in the sonicated region correlated strongly with doxorubicin concentration in tissue ($r = 0.87$), suggesting that contrast-enhanced MRI may provide useful feedback on drug penetration. Finally, glioma-bearing rats treated with ultrasound-enhanced chemotherapy exhibited significantly longer median survival times (31 versus 25 days; $p = 0.0007$) and slower tumor growth (average tumor volume doubling time, 3.7 ± 0.5 days, versus 2.3 ± 0.3 days) than nontreated rats; rats which received standard intravenous chemotherapy showed no significant difference in survival or tumor growth rate. In sum, this thesis research provides pre-clinical data toward the development of MRI-guided focused ultrasound as a noninvasive method for the delivery of agents such as doxorubicin across the BBB to treat patients with diseases of the central nervous system.

Thesis Supervisor: Kullervo Hynynen

Title: Professor of Medical Biophysics, University of Toronto

ACKNOWLEDGMENTS

I would like to thank my thesis advisor, Kullervo Hynynen, for his extraordinary support and patience throughout my graduate career. The past six years have been filled with ups and downs, and he has been there for me every step of the way. His wisdom, compassion, and renowned uncanny insight have contributed immeasurably to my growth as a scientist and as a person. I am also indebted to Nathan McDannold, for his patience, guidance, and hands-on mentorship, and to Fred Bowman and Jacquelyn Yanch, for their invaluable input and constant encouragement.

It has been a great pleasure to conduct my thesis research as a member of the Focused Ultrasound Laboratory at the Brigham and Women's Hospital. I am grateful to all its current and former members and affiliates, who define its spirit and sense of community. I am especially grateful to Yongzhi Zhang, Natalia Vykhodtseva, Karen Tam, Scott Raymond, Randy King, and Sue Agabian, for their contributions to this thesis research; to Greg Clement, Jason White, and Caleb Farny (aka the Peanut Gallery), for their entertaining antics; to Subha Maruvada, Krisztina Fisher, Shipra Sharma, and Keiko Fujiwara, for their moral support; and to Sham Sokka, for introducing me to the lab.

My graduate experience has been defined by the love and support of the close-knit community built by the Harvard-MIT Division of Health Sciences and Technology. Too many to list, I credit all my friends and mentors in HST for helping me to find my place when I first arrived at MIT and for giving me the strength to carry through to the end. I have found ardent supporters in Cathy Modica, Randy Gollub, Valerie Pronio-Stelluto, and Caroline Boudoux, who have collectively taught me both to accept who I am and to aspire to be more. It has truly been my honor and privilege to be a part of the HST family.

I thank my friends in the MIT Nuclear Science and Engineering Department, Rachel Batista, Yoonsun Chung, Jeongik Lee, Heongpil Ham, Xiaofeng Qian, John Bernard, and Jeff Coderre, for their support, especially during my early graduate years.

The journey that led me to this point began long before I set foot in Cambridge. I would like to thank my undergraduate mentors, Charles Bloch, John Luetzelschwab, Hans Pfister, Priscilla Laws, and Ken Laws, for their guidance and faith in me.

I am grateful to all the individuals and organizations whose financial and material support made this work possible, including the National Institutes of Health, through grants #R01EB003268 and #U41RR019703; the National Institute of Biomedical Imaging and Bioengineering, through the Medical Engineering and Medical Physics Neuroimaging Training Program funded by grant #5T32EB001680; and MIT, through graduate research fellowships from the Whitaker Health Sciences Fund and from HST. Additional funding was provided by a gift from the Brudnick family, and cell cultures were provided by the University of California–San Francisco/Neurosurgery Tissue Bank.

Finally, I thank all my family and extended families – the Hsus, Wangs, Treats, Grants, Martis, and Benezeches – for their continued love and support. I dedicate this thesis to my mother, Helen Hsu, who has made me everything I am and will be, and to my husband, Adam Treat, whose unconditional love gives me hope for tomorrow.

TABLE OF CONTENTS

List of Figures.....	8
List of Tables	9
Abbreviations	10
1 Introduction.....	11
1.1 Motivation	11
1.2 The Blood-Brain Barrier	15
1.2.1 Role.....	15
1.2.2 History	15
1.2.3 Blood supply to the brain.....	16
1.2.4 Physiology	16
1.2.4.1 Physical barrier.....	17
1.2.4.2 Enzymatic barrier	18
1.2.4.3 Efflux barrier.....	18
1.2.5 Endogenous transport across the BBB.....	19
1.2.5.1 Free diffusion of small molecules	19
1.2.5.2 Catalyzed transport of small or large molecules	19
1.2.6 Strategies for drug delivery to the brain	20
1.2.6.1 Catheter-based BBB disruption.....	20
1.2.6.2 Pharmacological modification.....	22
1.2.6.3 Other nonvascular routes to CNS drug delivery	24
1.3 Focused Ultrasound (FUS).....	26
1.3.1 Background.....	26
1.3.2 History of therapeutic ultrasound in the brain	28
1.3.2.1 Development of ultrasound applications through the skull.....	29
1.3.2.2 Development of targeting and monitoring methods.....	30
1.3.3 Ultrasound-induced BBB disruption	31
1.3.3.1 BBB disruption using ultrasound alone.....	31
1.3.3.2 Microbubble-enhanced ultrasound for BBB disruption	32
1.3.3.3 Physical mechanisms.....	34
1.3.3.4 Biological mechanisms	35
1.4 Doxorubicin (DOX)	37
1.4.1 Clinical use	37
1.4.2 Mechanism of action.....	38
1.4.3 Spectroscopy.....	39
1.5 Scope of this thesis	41
2 Materials and Methods.....	43
2.1 Animals and Equipment	43
2.1.1 Animals.....	43
2.1.2 Ultrasound	44
2.1.2.1 Transducer	44
2.1.2.2 Transducer characterization	44
2.1.2.3 Transducer calibration.....	45

Table of Contents

2.1.2.4	Derated measurements accounting for energy losses in bone and tissue ..	46
2.1.3	Experimental set-up	49
2.1.4	Magnetic resonance imaging	50
2.1.5	Fluorometry	51
2.2	Blood-brain barrier disruption using transcranial MRI-guided focused ultrasound.....	53
2.2.1	Sonications.....	53
2.2.2	Image analysis	54
2.2.3	Trypan blue staining	54
2.2.4	Histologic analysis.....	54
2.3	Targeted delivery of doxorubicin to normal brain by ultrasound-mediated blood-brain barrier disruption	55
2.3.1	Chemotherapy.....	55
2.3.2	Ultrasound	55
2.3.3	Fluorometric assay	57
2.3.3.1	Extraction and quantification of doxorubicin.....	57
2.3.4	Statistical analysis.....	58
2.3.5	Effect of microbubble concentration on DOX delivery to the brain	58
2.3.6	Histologic analysis.....	59
2.3.7	Fluorescence imaging	60
2.4	Therapeutic efficacy of ultrasound-enhanced chemotherapy in a rodent model of aggressive glioma	61
2.4.1	Cell culture	61
2.4.2	Tumor implantation	61
2.4.3	Study design	62
2.4.4	Sonications.....	63
2.4.5	Chemotherapy.....	64
2.4.6	Magnetic resonance imaging	64
2.4.7	Image analysis	66
2.4.8	Survival analysis.....	66
2.4.9	Histologic analysis.....	67
3	Blood-brain barrier disruption using transcranial MRI-guided focused ultrasound	68
3.1	Results	68
3.1.1	Visual confirmation of ultrasound-induced BBB disruption.....	68
3.1.2	Threshold response of ultrasound-induced BBB disruption.....	68
3.1.3	Variations in sensitivity to ultrasound-induced BBB disruption by anatomical location in the brain	70
3.1.4	MRI guidance of ultrasound-induced BBB disruption	71
3.1.5	Histologic results	72
3.2	Discussion	74
4	Targeted delivery of doxorubicin to normal brain by ultrasound-mediated blood-brain barrier disruption	77
4.1	Results	77
4.1.1	Therapeutic Levels of Doxorubicin Delivered to the Rat Brain	77
4.1.2	Correlation of MRI signal enhancement and DOX delivery	79
4.1.3	Histologic findings.....	80
4.1.4	Distribution of DOX revealed by fluorescence images	83
4.2	Discussion	85

5 Therapeutic efficacy of ultrasound-enhanced chemotherapy in a rodent model of aggressive glioma.....	87
5.1 Results	87
5.1.1 Improved survival in rats with implanted glioma after treatment with ultrasound-enhanced chemotherapy.....	87
5.1.2 Delayed tumor growth in rats with implanted glioma after treatment with ultrasound-enhanced chemotherapy	89
5.1.3 Histologic findings.....	91
5.2 Discussion	94
6 Conclusions and recommendations for future work	97
6.1 Conclusions	97
6.2 Recommendations for future work.....	104
7 References	107

LIST OF FIGURES

Figure 1-1: Correlation of intratumoral DOX concentration and patient response rate.	37
Figure 1-2: Fluorescence spectra for doxorubicin in aqueous solution.	40
Figure 2-1: Characteristic beam plots for the 1.7-MHz transducer.	45
Figure 2-2: Comparison of beam plots with and without rat skull in beam path.	48
Figure 2-3: Diagram of the experimental set-up.	50
Figure 2-4: Calibration curves for fluorometric measurements of doxorubicin concentration	52
Figure 2-5: Schematic of ultrasound protocol (freq = 1.7 MHz) used to deliver doxorubicin to the rat brain at human therapeutic levels.	57
Figure 2-6: Contrast-enhanced T1-weighted magnetic resonance images of the rat brain before (left) and after (right) ultrasound-induced BBB disruption around the tumor (arrows)	65
Figure 3-1: Confirmation of ultrasound-induced localized BBB disruption in the rat brain by MRI and by trypan blue	69
Figure 3-2: Threshold of BBB disruption induced by transcranial focused ultrasound.	70
Figure 3-3: Location dependence of threshold for ultrasound-induced BBB disruption.	71
Figure 3-4: Normalized MRI signal enhancement (mean \pm SD) in the sonicated region after injection of MR contrast agent as a function of pressure amplitude.....	72
Figure 3-5: H&E-stained rat brain exposed in 4 focal locations to pressure amplitudes ranging from 0.5 MPa to 1.7 MPa.	73
Figure 4-1: Concentration of DOX delivered to the brain as a function of Optison dose.	78
Figure 4-2: Correlation of MRI signal enhancement and DOX delivered to the targeted brain parenchyma.....	80
Figure 4-3: Transversal H&E-stained sections of rat brains harvested 4 h after sonication with 0.1, 0.2, or 0.5 mL/kg Optison injections	81
Figure 4-4: Transversal H&E-stained sections of brains of rats sacrificed 1 week after treatment with FUS+DOX	82
Figure 4-5: Fluorescence images showing localized distribution of DOX in sonicated region of rat brain.....	84
Figure 5-1: Fraction of survival (Kaplan-Meier plot) of rats with intracranially implanted 9L gliosarcoma after treatment	88
Figure 5-2: T2-weighted magnetic resonance images of a rat brain with implanted 9L gliosarcoma (outlined) before and 1, 2, and 3 weeks after treatment with focused ultrasound and i.v. liposomal doxorubicin (FUS+DOX; top row) or treatment with i.v. liposomal doxorubicin (DOX only; bottom row).	90
Figure 5-3: Average tumor volume doubling time in rats with intracranially implanted 9L gliosarcoma after treatment	91
Figure 5-4: H&E-stained histologic sections of rat brains implanted with 9L gliosarcoma, harvested 48 h after treatment.....	93

LIST OF TABLES

Table 2-1: Acoustic efficiency of air-backed single-element transducer.	46
Table 2-2: Experimental parameters for ultrasound-mediated delivery of doxorubicin to the normal rat brain.....	56
Table 4-1: Mean doxorubicin concentration (ng/g tissue) accumulated in sonicated and control brain tissue	78

ABBREVIATIONS

BBB	blood-brain barrier
deg C	degree Centigrade
cm	centimeter
CNS	central nervous system
CT	computed tomography
Da	Dalton, unit of molecular weight
DOX	doxorubicin
ETL	echo train length
FA	flip angle
FOV	field of view
FSE	fast spin echo
FUS	focused ultrasound
g	gram
h	hour
Hz	Hertz, unit of frequency
i.p.	intraperitoneal
i.v.	intravenous
m	meter
MHz	megaHertz, unit of frequency
min	minute
mg	milligram
μ L	microliter
mL	milliliter
μ m	micrometer (micron)
mm	millimeter
MPa	megaPascal, unit of pressure
MRI	magnetic resonance imaging
ms	millisecond
NEX	number of excitations
Pgp	P-glycoprotein
Np	Neper, natural logarithmic unit of ratio
ppm	part per million
RARE	rapid acquisition with relaxation enhancement
RF	radio frequency
ROI	region of interest
s	second
SD	standard deviation
T	Tesla, unit of magnetic field strength
TE	echo time
TJ	tight junction
TR	repetition time
W	Watt, unit of power

1 Introduction

1.1 Motivation

With all the scientific and medical advances over the last century, the brain remains one area of which our understanding has advanced greatly but our ability to treat has been sluggish. While imaging and diagnostics have grown by leaps and bounds, the evolution of therapeutic interventions in the central nervous system (CNS) has not enjoyed such rapid progress. Current standard clinical approaches to malignant brain tumors, including surgical resection in combination with radio- and/or chemotherapy, have met with limited success (1). Many other neurological or neurodegenerative disorders do not yet have effective therapies, despite the rapid growth of the pharmaceutical industry in recent years.

One major reason for the apparent bottleneck is the presence of the blood-brain barrier (BBB). Formed by the endothelial cells that line the microvasculature of the brain, the BBB prevents the entry of most blood-borne substances into the CNS. Its selective permeability, based on lipid solubility, molecular size, and charge, protects the brain from potential toxins but also limits the access of many prospective therapeutics (2). Potential therapeutic agents are prohibited from passing from systemic circulation into brain parenchyma (3, 4) or are unable to accumulate at sufficient therapeutic concentrations (5). Although tumor vasculature is often malformed and the integrity of its BBB compromised, the complex problem of drug delivery to the brain persists. Because systemic chemotherapeutic agents are not able to penetrate solid tumors homogeneously (6), portions of the tumor are often left untreated or partially treated after traditional

intravenous chemotherapy. Additionally, malignant cells may infiltrate the margin beyond the visible tumor where the BBB is intact. Invisible to the surgeon and unreachable by pharmacological interventions, these infiltrating cells are to blame in 78-90% of cases of recurrent glioma (7, 8). Thus, the BBB remains a formidable obstacle in the treatment of patients with brain malignancies. Even with aggressive surgical resection and radiotherapy, the prognosis for the most common and most aggressive form of glioma in adults is associated with a median survival of less than one year from the time of diagnosis (1, 9).

Current strategies to circumvent the BBB are less than ideal. Methods of diffuse BBB disruption allow widespread cytotoxic drug penetration to non-targeted brain tissue (10) and can thus have dose-limiting side effects. Other methods which provide localized drug delivery may increase the drug concentration at the target location while reducing systemic toxicity effects, but they typically require invasive, high-risk neurosurgical procedures (11, 12).

A novel approach to the problem of drug delivery to the brain uses focused ultrasound to temporarily disrupt the BBB in a noninvasive and localized manner (13). High-frequency acoustic energy penetrates soft tissue to induce effects deep below the surface, thus allowing a noninvasive approach to therapy. When applied to the brain in the presence of gas-filled microbubbles, ultrasound has been shown to stimulate active vesicular transport and transiently disassemble tight junctional complexes to allow the passage of molecules which would not otherwise penetrate the BBB (14, 15). As the energy is tightly focused to diameters as small as <1 mm, its effects on the BBB can be confined to a limited volume of tissue to enable targeted therapy (16-18). The high spatial

resolution and noninvasive nature of ultrasound-induced BBB disruption make it an advantageous technique for targeted drug delivery to the brain. In addition, the use of magnetic resonance imaging (MRI) to guide and monitor the procedure enables precise targeting and repeated application without ionizing radiation. Trans-BBB delivery by MRI-guided focused ultrasound has now been demonstrated for numerous agents, including liposomal doxorubicin (17), imaging fluorophores (19), Herceptin (16), Alzheimer's disease immunotherapeutics (20), and other antibodies (21).

Focused ultrasound-induced BBB disruption addresses the limitations of other drug delivery methods and shows great potential to have a positive impact on patients with a variety of neurological disorders. However, further evidence of the therapeutic benefit of ultrasound-enhanced trans-BBB chemotherapy is needed to advance this technology toward clinical trials. Doxorubicin (DOX) is a prime candidate with which to demonstrate the therapeutic potential of ultrasound-mediated trans-BBB drug delivery. It is a highly effective cytotoxic agent with ubiquitous clinical use in the treatment of a wide range of cancer types, but because it does not readily penetrate the intact BBB, it is typically ineffective in treating intracranial lesions. Cancer patients who demonstrate partial or complete response to DOX chemotherapy for extracranial lesions may no longer enjoy such positive results if their lesions metastasize to the brain. Even in high-grade brain tumors, in which the vasculature is abnormally permeable, the BBB often prevents cytotoxic levels of DOX from being achieved in glioma tissue and in intracranial metastases (5). If DOX were allowed to accumulate at sufficient concentrations in the brain, its clinical impact on the treatment of patients with both primary and metastatic tumors could be significant. To advance the development of MRI-

guided focused ultrasound for targeted drug delivery applications in the brain, this thesis aimed to develop a protocol using MRI-guided focused ultrasound for the targeted delivery of doxorubicin to the brain and to demonstrate its therapeutic impact in a disease model.

1.2 The Blood-Brain Barrier

1.2.1 Role

Comprised of the brain and spinal cord, the central nervous system (CNS) needs a chemically stable environment to function properly. Neurons communicate through the propagation of action potentials induced by the flow of ions into and out of the cells. In the brain, their complex synaptic connections require that the surrounding extracellular concentrations of sodium, potassium, and calcium be maintained within a very narrow range. The hypersensitivity of neurons to the ionic balance of their environment necessitates a mechanism of strict regulation of access to the brain microenvironment from the vascular compartment. Such regulation exists in the form of the blood-brain barrier (BBB). The BBB is a selectively permeable barrier between the brain parenchyma and its blood supply. It regulates ionic balance within the brain and facilitates the transport of nutrients from systemic circulation, while protecting the brain from potentially harmful blood-borne molecules, which may otherwise be innocuous in the peripheral organ system (4, 22).

1.2.2 History

The restrictive permeability of the brain was first observed by Paul Ehrlich in 1885. While studying staining in animals, he discovered that some injected dyes diffused rapidly into most organs, whereas the brain showed very little uptake. His student Edwin Goldmann further observed in 1913 that a dye injected directly into the surrounding cerebrospinal fluid (CSF) was contained within the CNS, while the rest of the body remained unstained (23). These observations provided the first documented evidence of a

barrier which separates the cerebral microenvironment from its vasculature. Lina Stern later proposed the existence of a “hemato-encephalic barrier” in 1921 (24).

Electron microscopy studies in the 1960’s helped to elucidate the physical structure of the BBB. They revealed that the actual barrier lay in the endothelial lining of the brain (25). It is now recognized that the BBB is just one of several blood-CNS barriers. Other blood barriers include the blood-CSF barrier and the blood-spinal cord barrier (26, 27).

1.2.3 Blood supply to the brain

The brain is perfused by an extremely dense and extensive microvascular network. Virtually all neurons and supporting glial cells are within 20 microns of a capillary so that nutrients and oxygen carried by the blood can be delivered to the brain in a quick and efficient manner. Since each brain cell has an almost direct connection to the circulatory system, the vascular route would be an extremely effective way to deliver an agent to the brain, if the molecule were able to enter the brain from circulation. However, the presence of the BBB makes it very difficult for all but a few molecules to do so (28).

1.2.4 Physiology

Multiple mechanisms contribute to the functionality of the BBB. The primary mechanism is the physical barrier between the blood and the brain’s extracellular space formed by the endothelial lining of the brain microvasculature. In addition, capillary pericytes directly adjacent to the endothelium share a common basement membrane with the endothelium and help to regulate endothelial metabolism. Astrocytes, one type of glial cell, have extensions of the main cell body which terminate on the vessel wall,

called foot processes; they both provide structural support and contribute to BBB regulation (29). A secondary defense, in the form of an enzymatic barrier, serves to inactivate drugs that may be able to passively diffuse through the endothelial cells. In addition, an active efflux barrier causes many penetrating molecules to be transported from the brain back into the blood. This multifunctionality of the BBB ensures that the neuronal and glial environment is kept stable and that entry into the brain parenchyma is strictly enforced (10).

1.2.4.1 Physical barrier

Endothelial cells which line the capillary walls serve as the physical interface between the brain parenchyma and its blood supply. Unlike the loosely connected endothelial cells of capillaries in peripheral organs, endothelial cells in brain capillaries are tightly connected to each other by specialized proteins which form intercellular tight junctions. Tight junctions are complexes of transmembrane proteins expressed by endothelial cells and perivascular glia, including junctional adhesion molecules (30), occludins (31), and claudins (32). Characterized by very high electrical resistance, on the order of 1000 Ohms/cm², which is several orders of magnitude higher than intercellular resistance of endothelial cells outside of the brain, tight junctions play a primary role in forming the highly impermeable physical barrier of the BBB (33). Because the gaps between the endothelial cells are well-occluded by the tight junctions, the paracellular pathway across the endothelium is blocked in the brain.

The transcellular pathway across the endothelium is likewise severely limited in brain capillaries in comparison to peripheral capillaries. Pinocytosis, a process by which molecules are enveloped within a vesicle and transported across the endothelial cell

membrane, is markedly reduced in the brain microvasculature, making it more difficult for nonspecific molecules to diffuse freely across its membrane into the brain parenchyma (34). As molecules can neither pass between nor through the endothelial cells of the blood vessel wall due to the combination of the high-resistance endothelial tight junctions and the restricted pinocytosis, these components both contribute to the physical barrier of the BBB.

1.2.4.2 Enzymatic barrier

The endothelial cells produce a variety of enzymes which inactivate or degrade molecules that are able to get past the physical barrier of the endothelial cells. In addition, neighboring pericytes and astrocytic foot processes also produce such enzymes to contribute to the functionality of the BBB (22, 35, 36). Conversely, the brain also produces specialized enzymes which activate molecules that would otherwise be inactive in the brain. For example, L-DOPA is an amino acid used in the treatment of Parkinson's disease which is inactive in the peripheral blood system but which is converted to its pharmacologically active form, dopamine, once it crosses the BBB (34).

1.2.4.3 Efflux barrier

A third mechanism exists for the undesired influx molecules which may penetrate the other barrier mechanisms. The endothelial cells, pericytes, and astrocytic foot processes of the BBB also produce efflux transporter proteins to escort undesired molecules out of the brain. If a molecule which enters the brain from the blood happens to be a substrate for one of the many active efflux proteins, it will bind to its transporter counterpart and be carried across the endothelial cell membrane back into the vascular compartment. P-glycoprotein (Pgp) is one particularly effective efflux pump which acts

on multiple substrates and is highly active on the interior (luminal) plasma membrane of the capillary endothelium (37). Its location, multispecificity, and potency make Pgp a critical barrier to therapeutic drug entry into the CNS, and its overexpression in tumor cells confers multidrug resistance (38, 39).

1.2.5 Endogenous transport across the BBB

Selective transcellular access to the brain for circulating molecules is possible via one of two transport mechanisms: free diffusion of small molecules or catalyzed transport of small or large molecules.

1.2.5.1 Free diffusion of small molecules

Certain small molecules are able to cross BBB by free diffusion across the phospholipid bilayer of the endothelial wall. In order to freely diffuse through the endothelial cell membrane, molecules must meet stringent criteria, based on size, charge, and lipid solubility. In general, molecules must be neutral, lipid-soluble, and less than 400-500 Dalton in molecular mass to be able to enter the brain parenchyma from circulation by passive diffusion (2, 28, 34).

1.2.5.2 Catalyzed transport of small or large molecules

Endogenous transport mechanisms exist to accelerate the passage of certain essential molecules which do not meet the criteria for free diffusion through the endothelial wall. Small water-soluble vitamins and nutrients, such as glucose and neutral amino acids, are brought into the brain from circulation through carrier-mediated transport. For certain large-molecule peptides or plasma proteins, receptors present on the endothelial cell membrane recognize specific molecules, such as insulin, leptin, and

transferrin, which are transported through the endothelial cytoplasm by receptor-mediated transcytosis (10).

1.2.6 Strategies for drug delivery to the brain

Multiple strategies to circumvent the BBB for the delivery of potential therapeutic agents have been developed, including catheter-based interventions, pharmacological manipulation of drugs, and alternative nonvascular routes. These techniques have demonstrated potential, but each has major limitations: they are invasive procedures, have toxic side effects and low efficiency, or are not sufficiently safe.

Intracranial drug delivery is further complicated in the case of CNS tumors. Although the integrity of the BBB is often compromised in tumors, granting access to blood-borne agents which would not normally be able to enter the neural tissue, the disruptions are localized and non-homogeneous (40). In addition, the distribution of the microvasculature in solid tumors is itself heterogeneous, leading to greater diffusional requirements for drugs to reach neoplastic cells and spatially inconsistent drug delivery. Furthermore, high interstitial pressure within the tumor and edema surrounding the tumor often contribute to an increase in hydrostatic pressure in the normal brain parenchyma adjacent to the tumor, making these regions even less permeable to drugs than normal brain endothelium (34).

1.2.6.1 Catheter-based BBB disruption

Osmotic opening of the BBB is possible by injection of a hypertonic solution, such as mannitol or arabinose, into a catheter placed in the carotid artery. The introduction of the hyperosmolar solution causes a difference in osmotic pressure between the intravascular space and the endothelial wall of the blood vessel. To balance

the osmotic pressure, water rushes out of the endothelial cells, causing their shrinkage and expansion of the intercellular spaces. In this way, the paracellular pathway through the BBB, normally occluded by tight junctions, is transiently opened, allowing small and large molecular agents to enter the brain interstitium over the period of a few hours (2, 41-43). Chemotherapy accompanied by osmotic BBB disruption has yielded moderate augmentation of the delivery of antitumor agents to the brain (44, 45). One major limitation of this method is that it affects the entire volume of tissue supplied by the injected artery, allowing diffuse cytotoxic drug penetration to non-targeted brain tissue. In addition, it has been associated with an increased risk of altered glucose uptake, microembolism, and abnormal neuronal function (3, 34, 46).

A method thought to be potentially safer than osmotic BBB disruption is biochemical BBB disruption by intracarotid infusion of agents such as leukotrienes, bradykinin, nitric oxide, or analogs (47-49). In contrast to osmotic disruption methods, these methods appeared to selectively affect brain tumor capillaries due to the down-regulation of the enzymatic barrier in tumor endothelial cells, while leaving normal brain capillaries unaffected (49, 50). Pre-clinical data in glioma-bearing rats showing enhanced tumor drug delivery and survival led to clinical trials (51, 52), but the trials have since been abandoned due to similar risks shown in osmotic BBB disruption (53).

Convection-enhanced delivery is another technique that utilizes a catheter-based approach (11, 54-56). It is based on maintaining a pressure gradient by delivering a continuous interstitial infusion of a drug via intracranial catheters. The resultant bulk fluid convection forces the aqueous solution through the brain interstitium to distribute the drug over large volumes of target tissue (57). An alternative approach to increasing the

pressure gradient is to increase the diffusion gradient by maximizing the concentration of the the infused agent; such an approach has been shown to increase the volume of distribution (58, 59). Clinical trials of convection-enhanced delivery of intratumoral chemotherapeutic agents have shown some significant antitumor response rates with varying degrees of clinical impact (60-63). However, the technique is not without its limitations. Preferential flow of the forced fluid along white matter tracts can result in unintentional distribution patterns of the drug, resulting in harmful consequences such as diffuse astrogliosis (64, 65). Also, as with other transcranial catheter-based approaches, it is an invasive intracranial procedure with significant risk of morbidity and mortality.

1.2.6.2 Pharmacological modification

Without altering the BBB permeability, pharmacological modification is another approach which is being explored to increase the ability of agents to penetrate the BBB. Since lipophilic drugs cross the BBB much more easily than their hydrophilic counterparts, lipidization of small-molecule drugs can facilitate their passage through the phospholipid bilayer of the endothelial cell membrane. By conjugation to a lipid carrier or by reduction of the strength of its hydrogen bonding, lipidization increases the transcellular transport of a molecule into the brain interstitium (66, 67). In another process of pharmacological modification called cationization, proteins can be attached to a charged molecule, which induces transcellular uptake as a result of interactions with anionic groups on the cell membrane (68). However, while uptake in the brain is increased by these processes, uptake is also increased in peripheral tissues, reducing the plasma concentration and availability of the circulating agent and increasing the toxicity to non-targeted tissues. In addition, efflux processes can also be enhanced by these

processes, resulting in poor retention. Thus, poor selectivity and poor retention are major limiting factors in the applicability of these approaches (34).

Other carrier-mediated or receptor-mediated approaches take advantage of the endogenous transport mechanisms of the BBB by conjugating small- or large- molecule drugs to a known BBB transport vector (69-71). These transport vectors have been termed “molecular Trojan horses” because molecules which would not normally cross the BBB are essentially disguised by the attached carrier molecule to gain entry to the brain in pharmacologically significant amounts (72-74). For example, large molecules, such as recombinant proteins, neuropeptides, and therapeutic genes, can be bound to an endogenous peptide or monoclonal antibody which undergoes receptor-mediated transcytosis, to form a chimeric peptide, enabling the attached agent to benefit from the native BBB transport process (28). While this approach may be effective in small doses, the technique is limited by the number of available receptors expressed on the brain endothelium and by the finite carrying capacity of a given carrier (53). Furthermore, in spite of the target selectivity and therapeutic potential of the technique demonstrated in animal models (74), molecularly targeted therapies are often beleaguered by systemic toxicity (75).

Biodegradable polymer-based nanoparticles, liposomes, and micelles are also being developed for drug and gene delivery (76-78). The viability of these carrier-based approaches is increased by the modification of their surfaces with poly(ethylene glycol), a process known as pegylation, which increases their stability and increases their circulation time in the body (79, 80). Nanoparticles have been shown to improve both penetration and retention of a bound drug in the brain (81-83) and to improve therapeutic

efficacy in glioma-bearing rats (76, 84). While these approaches show great promise, they too are limited by their finite carrying capacity and considerable burden for chemical conjugation.

Yet another strategy is to inhibit the drug efflux transporters expressed in the BBB. The use of pharmacological modulators known as poloxamers blocks the activity of efflux pumps such as Pgp, allowing increased transport of their substrates (85-87). These modulators have been shown to effectively enhance the transport of intravenously administered drugs to the brain in animal models (88, 89). However, a major limitation of disabling the powerful, multispecific efflux barriers is that it allows the passage of all substrates normally blocked by the transporter pumps, resulting in loss of protection everywhere in the brain and dramatic neurotoxicity (37).

1.2.6.3 Other nonvascular routes to CNS drug delivery

Direct administration of an agent into the CSF is one way to bypass the BBB altogether by using delivery routes which do not involve the vascular system. Drugs can be infused into CSF through the brain ventricles (intraventricular route) or by lumbar puncture (intrathecal route). Since the drug would be contained within the CSF by the blood-CSF barrier, and since there is free molecular exchange between the CSF and brain interstitial fluid, high CSF drug concentrations should theoretically translate into therapeutic CNS drug concentrations with minimal systemic toxicity (34). In practice, however, the rate of drug distribution within the CSF is very slow. Drug diffusion through the brain parenchyma is also very slow and inversely proportional to the molecular weight of the drug (90, 91). Furthermore, this approach is complicated by

increased intracranial pressure and high clinical incidence of hemorrhage, neurotoxicity, and CNS infections (34).

Localized drug delivery in the brain is possible with methods such as direct intratumoral injection (92, 93) and controlled release from polymer implants (12, 94, 95). Such approaches can deliver therapeutic molecules at a defined rate over a specific period of time. Implantable devices can be positioned by stereotaxy in precisely defined targeted areas and the procedure can be repeated if necessary (96). This technique has been shown to prolong survival in patients with recurrent aggressive glioma and has proven its clinical impact (95). However, the limited diffusion of drugs into the brain from the implanted source and their rapid elimination by active efflux transport present weaknesses to this approach to CNS drug delivery (94). In addition, due to the invasive intracranial surgery required, this approach can only be used in a limited number of patients and carries significant risk of morbidity and mortality with only modest benefit (97).

1.3 Focused Ultrasound (FUS)

A novel approach to deliver drugs to the brain uses focused ultrasound to temporarily disrupt the BBB in a noninvasive and localized manner. In this technique, acoustic energy is concentrated in a focal spot to induce localized biological effects deep below the tissue surface with minimal effects to surrounding nontargeted tissue, even in the path of the ultrasound beam (98-101). Advances in acoustic technology have enabled the use of ultrasound in the brain, in spite of strong energy attenuation by the skull bone (102, 103). Because acoustic energy can be applied in a completely noninvasive manner, has the ability to precisely target tissue of interest while leaving other structures unaltered, and enables the passage of pre-existing drugs through the BBB, focused ultrasound offers distinct advantages over other diffuse or invasive methods of drug delivery to the CNS.

1.3.1 Background

Ultrasound is generated by applying an electrical voltage to a piezoelectric material, such as certain crystals or ceramics, which responds with mechanical deformation in proportion to the applied voltage. The expansion or contraction of the material causes the compression or rarefaction of its surrounding medium, such as air or water. An oscillating voltage then produces pressure waves; at frequencies in excess of ~18 kHz, the upper limit of human hearing, the resultant pressure wave is termed ultrasound. The effect works both ways, so mechanical stress will conversely induce a voltage across the material. Thus piezoelectric transducers can be used both to generate and receive ultrasonic signals.

Ultrasound propagates as a mechanical wave through tissue with attenuation of its pressure amplitude $P(z)$ described by:

$$P(z) = P_0 e^{-\mu z} \quad (1)$$

where μ is the frequency-dependent attenuation coefficient per unit path length z due to energy scattering and absorption in tissue, and P_0 is the incident peak rarefactional pressure amplitude at the surface. Ultrasound has a relatively low absorption rate in soft tissue; at 1.0 MHz, ultrasound has an approximate wavelength of 1.5 mm and its focal penetration depth can reach up to 10 cm (104). As with any wave, reflection, refraction, and diffraction at media interfaces of vastly different acoustic impedance, due to differences in density and sound speed, severely reduce energy transmission. Much of the mechanical energy lost from the propagating wave is converted to heat and absorbed in the body. Thus, the use of ultrasound has been limited in areas of the body which include interfaces between soft tissue and gas or bone, such as in the lungs, digestive tract, and brain, where energy losses can cause unwanted heating and severe tissue damage (105).

The ability of ultrasound to be focused has made it practical for therapeutic use. The size of the focal region is limited by the wavelength and its sharpness is determined by the ultrasound frequency and the geometry of the source transducer (105). Thus, higher frequencies with smaller wavelengths can achieve tighter foci, while lower frequencies with greater wavelengths produce wider focal regions. Therapeutic applications of focused ultrasound can be achieved with both thermal and mechanical effects. In tissue ablation, the induced temperature is raised high enough over a short period of time (~seconds) to cause cell death by protein denaturization and coagulative necrosis, while in hyperthermia, an induced temperature change of only a few degrees for

an extended period of time (~minutes) can sensitize tissue to radiation and chemotherapy. In addition to thermal effects, focused ultrasound can induce mechanical effects in biological tissue. In cavitation, the interaction of a gas bubble with the acoustic field, whether by radial oscillation (stable cavitation) or violent collapse (inertial cavitation) (106), can significantly enhance absorption and heating effects in tissue (107). Gas bubbles can form spontaneously in tissue during exposure to high intensity focused ultrasound, or pre-formed gas bubbles, such as those found in ultrasonographic contrast agents, can be introduced into the acoustic field by intravenous injection. The variety of bioeffects induced by focused ultrasound at therapeutic frequencies ranging from 0.5 to 10 MHz has prompted its investigation for diverse medical applications, including tumor and tissue ablation (108-121), hemostasis (122-125), vessel occlusion (126-128), thrombolysis (129-134), and BBB disruption for drug and gene delivery (16, 17, 21, 135-140), in multiple organ systems.

1.3.2 History of therapeutic ultrasound in the brain

The use of ultrasound for therapeutic applications in the brain has been studied for over half a century. In the early part of the 20th Century, it was demonstrated that high frequency sound waves could induce biological effects in tissue (141). In the 1940's, other investigators attempted to use focused ultrasound to induce permanent changes in animal brains for therapeutic applications but could not do so without undesired damage due to the attenuation and distortion caused by the skull bone in the path of the ultrasound (142, 143). Removal of a section of the skull bone by craniotomy in subsequent studies enabled the use of focused ultrasound to produce discrete lesions deep within the brains of animals and humans (144-149). In the 1960's, animal experiments with micro-

thermocouples implanted in the brain revealed that tissue damage was caused by temperature elevation at the acoustic focus resulting from the use of high intensity focused ultrasound (150-154). Other studies demonstrated the capacity of ultrasound to induce changes in the permeability of the BBB (155-157). In addition, ultrasound-induced hyperthermia in the brain has been studied extensively to sensitize tissue and enhance the therapeutic impact of radiation or chemotherapy (158-162). Thus, ultrasound has been used to produce both structural and functional changes within the brain.

1.3.2.1 Development of ultrasound applications through the skull

Since the skull was viewed as a barrier to therapeutic applications in the brain, early clinical studies for the treatment of patients with Parkinson's disease and malignant brain tumors were performed by applying focused ultrasound to the brain through a cranial window (163-166). By the late-1970's, the concept of focusing the acoustic energy through the skull had emerged. Studies demonstrated that ultrasound at frequencies less than 1 MHz could be focused through the skull with some distortion and shifting of the foci (167-169). Phased transducer arrays were later suggested as a method to compensate for the distortion caused by the skull. By adjusting the driving phase of each transducer element in the array, the acoustic focus distorted by the skull could be restored (170). This strategy, along with distributing the acoustic energy over a larger surface area of the skull and active cooling of the scalp, can also address problems of unwanted heating in and around the skull due to energy absorption in the bone (171, 172). The requisite phase and amplitude corrections factors for each individual transducer elements can be derived from x-ray computed tomography (CT) scans (102, 173). A hemispherical MRI-guided phased array system has been designed for thermal ablation of

malignant brain tumors (174, 175), which has led to a phase I clinical trial (101). Since the acoustic intensity used for BBB disruption is at least two orders of magnitude less than for thermal ablation, it follows that such a system could also be used for noninvasive BBB disruption through the human skull. Alternative methods of transcranial ultrasound propagation, using lower frequencies (250-300 kHz) (176) or shear-mode transmission (177, 178), which distort to a lesser extent in the bone, are being investigated to eliminate the need for patient-specific CT corrections. Thus, several methods exist to compensate for distortions in beam propagation induced by the skull bone to allow the ultrasound to be applied completely noninvasively in the brain.

1.3.2.2 Development of targeting and monitoring methods

The development of methods to visualize diseased tissue and to monitor the effects of focused ultrasound has been critical to its application in the brain. Crude targeting in early clinical applications used a stereotactic frame based on x-ray images of bony landmarks (164). A more advanced targeting system using CT guidance was later proposed but not clinically tested (179). However, these methods did not offer the ability to monitor the effects of ultrasound in the brain. More recently, MRI has been demonstrated to provide both an effective means of both targeting and monitoring of ultrasound in the brain (13, 21, 180-185). Its excellent soft-tissue contrast and high temporal resolution confer the ability to distinguish diseased tissue from normal tissue in many cases with unprecedented precision. Temperature-sensitive image sequences can provide information on relative temperature changes with an accuracy of ± 0.5 deg C (186-188). Furthermore, MR contrast enhancement during MRI-guided ultrasound-mediated delivery of molecules across the BBB has been demonstrated to correlate with

the amount of drug or antibody accumulated in the brain, indicating its potential to provide important feedback during ultrasound-mediated CNS drug delivery (16, 17). Finally, the combination of functional MRI and focused ultrasound may enable precise focal stimulation of brain activity in targeted regions. The ability to steer the ultrasound beam to a desired target and to closely monitor its effects with MRI has enabled this technology to move beyond experimental status into clinical adoption. MRI-guided focused ultrasound earned approval by the U.S. Food and Drug Administration for the thermal ablation of benign leiomyomata, more commonly known as uterine fibroids, in 2004 (189).

1.3.3 Ultrasound-induced BBB disruption

1.3.3.1 BBB disruption using ultrasound alone

It has long been known that ultrasound is capable of disrupting the BBB (155-157). In the 1950's, deposition of trypan blue and radioactive phosphate tracers in the brain after exposure to focused ultrasound was used to demonstrate increased permeability of brain capillaries without visible structural changes (155). BBB disruption was later observed in the periphery of thermal lesions resulting from ultrasound-induced tissue coagulation (135, 190). However, under further investigation, thermally induced BBB disruption has always been associated with tissue damage (190). Disruption of the BBB was also observed after high-intensity ultrasound exposures above the cavitation threshold, sometimes without tissue damage, indicating that the effect may be related to an interaction between the acoustic field and gas bubbles. However, the unintentional BBB disruption was sporadic and unpredictable, and its association with tissue damage was unclear (191, 192). In 1990, it was proposed that the phenomenon of ultrasound-

induced BBB disruption could be used with antineoplastic agents and ultrasound-induced thermal ablation to enhance the treatment of brain tumors (135). However, molecular delivery into the brain by ultrasound-mediated BBB disruption would not be practical without a controlled reversible process which does not induce tissue damage.

1.3.3.2 Microbubble-enhanced ultrasound for BBB disruption

A method to induce focal BBB disruption in a predictable and reproducible manner without obvious permanent damage to the brain tissue was demonstrated in rabbits when pulses of focused ultrasound were applied through a cranial window in the presence of an ultrasonographic contrast agent containing gas-filled microbubbles (13). Unlike in thermal ablation applications which use high-intensity focused ultrasound (193), the intravenous administration of gas-filled microbubbles allows the desired BBB opening to be achieved with powers approximately two orders of magnitude lower than those required in the absence of microbubbles and largely confines the induced bioeffects within the walls of the blood vessel.

Successful focal BBB disruption has been demonstrated using ultrasound frequencies ranging from 260 kHz to 2.04 MHz (13, 194-196), allowing the passage of MRI contrast agents Magnevist[®] (gadopentatate dimeglumine, molecular weight: 938 Da) (194) and MION (monocrystalline iron oxide nanoparticles, molecular weight: 10,000 Da) (197), trypan blue (molecular weight: 961 Da), horseradish peroxidase (molecular weight: 40,000 Da) (195), and antibodies (molecular weight: 150,000 Da) (16, 21, 140) into the brain. The size of the focal region demonstrated by contrast-enhanced MRI decreased with increasing frequency, with focal diameters smaller than 1 mm possible at the higher frequencies (196). The transient nature of the induced BBB disruption was

confirmed by contrast-enhanced MRI, which showed that the BBB was mostly restored 5-6 h after exposure to ultrasound (sonication) and fully intact 2-5 days and 4 weeks after sonication (195, 198). Focal BBB disruption was sometimes accompanied by minor extravasation of erythrocytes from affected capillaries in the sonicated region, but no regions of ischemia or apoptosis which would indicate a compromised blood supply were detected, nor were delayed effects observed by MRI or histology up to 4 weeks after sonication (198); the incidence of erythrocyte extravasation per unit area decreased with lower frequencies (196). Thus, MRI-guided focused ultrasound can induce transient, localized BBB disruption in a noninvasive manner to enable the passage of diagnostic or therapeutic molecules into the brain and is a relatively safe alternative to invasive or diffuse methods currently available. Furthermore, it can be achieved using ultrasound frequencies suitable for transcranial delivery (195).

The influence of various sonication parameters on the induced BBB disruption has been extensively explored since the introduction of the method. Most work cited has used ultrasound exposures at low pressure amplitudes (<1 MPa) with 10-ms pulses repeated at a frequency of 1 Hz for a duration of 20–30 s. One study showed that BBB disruption was not affected by variation in the pulse repetition frequency but was influenced by burst length (199) and peak negative pressure amplitude (16, 17, 21, 195). The pressure threshold for BBB disruption has been shown to be dependent on both frequency and burst length, increasing with the former (200) and decreasing with the latter (199). However, when expressed in terms of mechanical index, defined as pressure amplitude in MPa divided by the square root of frequency in MHz, the mechanical index threshold appeared to be constant at 0.46 (95% confidence intervals: 0.42 to 0.50) when

other sonication parameters are kept constant (196). Investigations of the impact of the concentration of microbubbles on BBB disruption have been inconclusive (17, 199, 201).

1.3.3.3 Physical mechanisms

Ultrasound-induced BBB disruption appears to be mechanically, rather than thermally, mediated; one study in rabbits using 1.63-MHz sonications concluded that the temperature elevation induced during BBB disruption was approximately 0.025 deg C (13). Although it is believed that ultrasound-induced BBB disruption is achieved by using the microbubbles as cavitation sites (98, 99), the exact physical mechanism by which the ultrasound-microbubble interaction induces disruption of the BBB is not fully understood. Multiple biological effects may arise from the interaction of microbubbles with a propagating acoustic wave in tissue (202). In stable cavitation, a bubble expands and contracts at the frequency of the oscillating pressure field. It may grow in size by rectified diffusion, when more gas diffuses into the bubble from the surrounding medium during expansion than diffuses out of the bubble during the compression phase of the pressure wave (203). In inertial cavitation, which occurs at high acoustic pressures, the inertia of the surrounding medium can cause the violent collapse of the bubble during the positive pressure cycle, producing shock waves and high-velocity jets (107), free radicals (204), and high local temperatures (205-207). Another process known as acoustic streaming occurs when the oscillation of bubbles causes their surrounding medium to flow and is often associated with large shear stresses (208). In addition, the acoustic field exerts a steady radiation force on the bubbles along the direction of the ultrasound beam, pushing the bubbles against the blood vessel wall (209).

Of the above-described bioeffects, inertial cavitation would likely have the most

significant effect due to the large energy concentrations in the region of the collapsing bubbles. However, ultrasound-induced BBB disruption has been demonstrated over a range of acoustic intensities at 260 kHz without wideband acoustic emission (200), a known signature of inertial cavitation *in vivo* (150), indicating that inertial cavitation is not necessary for the blood-brain barrier disruption. Bubble collapse detected by wideband acoustic emission was associated with small regions of erythrocyte extravasation, while bubble oscillations were detected when BBB disruption was induced without vascular damage (200).

1.3.3.4 Biological mechanisms

Immunoelectron microscopy studies have provided some insight into the biological mechanisms by which microbubble-enhanced focused ultrasound enables the trans-BBB transport of macromolecules. One study showed that passage through the BBB after treatment with microbubble-enhanced ultrasound occurs via both paracellular and transcellular routes, including open endothelial cell tight junctions, enhanced active vesicular transport, endothelial cell fenestration and channel formation, and free passage through injured endothelium (14). Specifically, the redistribution and loss of immunosignals for TJ-specific proteins occludin, claudin-5, and ZO-1 provide direct evidence of the disassembling of the TJ molecular structure and associated functional loss of the BBB immediately following ultrasound exposure; six hours after sonication, the protein immunosignals and BBB function are both restored (15). Active vesicular transport following ultrasound-stimulated BBB disruption was preferentially demonstrated in brain arterioles, rather than venules or capillaries (210). Furthermore, an *in vivo* study in mice using multiphoton microscopy through a cranial window revealed

arteriolar vasoconstriction during the ultrasound pulses, followed shortly by leakage of a tracer, suggesting that the increase in BBB permeability might be related to temporary vessel spasm (19).

1.4 Doxorubicin (DOX)

1.4.1 Clinical use

Doxorubicin (molecular weight: 580 Da) is one of the most commonly used cytotoxic drugs in both single-agent and multi-agent chemotherapy regimens. It is used to treat many solid forms of cancer, including breast (211), ovarian (212), bone (213), lung (214), thyroid (215), and gastrointestinal carcinomas (216), as well as blood-derived cancers, such as lymphoma and multiple myeloma (217-219) and soft-tissue sarcomas (220). Because it has demonstrated antineoplastic efficacy against such a variety of cancer types, it has enjoyed widespread clinical use for over 30 years (221). Figure 1-1 shows that intratumoral DOX concentration is strongly correlated ($R^2 = 0.90$) with patient response rate, irrespective of the type of cancer (222).

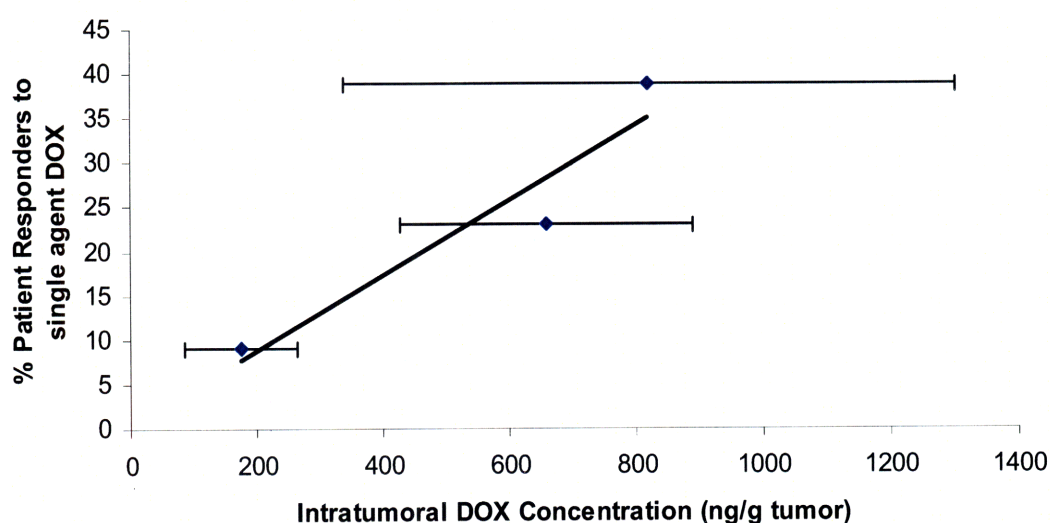


Figure 1-1: Correlation of intratumoral DOX concentration and patient response rate. DOX concentration measured in excised tumors is linearly proportional to the response rate of patients with breast, gastric, or colorectal carcinoma ($R^2 = 0.90$). Data taken from (222).

Despite its extensive clinical use, DOX is not typically used to treat intracranial tumors because, as a substrate for the powerful efflux pump Pgp, it cannot cross the intact BBB (84). Systemic administration of DOX has seldom been effective in patients with brain tumors due to poor accumulation in glioma tissue (5). However, it has been shown to arrest cell growth and induce apoptosis in malignant glioma cell lines (223). Moreover, direct intratumoral infusion of DOX has been shown to improve survival of glioma patients (92). Thus, the antineoplastic efficacy of DOX against glioma is not in doubt. The evidence indicates that if the accumulation of DOX could be increased to therapeutic levels within the brain, it could be effective in the treatment of malignant brain tumors, whether primary glioma or metastatic brain tumors which originated elsewhere in the body.

1.4.2 Mechanism of action

Formerly known as adriamycin, doxorubicin belongs to the family of anthracycline antibiotics. Like many chemotherapeutic drugs, it combats the uncontrolled proliferation of cancerous cells by binding to DNA to inhibit nucleic acid synthesis and block cell reproduction (224). Cell structure studies have demonstrated that DOX rapidly penetrates cells and binds to perinuclear chromatin (225). It is thought to inhibit the action of topoisomerase II, which is responsible for the unwinding of DNA during the transcription process. The interference of DOX during the process of DNA transcription and gene replication induces chromosomal aberrations and interrupts the continuous cycle of cell proliferation, leading to cell death (226). The bioreactivity of DOX with iron, oxygen, or free electrons in the body can also produce free radicals, such as the

highly reactive hydroxyl radical ($\text{OH}\cdot$), which themselves induce DNA damage (227, 228).

These multiple mechanisms of DNA damage make DOX a highly effective cytotoxic agent. Cancerous cells are strongly impacted by the interference of DOX during the cell reproductive cycle due to their high turnover rate. However, as with any chemotherapeutic drug, DOX also causes unwanted cell death in normal cells as well, especially in those which proliferate quickly, such as hematopoietic cells, gastrointestinal cells and hair follicles. In addition, DOX can cause cardiomyopathy and loss of cardiac function (229, 230), which is associated with the production of free radicals (231). The encapsulation of DOX within microscopic (~ 100 nm) phospholipids vesicles, known as liposomes, has been shown to reduce the cardiotoxic effects associated with DOX while prolonging circulation time (232, 233). Due to these benefits, this liposomal form of DOX is most commonly used clinically.

1.4.3 Spectroscopy

Doxorubicin absorbs and emits light according to the spectra shown in Figure 1-2, with peak absorption at 480 nm and peak emission near 595 nm (234). Because the amount of light emitted is directly proportional to the number of molecules, the fluorescent properties of doxorubicin allow us to make quantitative measurements.

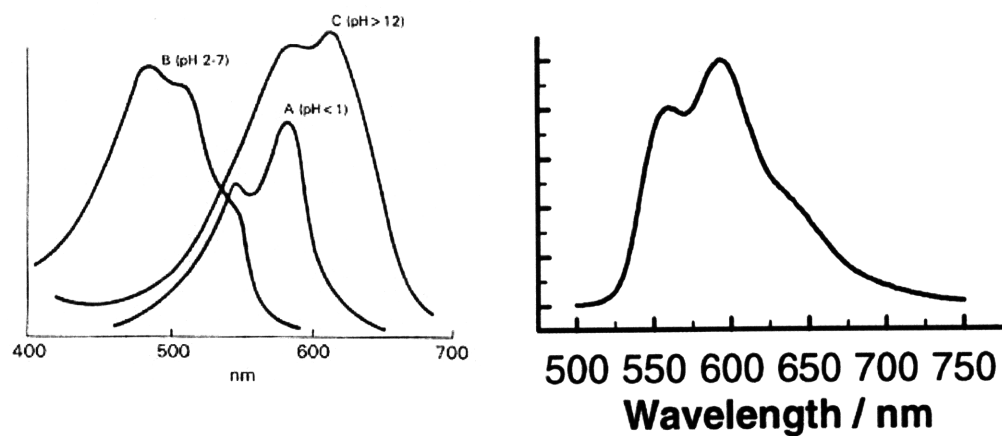


Figure 1-2: Fluorescence spectra for doxorubicin in aqueous solution. A, Absorption spectrum show maximum absorption at 480 nm (curve B, pH 2-7) (235). B, Emission spectrum with excitation at 479 nm shows maximum emission near 595 nm (234).

1.5 Scope of this thesis

The overall goal of this thesis was to further develop MRI-guided focused ultrasound for noninvasive trans-BBB drug delivery applications. In particular, we wish to develop a method to enable the efficacious use of doxorubicin for the treatment of intracranial malignant tumors.

In the first set of experiments, ultrasonic parameters were investigated to achieve consistent, localized disruption of the BBB in rats with an intact cranium. The threshold pressure amplitude for reliable BBB opening was determined. We also examined the relationship between the acoustic parameters and monitoring data acquired by MRI. In addition, the study confirmed our ability to focus the acoustic energy through the rat skull despite its attenuating effects, eliminating the need for invasive craniotomy in future experiments. The findings of this study helped to establish the framework for subsequent drug delivery experiments.

Based on the parameters determined for BBB disruption, we developed a protocol for the targeted delivery of liposomal doxorubicin to the brain in normal, healthy rats. The drug delivery protocol was adapted to increase the local penetration of doxorubicin through the BBB until its accumulation in the brain was within the human therapeutic range. Variations in both ultrasound delivery strategies and ultrasonic contrast agent dose were explored. In addition, the usefulness of MRI as a monitoring and feedback tool for the drug delivery procedure was explored by comparing the imaging data to the quantified accumulation of doxorubicin in the brain. These results provide evidence that our ultrasound-enhanced drug delivery technique has the potential to enable the practical use of doxorubicin in the brain, despite its inability to penetrate the intact BBB.

In the final component of this thesis, the therapeutic efficacy of our technique was put to the test. We compared ultrasound-enhanced trans-BBB drug delivery to standard intravenous chemotherapy by measuring the impact of ultrasound-enhanced delivery of doxorubicin on survival and on tumor growth rate in a rodent model of aggressive glioma.

In sum, this thesis demonstrates that MRI-guided focused ultrasound can be used to achieve consistent and reproducible BBB disruption without invasive craniotomy, to enable doxorubicin to accumulate in normal brain at levels sufficient to have a therapeutic effect, and to increase the antitumoral efficacy of doxorubicin in a rodent model of aggressive glioma. These pre-clinical data are important to establish the usefulness of this technique as justification to pursue the development of MRI-guided focused ultrasound for trans-BBB drug delivery applications toward clinical trials.

2 Materials and Methods

2.1 Animals and Equipment

2.1.1 *Animals*

Male Sprague-Dawley rats (200-400 g) were acquired from Charles River Laboratories (Boston, Massachusetts). In preparation for surgery or sonication, rats were anesthetized by i.p. administration of ketamine (90 mg/kg) and xylazine (10 mg/kg), per hour or as needed. The hair covering the dorsal surface of the skull was removed with depilatory lotion. For experiments requiring i.v. administration of contrast agents or chemotherapy, a 24-gauge catheter was inserted into the tail vein. For imaging on days before or after sonication, rats were anesthetized by induction in a vaporized isoflurane chamber (3% induction, 1–2% maintenance).

All animals were cared for in accordance with our institutional animal care policy. For animals in experiments of acute BBB disruption or ultrasound-assisted drug delivery, animals were sacrificed while under deep anesthesia 3.5–4 h after sonication by transcardial perfusion with 0.9% NaCl solution and 10% formalin in 0.1 M phosphate buffer, followed by harvest of the brain. For animals which were implanted with glioma for the survival study, euthanasia of those exhibiting severely impaired activity or weight loss in excess of 20% was conducted by i.p. injection of sodium pentobarbital (Euthasol, 180 mg/kg; Virbac Corporation, Fort Worth, Texas) or by transcardial perfusion with 0.9% NaCl solution and 10% formalin in 0.1 M phosphate buffer, while under deep anesthesia.

2.1.2 Ultrasound

2.1.2.1 Transducer

For all experiments, ultrasonic fields were generated by a single-element, spherically curved, air-backed piezoelectric transducer (manufactured in-house) with a diameter of 100 mm, radius of curvature of 80 mm, and resonant frequency of 1.5 or 1.7 MHz. The electrical impedance of the transducer was matched to 50 Ohms by means of an inductor-capacitor circuit contained within an external matching box.

2.1.2.2 Transducer characterization

Figure 2-1 shows the characteristic beam plots of the 1.7-MHz transducer, which produced a tight ellipsoid focal spot with diameter and length of 1 mm and 4 mm, respectively, at half-maximum pressure amplitude.

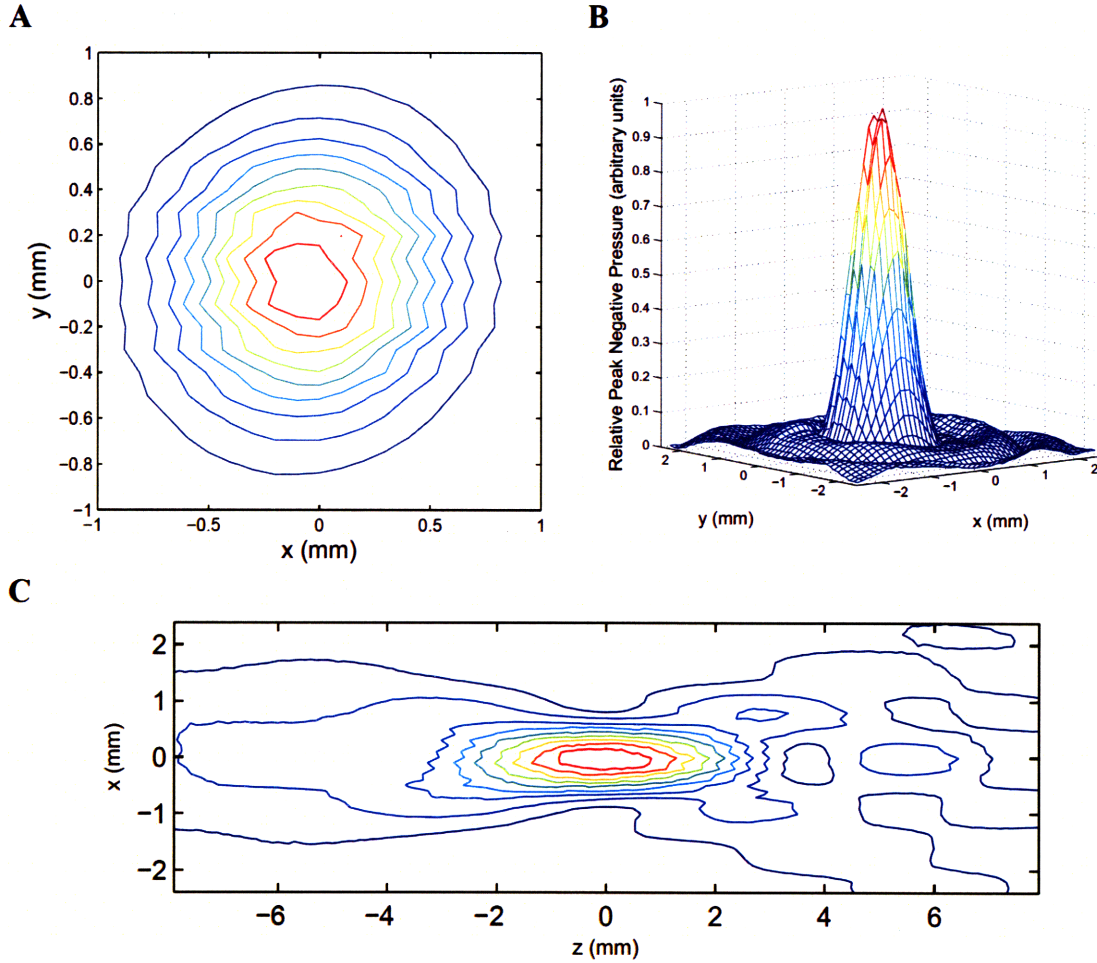


Figure 2-1: Characteristic beam plots for the 1.7-MHz transducer. A, Contour plot of relative peak negative pressure amplitude at the cross-sectional acoustic focus in degassed, deionized water. Pressure amplitude was normalized to the maximum value; 10 contour levels at increments of 0.1 are displayed. The focal diameter was approximately 1 mm at half-maximum pressure amplitude. B, Three-dimensional plot of relative peak negative pressure amplitude of the cross-sectional beam plot shown in A. C, Contour plot of relative peak negative pressure amplitude along the longitudinal axis of the acoustic focus. The focal length was approximately 4 mm at half-maximum pressure amplitude.

2.1.2.3 Transducer calibration

The transducer efficiency was measured using an acoustic radiation force balance system (236). The system is based on the principle that an acoustic wave exerts a force F on an ideal absorbing target proportional to the acoustic power P , as described by:

$$F = \frac{P \cos \theta}{c} \quad (2)$$

where c is the speed of sound in the given medium and θ is the angle of incidence (105).

The transducer was immersed in degassed, deionized water ($pO_2 < 1$ ppm) and driven at peak-to-peak voltages ranging from 0.050 – 0.250 V in 50-mV steps. A densely bristled brush was used as the absorbing target to encompass the complete acoustic beam emitted by the transducer. The brush was suspended in the water by a thin wires attached to an electronic weighing balance so that its face lay directly opposite the transducer. For each voltage, the acoustic power output of the transducer was calculated from the force exerted on the brush, which was measured by the change in weight of the absorbing brush. The output acoustic power averaged over three measurements was divided by the input electrical power to compute the efficiency of the transducer (Table 2-1).

Voltage (V)	Electrical Power (W)	Acoustic Power (W)	Efficiency (%)	Standard Error
0.050	1.93	1.04	53.9	6.57×10^{-3}
0.100	7.67	4.17	54.4	4.70×10^{-2}
0.150	17.2	9.30	54.1	3.73×10^{-2}
0.200	30.7	16.6	54.2	7.63×10^{-2}
0.250	48.0	26.4	55.0	1.09×10^{-1}

Table 2-1: Acoustic efficiency of air-backed single-element transducer. Frequency: 1.696 MHz; Radius of curvature: 80 mm; Diameter: 100 mm; F number: 0.8.

2.1.2.4 Derated measurements accounting for energy losses in bone and tissue

The absolute and relative peak negative pressure amplitudes were measured in a water tank with a calibrated 0.5-mm-diameter membrane hydrophone (Marconi, Chelmsford, United Kingdom) and a 0.075-mm-diameter needle hydrophone (Precision Acoustics, Dorchester, United Kingdom), respectively. However, due to the strong attenuation of ultrasound in the bone and, to a minor extent, in the brain tissue, the acoustic energy delivered to the brain *in vivo* is not the same as that measured in the

water tank. To better understand how a given set of acoustic parameters translates into *in vivo* effects, derated values accounting for energy losses through the skull and brain must be determined. Brain tissue is known to have a mean attenuation coefficient of 5 Np/m/MHz (237). Energy losses caused by the rat skull bone were measured by performing relative pressure measurements with the hydrophone in the water tank both with and without an *ex vivo* rat skull placed in the path of the ultrasound beam. The average pressure loss due to the skull over ten individual measurements was found to be 49%, with 51% of the incident energy transmitted through the skull. The pressure amplitude values reported in this study are derated to account for these losses.

Figure 2-2 shows the cross-sectional and longitudinal beam plots of the acoustic field produced by the placement of an *ex vivo* rat skull in the path of the ultrasound beam approximately 4 mm proximal to the focal center, as compared to those measured in water in the absence of the skull.

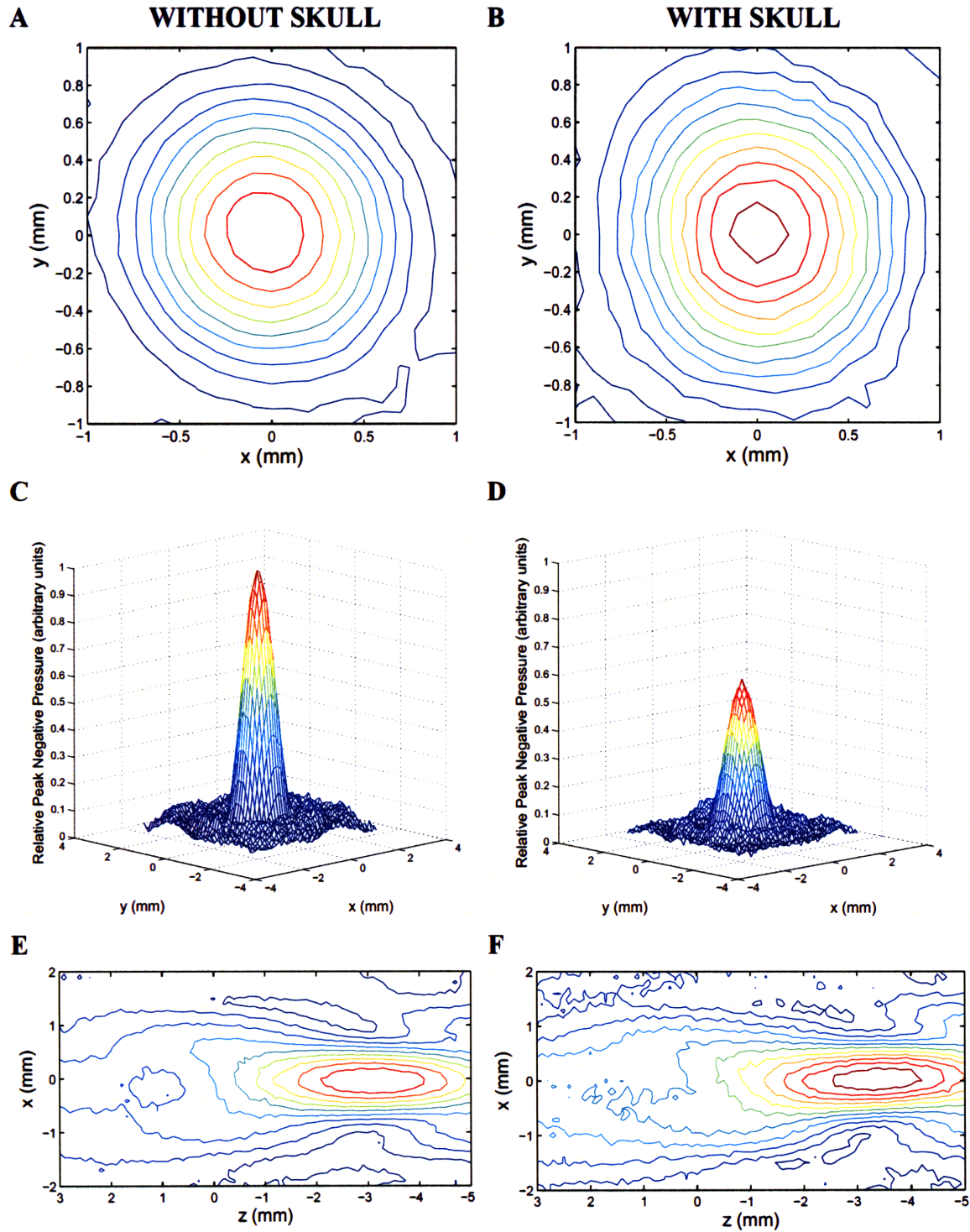


Figure 2-2: Comparison of beam plots with and without a rat skull in the beam path. A-B, Contour plot of relative peak negative pressure amplitude at the cross-sectional acoustic focus in the absence (A) and presence (B) an *ex vivo* rat skull; **C-D,** Three-dimensional plot of relative peak negative pressure amplitude of cross-sectional beam plot in the absence (C) and presence (D) an *ex vivo* rat skull; **E-F,** Contour plot of relative peak negative pressure amplitude along the longitudinal axis of the acoustic focus in the absence (E) and presence (F) an *ex vivo* rat skull. Pressure amplitudes were normalized to the maximum values measured without the skull; 10 contour levels at increments of 0.1 are displayed.

2.1.3 Experimental set-up

Figure 2-3 shows a diagram of the experimental set-up.¹ Inside the magnet room of a standard 3-Tesla clinical MRI scanner, the transducer was mounted on an MR-compatible² manual positioning system with three translational degrees of freedom and immersed in a tank of degassed, deionized water ($pO_2 < 1$ ppm). Outside the magnet room, a personal computer network with standard magnetic parts controlled the transducer by means of a function generator (model 395; Wavetek, San Diego, California), power amplifier (50-dB gain, model 240L; E&I, Rochester, New York), and power meter (model 438A; Hewlett-Packard, Palo Alto, California). Prior to each animal experiment, the coordinates of the acoustic focus of the transducer were determined using heat-sensitive MRI to visualize thermal changes induced in a gel phantom during high-power continuous-wave sonications.

The animal was placed into a custom-made holder with a bite bar so that its head was positioned above the transducer. The surface of the head was acoustically coupled to the transducer by the degassed water. Ultrasound was propagated through the water to the dorsal surface of the head and focused through the intact skull on a target centered 4 or 5 mm deep from the dorsal brain surface.

¹ Diagram adapted from original artwork by Dr. Nathan McDannold.

² The manual positioning system was made with aluminum and brass components so that it could be used in the presense of the high magnetic field without interfering with the MRI scanner.

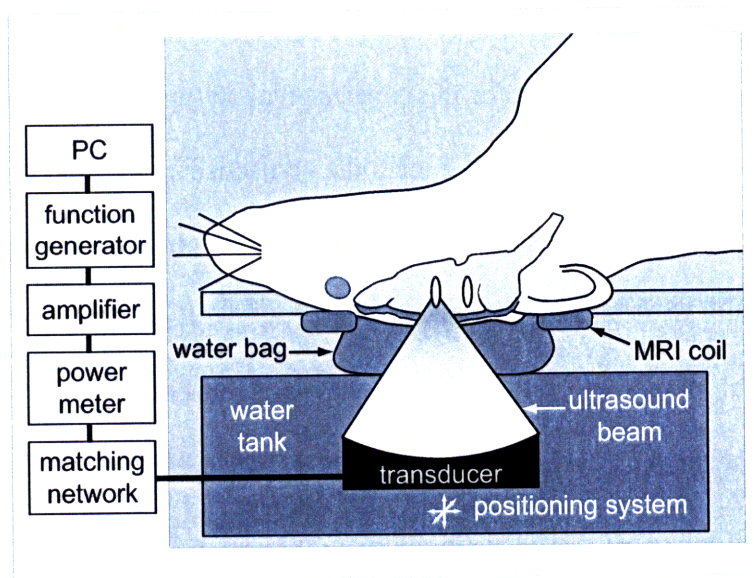


Figure 2-3: Diagram of the experimental set-up. Inside the MRI magnet room, the transducer was mounted on a manual MR-compatible 3-D positioning system and immersed in a water tank integrated into the MRI table. Outside the magnet room, a network consisting of a personal computer, function generator, power amplifier, power meter, and dual directional coupler served to control the transducer. The animal was placed into a custom-made holder with a bite bar so that its head was positioned above the transducer. The surface of the head was coupled to the transducer by degassed, deionized water.

2.1.4 Magnetic resonance imaging

The experimental set-up shown in Figure 2-3 was integrated into the table of a 3-Tesla clinical MRI scanner (General Electric Healthcare, Milwaukee, Wisconsin) for image guidance and evaluation. Each animal was placed on the table in the supine position with the dorsal surface of the head centered on a 7.5-cm-diameter transmit/receive surface coil (constructed in-house).

For all BBB disruption experiments, T1-weighted fast spin-echo (FSE) images (repetition/echo time (TR/TE): 500/17 ms; echo train length (ETL): 4; matrix size: 256 x 256; slice thickness: 1.5 mm; field of view (FOV): 8 cm; number of excitations (NEX): 2; flip angle (FA): 90 degrees) of the brain were acquired in three orthogonal planes. The target site for BBB disruption was identified on the MR images and the transducer

repositioned accordingly. Sonications were performed through the opening of the surface coil, which was filled with a plastic bag [poly(vinyl chloride), thickness $\sim 75\ \mu\text{m}$] containing degassed water. After ultrasound-mediated BBB disruption was completed, a bolus of gadopentatate dimeglumine MR contrast agent (Magnevist; Berlex Laboratories, Wayne, NJ; 0.125 mmol/kg; 0.25 mL/kg; molecular weight: 938 Da) was injected into the tail vein and additional images were acquired for up to 15 min.

2.1.5 Fluorometry

To quantify doxorubicin accumulation in brain tissue, a benchtop cuvette fluorometer (VersaFluor; Bio-Rad Laboratories, Hercules, California) with changeable filters was used. Because doxorubicin absorbs the most light between approximately 473 nm and 494 nm and emits maximal fluorescent light at about 590 nm (234, 238), fluorescence measurements were performed using filters with excitation and emission wavelengths of $480 \pm 10\ \text{nm}$ and $590 \pm 5\ \text{nm}$, respectively.

To calibrate the fluorometer for doxorubicin quantification, a serial dilution of DOX in acidified alcohol was used to measure the fluorescent signal of the extracted supernatant. For DOX concentrations of 100-1000 ng/mL, the gain of the VersaFluor fluorometer was set to medium. For lesser DOX concentrations of 10-100 ng/mL, the fluorometer was not sensitive enough to differentiate small differences in concentration using medium gain, so the gain was set to high. For each experiment, a freshly prepared solution of acidified alcohol was used as a "blank" to zero the fluorometer. Figure 2-4 shows the calibration curves used to convert the fluorometric readings to doxorubicin concentration.

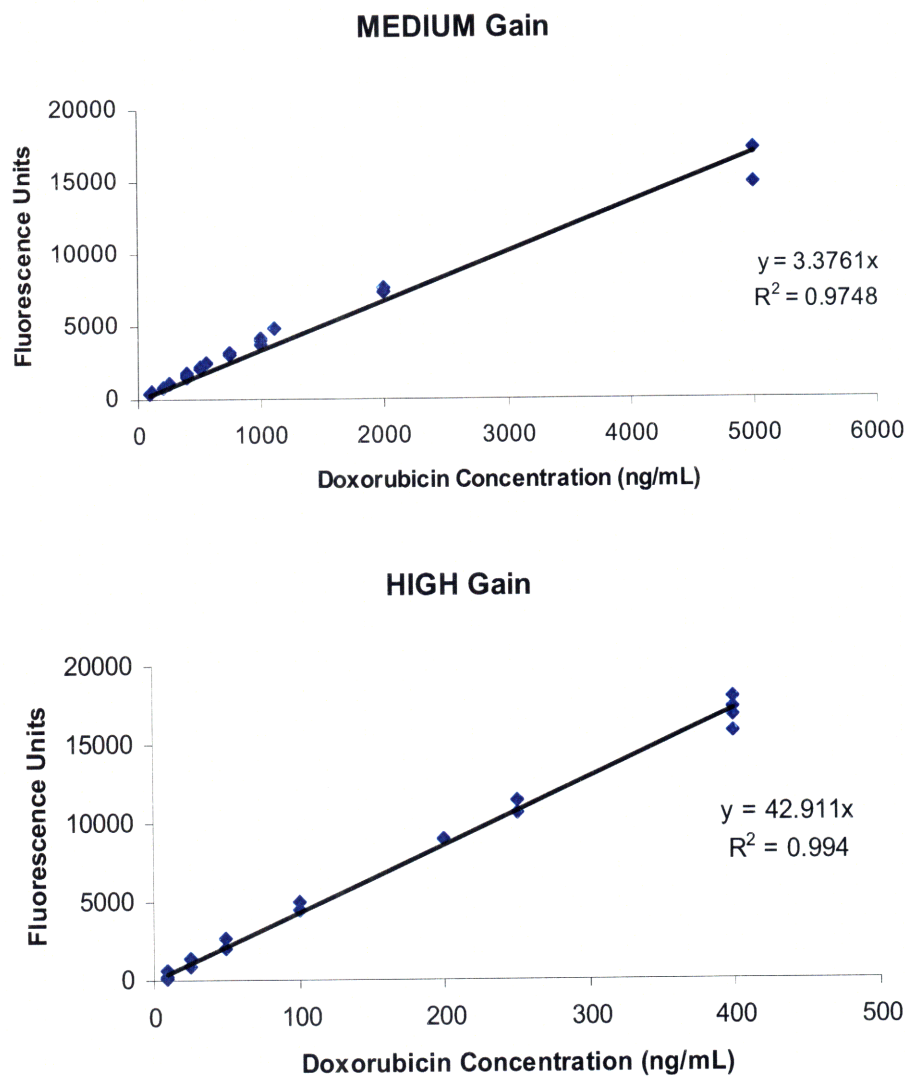


Figure 2-4: Calibration curves for fluorometric measurements of doxorubicin concentration, showing a strong linearly proportional relationship between arbitrary fluorometric units and doxorubicin concentration for A, medium gain ($R^2 = 0.97$) and B, high gain ($R^2 = 0.99$). The calibration coefficients were obtained by forcing each linear fit through zero.

2.2 Blood-brain barrier disruption using transcranial MRI-guided focused ultrasound

In the first step toward developing a protocol for targeted drug delivery across the BBB in a standard pre-clinical rodent model, we investigated the ultrasonic parameters needed to achieve reproducible, localized blood-brain barrier disruption in rats when focused ultrasound is applied through the intact rodent skull. Although ultrasound is strongly attenuated in bone, we hypothesized that the skull of the rat is thin enough to permit the focusing of the ultrasound beam sufficient to induce localized BBB opening.

2.2.1 Sonications

Energy was delivered in pulsed sonications with burst length of 10 ms and pulse repetition frequency of 1 Hz (i.e., 10 ms ON followed by 990 ms OFF; duty cycle: 1%) for 30 s. Each sonication was accompanied by a bolus of a microbubble-based ultrasound contrast agent (Optison; Mallinckrodt, St. Louis, MO) into the tail vein catheter. Each mL of Optison contains $5 - 8 \times 10^8$ microbubbles, which are composed of perfluorocarbon gas-filled albumin shells with a mean diameter of $2.0 - 4.5 \times 10^{-6}$ m. The administration of 0.1 mL/kg Optison was simultaneous with sonication and followed by 0.2 mL 0.9% NaCl solution (normal saline). Multiple sonications in an individual rat were spaced 4 to 5 min apart to allow time for vascular clearance of the Optison, which has a pulmonary elimination half-life of 1.3 ± 0.7 min (mean \pm standard deviation (SD)) in humans.

To find the pressure amplitude with which BBB disruption was reliably induced, sonications were performed in 50 rats in up to four target locations per brain, with acoustic power levels ranging from 0.06 to 3.0 W, corresponding to derated peak negative pressure amplitudes of 0.36 – 2.5 MPa in the brain. BBB disruption was

measured by MRI contrast enhancement as described below.

2.2.2 Image analysis

MRI contrast enhancement was evaluated at each target location using software written in-house using MATLAB (MathWorks, Natick, MA). The average signal intensity within a selected 3x3x1-voxel region of interest (ROI) was normalized to the pre-contrast baseline value of the ROI to calculate the signal enhancement. If the maximum enhancement of the sonicated ROI, averaged over three consecutive time points, exceeded that of a control ROI outside of the focal target by more than one standard deviation, the BBB was considered to have been opened in that location.

2.2.3 Trypan blue staining

Trypan blue (ICN Biomedical, Aurora, OH; 80 mg/kg) was administered i.v. to several rats prior to sonication for visual confirmation of BBB disruption in harvested tissue samples.

2.2.4 Histologic analysis

Histologic analysis was performed for eight locations in two rat brains exposed to ultrasound with acoustic power ranging from 0.12 to 1.2 W (0.5 – 1.6 MPa). The animals were deeply anesthetized and sacrificed 4 h after the last sonication. Their brains were perfused by transcardiac methods with 10% buffered formalin phosphate, embedded in paraffin, and cut into 5-micron sections in the axial plane perpendicular to the direction of ultrasound propagation. Every thirtieth section was stained with hemotoxylin and eosin (H&E). Sections exhibiting the greatest effect were identified and evaluated for capillary damage by light microscopy.

2.3 Targeted delivery of doxorubicin to normal brain by ultrasound-mediated blood-brain barrier disruption

Once the parameters for consistent BBB disruption by transcranial sonication were established, we adapted the technique to aid in the targeted delivery of the chemotherapeutic doxorubicin in the rat brain. Our aim was to develop a protocol for ultrasound-mediated BBB disruption which would allow DOX to accumulate at sufficient levels in the normal *in vivo* rat brain to have a therapeutic effect.

2.3.1 Chemotherapy

Doxorubicin hydrochloride (DOX) encapsulated in long-circulating pegylated liposomes (Doxil; Ben Venue Laboratories, Bedford, OH; 5.67 mg/kg) was selected for targeted delivery through the blood-brain barrier. In this form, greater than 90% of the drug is encapsulated within the liposomes. Once the liposomes pass from the vascular compartment to the parenchyma, the liposome is degraded by endogenous enzymatic processes and the encapsulated DOX is released in the tissue.

2.3.2 Ultrasound

The experimental set-up of the first study was used (Figure 2-3). Based on the results of the previous experiments, 1.2 MPa was used to provide BBB disruption to deliver doxorubicin to the brain. In the first set of experiments, we sought to identify an ultrasound protocol which would deliver a therapeutic level of DOX through the BBB. The acoustic parameters and delivery schedule were varied in 20 rats. The tissue drug concentration was considered within human therapeutic levels when the dose reached levels shown to correspond with a 39% patient response rate (clinical dose-response curve) (Cummings 1986). For each rat, four overlapping pulsed sonications (Table 2-2;

Set #1, Sonication A) were performed on the brain and spatially distributed in the corners of a 1.5-mm square to increase the area of BBB disruption. DOX was administered i.v. in four bolus injections immediately after the Optison injections, for a total DOX dose of 3.0 – 5.7 mg/kg. To dramatically increase the amount of DOX delivered to the brain, some rats also received an additional 40-min pulsed sonication (Table 2-2; Set #1, Sonication B) in the center of the target region with Optison injections at 5-min intervals; these additional low-power sonications were aimed to assist the break-up of the liposomes and facilitate the release of DOX in the focal region. Figure 2-5 shows a schematic of the final ultrasound protocol tested, which allowed doxorubicin to accumulate in the brain parenchyma at therapeutic levels.

		Sonication A: BBB Disruption					*Sonication B: Increase DOX Uptake			
#	N	Pressure (MPa)	Dur (s)	Optison (mL/kg)	Rep/ Config	DOX (mg/kg)	Pressure (MPa)	Dur	Optison (mL/kg)	Rep/ Config
1	20	0.8	30 – 120	0.1	4 / square	3.0 – 5.67	0.8	40 min	0.1	1 / center
2	13	1.2	120	0.1 – 0.5	5 / square (corners + center)	5.67	1.2	60 s	0.05 – 0.25	8 / center
*Only 4/20 rats in the first set received sonication B to dramatically increase the uptake of DOX in the brain. For sonication B, Optison was administered every 5 min during the 40-min sonication.										
Dur : duration of sonication; Rep: repetition of sonication; Config: configuration of sonications										

Table 2-2: Experimental parameters for ultrasound-mediated delivery of doxorubicin to the normal rat brain.

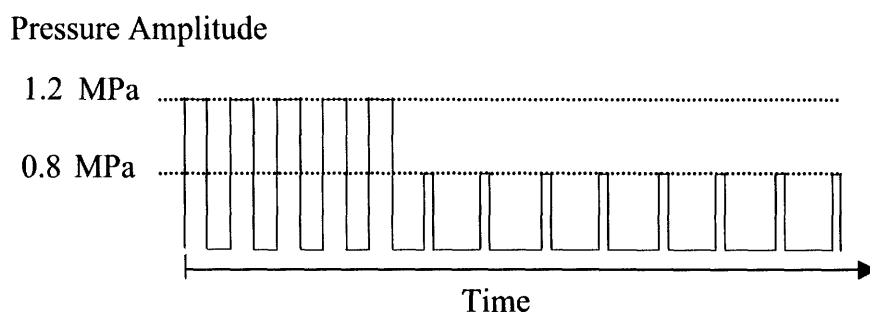


Figure 2-5: Schematic of ultrasound protocol (freq = 1.7 MHz) used to deliver doxorubicin to the rat brain at human therapeutic levels. Five overlapping 120-s pulsed sonications at 1.2 MPa were performed on the brain and spatially distributed in the corners and center of a 1.5-mm square to disrupt the BBB, followed by eight 60-s pulsed sonications in the center of the target region at 5-min intervals to increase the uptake of DOX in the brain. Sonications were accompanied by simultaneous injections of Optison microbubble contrast agent (0.1 mL/kg for first 5 sonications, 0.05 mL/kg for last 8 sonications). See Table 3-1 and text for further details.

2.3.3 Fluorometric assay

Trypan blue (ICN Biomedical, Aurora, OH; 80 mg/kg) was administered through the tail vein after the completion of the treatment and imaging session to confirm successful BBB disruption and to mark the target site of sonication for tissue harvesting. Each animal was put into a state of deep anesthesia with an overdose of ketamine and xylazine. To flush unabsorbed DOX from the cerebral vasculature, the brain was perfused by transcardiac methods with normal saline 3.5 h after the last sonication. The site of BBB disruption, identifiable by its trypan blue stain, was harvested along with its contralateral counterpart for control. The concentration of DOX of each tissue sample was determined by taking the average of at least three fluorometric readings on a benchtop fluorometer.

2.3.3.1 Extraction and quantification of doxorubicin

A preparation of acidified alcohol (0.3 N HCl in 50% EtOH) was used to extract DOX from harvested tissue samples for fluorometric quantification (Bachur 1970). For

these minute samples, we assumed the tissue density was approximately 1 g/cm³. Thus, the mass of each sample was equal to its volume. The mass of each sample was measured and cut down³ until it reached the appropriate size of ~0.020 - 0.025 g.⁴ Each sample was put into a 1.5-mL centrifuge tube with 20 volumes (400-500 μ L) of acidified alcohol, then homogenized with a motorized pestle, set in refrigerator at 4 deg C for 24 h. Samples were then centrifuged at 16,000 \times g for 25 min at 4 deg C. The supernatant was extracted for immediate fluorometric reading or stored at -20 deg C (Bachur 1970).

2.3.4 Statistical analysis

Sonicated and contralateral control paired samples were compared using a two-tailed paired Student's *t*-test. Values of $p < 0.05$ were considered statistically significant. Additional analyses included least-squares linear regression and calculation of correlation coefficients.

2.3.5 Effect of microbubble concentration on DOX delivery to the brain

In the second set of experiments, the effect of Optison dose on the amount of DOX delivered to the brain was investigated in 13 rats for a fixed ultrasound exposure scheme. For each rat in this set, the ultrasound protocol consisted of five 120-s

³ For reduction of the sample size, outer edges were cut to preserve the center of the focus, which was likely to exhibit the greatest BBB permeability and the highest concentration of DOX.

sonications at 0.6 W (Table 2-2; Set #2, Sonication A) and eight 60-s sonications at 0.3 W (Table 2-2; Set #2, Sonication B).

The first five sonications for BBB disruption were spatially distributed in the four corners and center of a 1.5-mm square and accompanied by 0.1, 0.2, or 0.5 mL/kg Optison injections, while the last eight sonications applied to the center of the target region for increase DOX delivery were accompanied by 0.05, 0.10, or 0.25 mL/kg Optison injections, respectively. As before, DOX was administered i.v. in bolus injections immediately after the Optison injections during the first five sonications for BBB disruption, for a total DOX dose of 5.7 mg/kg.

2.3.6 Histologic analysis

The brains of six animals (two animals per Optison dose) which were treated with ultrasound but without DOX were examined to evaluate the histologic effects of the ultrasound protocol on brain tissue. In addition, the brains of two animals were examined one week after treatment with sonications accompanied by 0.1 mL/kg Optison injections (the lowest Optison dose) and DOX. Histologic specimens were fixed in formalin and prepared with H&E staining as before.

⁴ These values were chosen to ensure that the addition of 20 volumes of acidified alcohol did not exceed the capacity of the 1.5-mL centrifuge tube so that no spillage occurred during homogenization, and that the extracted supernatant was greater than the minimum volume of 250 μ L of the fluorometric system.

2.3.7 Fluorescence imaging

To visualize the distribution of DOX in the brain after treatment with ultrasound-induced focal BBB disruption (with 0.2 mL/kg Optison injections) and intravenous DOX administration, volumetric projections of whole rat brains were obtained using a multi-spectral small animal imaging system (Maestro; Cambridge Research and Instrumentation, Woburn, Massachusetts; version 2.0.4; Excitation: 465 nm; Emission detection: 365-700 nm; 120-150 ms exposure), which has the ability to identify contributions from multiple components by linear unmixing of their spectral signatures. Spectral data were also obtained for doxorubicin, trypan blue, and autofluorescence of a brain treated with focused ultrasound but without DOX or trypan blue.

Brains were then sectioned at 50 μ m and representative sections were mounted and imaged using a Zeiss LSM 510 confocal laser scanning microscope (Carl Zeiss, Jena, Germany) with a 25x or 63x objective and two-photon excitation at 800 nm using a femtosecond-pulsed, mode-locked Ti:Sapphire laser (Chameleon; Coherent Inc, Santa Clara, California). Emission was collected with the META detector (Carl Zeiss, Jena, Germany), a polychromatic, 32-channel detector for rapid acquisition of multiple wavelengths.

2.4 Therapeutic efficacy of ultrasound-enhanced chemotherapy in a rodent model of aggressive glioma

After a method to deliver therapeutic levels of doxorubicin to the brain was developed, the therapeutic efficacy of the technique was investigated in rats with implanted aggressive glioma.

2.4.1 Cell culture

9L gliosarcoma cells were obtained from the University of California–San Francisco/ Neurosurgery Tissue Bank. Cells were cultivated in Minimum Essential Medium with Earle’s salts, supplemented with 10% fetal calf serum, 1% L-glutamine, 1% MEM nonessential amino acids, and 0.1% gentamicin (10% FCS-MEM) in a 5% CO₂ chamber held at 37 deg C.

2.4.2 Tumor implantation

In the anesthetized rat, the dorsal surface of the skull was sterilized with an iodine swab. A 1-cm linear skin incision was placed over the bregma and a 1-mm burr hole was drilled into the skull approximately 2 mm lateral to the bregma. A 10-μL gas-tight syringe (Hamilton, Reno, Nevada) was used to inject $(0.5\text{--}1) \times 10^5$ 9L rat gliosarcoma (9L GL) cells suspended in 2–4 μL 10% FCS-MEM into the right or left frontal lobe at a depth of 3.5 mm relative to the dural surface of the brain. To minimize convection at the injection site, the cell suspension was slowly injected over 5 min. Two minutes after injection, the needle was slowly retracted over an additional 5 min. The wound was rinsed with 0.9% NaCl solution and the burr hole occluded with sterile bone wax (Ethicon, Somerville, New Jersey) to prevent leakage of the cerebrospinal fluid. The skin

was then closed with 5-0 silk sutures (Ethicon, Somerville, New Jersey). The rat recovered from anesthesia under observation.

Each animal was given a one-time dose of antibiotic (Baytril, 2.5 mg/kg; Bayer HealthCare, Wayne, New Jersey) and analgesic (Buprenex, 0.05 mg/kg; Reckitt Benckiser Healthcare, Hull, England, UK) every 12 h for 24 h following surgery by i.p. administration. Sutures were removed prior to sonication, usually 5 days after surgery. MR images of the brain were acquired 7 or 8 days following implantation. Animals were included in the study if the tumor appeared to be well-circumscribed and if the larger cross-sectional diameter was within 1-3 mm, inclusive.

2.4.3 Study design

On Day 8 after implantation, each rat was randomly assigned to one of the following groups: (1) no treatment (control), (2) a single treatment with microbubble-enhanced MRI-guided focused ultrasound (FUS only), (3) a single treatment with i.v. liposomal doxorubicin (DOX only), or (4) a single treatment with microbubble-enhanced MRI-guided focused ultrasound and concurrent i.v. injections of liposomal doxorubicin (FUS+DOX). Additional MR images of the brain were acquired weekly to monitor tumor growth. Animals were followed until death, up to 55 days. Total survival times from tumor implantation until death were recorded. To minimize potential confounding factors, six animals which did not die of disease progression (i.e., animals whose tumor resorbed or stabilized) were excluded from analysis.

2.4.4 Sonications

For animals in Groups 2 (FUS only) and 4 (FUS+DOX) which received treatment with microbubble-enhanced MRI-guided focused ultrasound, each rat was laid supine over the water tank so that the dorsal surface of its head was acoustically coupled to the transducer with degassed, deionized water. Pre-sonication images of the brain were acquired to determine the size and coordinates of the tumor. The transducer was repositioned to align its focus with the tumor, which was then exposed to pulsed ultrasound (pressure amplitude: 1.2 MPa, burst length: 10 ms, pulse repetition frequency: 1 Hz, duration: 60–120 s; five sonications in square formation; see (17) for further detail).

At the time of this study, the ultrasonographic contrast agent Optison was not commercially available. Therefore, another contrast agent (Definity, 0.01–0.02 mL/kg; Bristol-Myers Squibb, New York, New York) containing perflutren lipid microspheres (mean diameter, 1.1–3.3 μm) was used to achieve the cavitation effect for BBB disruption. Definity was activated by shaking the vial for 45 s using Vialmix (Bristol-Myers Squibb Medical Imaging, North Billerica, Massachusetts) and diluted to 0.1x normal strength (maximum concentration, 1.2×10^9 bubbles per mL) with a solution of 0.01 M phosphate buffer, 0.0027 M KCl, and 0.137 M NaCl. At the start of sonication, a bolus of the diluted contrast agent was injected simultaneously into the catheterized tail vein, followed by a 0.2-mL flush with 0.9% NaCl solution. The transducer was then moved to its new position and the procedure repeated every 5 min until the entire cross-sectional area of the tumor and its margins had been exposed to the acoustic focus, usually 5–9 sonications in total with the focal spot spacing of 1 mm. Contrast-enhanced MR images with one-half dose of Magnevist MR contrast agent (0.125-mL/kg) were

obtained immediately following the first two exposures, which were aimed 1 mm outside of the tumor, to confirm the *in vivo* location of the acoustic focus relative to the tumor prior to treatment.

2.4.5 Chemotherapy

Animals in Groups 3 (DOX only) and 4 (FUS+DOX) received single-agent intravenous chemotherapy with doxorubicin hydrochloride encapsulated in long-circulating pegylated liposomes (Doxil; Ortho-Biotech, Bridgewater, New Jersey). Each rat was administered 5 slow bolus injections of DOX followed by 0.2 mL 0.9% NaCl solution into the catheterized tail vein at 5-min intervals, for a total dose of 5.67 mg/kg. For the animals in Group 4, the DOX injections immediately followed the administration of Definity microbubble contrast agent and were concurrent with ultrasound exposure.

2.4.6 Magnetic resonance imaging

Additional images were acquired in animals with implanted glioma. To determine the size and location of the tumor prior to sonication, two-dimensional T2-weighted fast spin-echo images of the brain (TR/TE: 2000/91 ms; ETL: 8; matrix size: 256 x 256; slice thickness/spacing: 1.5 mm/interleaved; FOV: 8 cm; NEX: 2; FA: 90 degrees) were acquired in three orthogonal planes.

To show the baseline contrast enhancement of the tumor prior to ultrasound exposure (Figure 2-6, left), two-dimensional T1-weighted FSE images of the tumor (TR/TE: 500/13 ms; ETL: 4; matrix size: 256 x 256; slice thickness: 1.5 mm; FOV: 8 cm; NEX: 4; FA: 90 deg) were acquired in the plane perpendicular to the direction of ultrasound propagation and then repeated after i.v. administration of gadopentatate dimeglumine MR contrast agent (Magnevist; Bayer HealthCare, Wayne, New Jersey;

0.25 mL/kg). After treatment with ultrasound was completed, additional contrast-enhanced T1-weighted FSE images were acquired to confirm successful ultrasound-induced BBB disruption in and around the tumor (Figure 2-6, right).

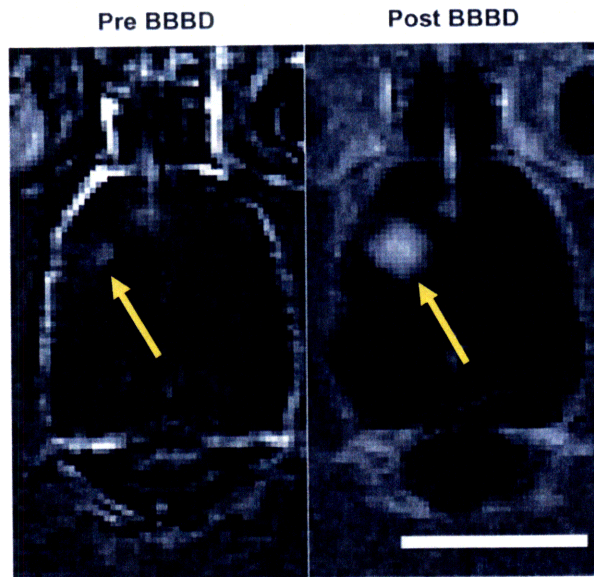


Figure 2-6: Contrast-enhanced T1-weighted magnetic resonance images of the rat brain before (left) and after (right) ultrasound-induced BBB disruption around the tumor (arrows) showed increased penetration of MR contrast agent through the BBB in the targeted area after sonication. Scale bar: 10 mm

To assess the successful implantation and viability of the tumor and to track tumor growth, additional images were acquired using a 4.7-Tesla small animal MRI scanner (BioSpec Avance; Bruker, Billerica, Massachusetts) with a 33-cm diameter bore and a 7-cm diameter RF ^1H birdcage volume coil. T2-weighted rapid acquisition with relaxation enhancement (RARE) images of the brain (TR/TE: 2000/85 ms; ETL: 8; matrix size: 256 x 256; slice thickness: 1.5 mm; FOV: 8 cm; NEX: 2; FA: 90 degrees) were acquired before treatment on post-implantation Day 7 or 8 and weekly after treatment. The implantation was deemed successful if the tumor was well-circumscribed and if the larger cross-sectional diameter was within 1-3 mm, inclusive.

2.4.7 Image analysis

The size of the tumor was evaluated with image analysis software written in-house using MATLAB (MathWorks, Natick, MA). Tumor volumes V were calculated using an ellipsoid approximation

$$V \approx \frac{4}{3} \pi \left(\frac{1}{2} \right)^3 abc \quad (3)$$

where a , b , and c are the maximum diameters of the tumor measured in three orthogonal planes on two-dimensional T2-weighted MR images. Least-squares nonlinear regression analyses were performed to compare the rate of tumor growth between groups. For animals for which MRI data were acquired on at least three different days, tumor volumes were fit using an exponential model of the form

$$V = Ae^{kt} \quad (4)$$

where A and k are constant parameters and t is the time in days after implantation. Tumor volume doubling time $T_{1/2}$ was then calculated for each animal using the equation

$$T_{1/2} = \frac{\ln(2)}{k} \quad (5)$$

2.4.8 Survival analysis

Population survival curves were also plotted using the Kaplan-Meier method (239). Survival curves were compared between groups using the Log-Rank test. Statistical analyses were performed using either GraphPad Prism version 5.01 for Windows (GraphPad Software, San Diego, California) or Excel 2002 (Microsoft Corporation, Redmond, Washington). The Bonferroni method (240) was used to compare multiple pairs of groups. The significance level for the family of comparisons was set at

0.05. Since there are four treatment groups (including control) with six possible paired comparisons, pairwise p values less than the Bonferroni-corrected threshold of $0.05/6 = 0.0083$ were considered statistically significant.

2.4.9 Histologic analysis

For illustrative purposes, the brains of three animals were examined to compare the histologic effects of different treatments. As with those in the survival study, these animals were randomly assigned on post-implantation Day 8 to one of Groups 1 (control), 3 (DOX only), or 4 (FUS+DOX). Forty-eight hours after treatment, the animals were euthanized by transcardiac perfusion with 0.9% NaCl solution followed by 10% phosphate-buffered formalin while under deep anesthesia with ketamine and xylazine. Their brains were harvested and fixed in formalin; tissue blocks containing the tumor were embedded in paraffin and cut into 6- μ m serial sections perpendicular to the direction of ultrasound propagation. Every thirtieth section was stained with hemotoxylin and eosin (H&E) for examination by light microscopy.

3 Blood-brain barrier disruption using transcranial MRI-guided focused ultrasound⁵

3.1 Results

3.1.1 *Visual confirmation of ultrasound-induced BBB disruption*

In order to eventually deliver DOX to the brain in a targeted manner, we first investigated the use of MRI-guided focused ultrasound to induce local BBB disruption in the rat brain when transmitted through the intact skull. Successful BBB disruption was confirmed by localized regions of increased signal intensity on T1-weighted MR images of the brain, due to the penetration of the MR contrast agent through the BBB (Figure 3-1, *left*). In addition, diffusion of trypan blue into the brain parenchyma marked the site of BBB disruption in harvested tissue samples (Figure 3-1, *right*).

3.1.2 *Threshold response of ultrasound-induced BBB disruption*

In 146 sonicated locations in the four quadrants of the brain, we observed a threshold response to the applied focused ultrasound. BBB opening was consistently achieved when we applied focused ultrasound with pressure amplitudes of 1.2 MPa or greater (Figure 3-2). This value was therefore used to induce BBB disruption in

⁵ Published in Treat *et al.* (2007) Int J Cancer and reproduced with permission from Wiley-Liss, Inc.

subsequent DOX delivery experiments. At pressure amplitudes below 1.2 MPa, the BBB was successfully opened, as measured by MRI signal enhancement, in some locations but not in all.

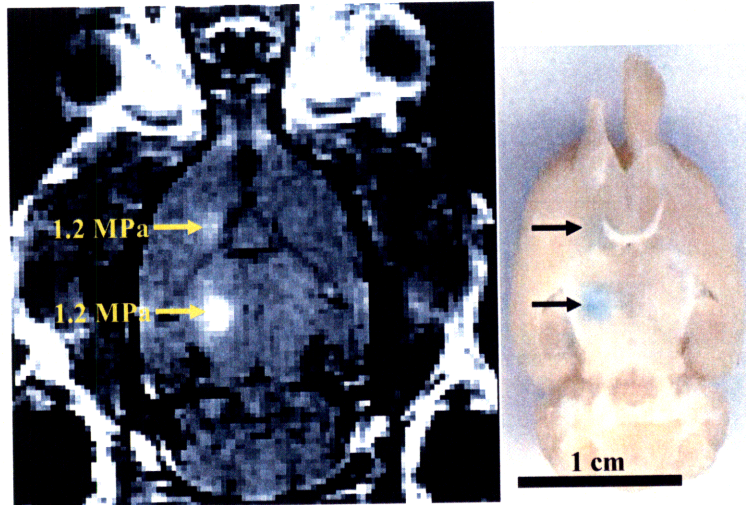


Figure 3-1: Confirmation of ultrasound-induced localized BBB disruption in the rat brain by MRI and by trypan blue staining of the affected area. *Left*, T1-weighted contrast-enhanced fast spin-echo image of a rat brain exposed in two locations to FUS at 1.2 MPa showed localized regions of MR contrast enhancement in the brain, indicating focal leakage of the MRI contrast agent (molecular weight: 938 d) through the blood-brain barrier. *Right*, Corresponding scanned rat brain section at 4-mm depth in the focal plane. Arrows indicate leakage of trypan blue from the vasculature into focal locations of the brain parenchyma.

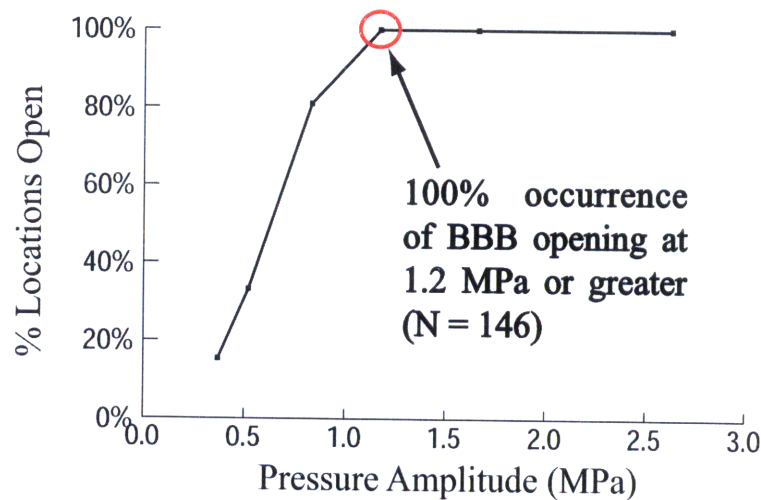


Figure 3-2: Threshold of BBB disruption induced by transcranial focused ultrasound. BBB disruption was consistently achieved when pressure amplitudes of 1.2 MPa or greater were applied to the brain through the intact rat skull.

3.1.3 Variations in sensitivity to ultrasound-induced BBB disruption by anatomical location in the brain

We noted that different locations in the brain exhibited varying responses to the applied ultrasonic energy. In locations in the posterior quadrants of the brain, such as the thalamus, hippocampus, or superior colliculus, lower pressure amplitudes were required to induce consistent BBB disruption. While over all locations in the brain, 1.2 MPa was the minimum pressure observed to achieve the desired effect, a lesser peak rarefactional pressure of 0.8 MPa was sufficient to induce reproducible BBB disruption in the posterior quadrants of the brain (Figure 3-3).

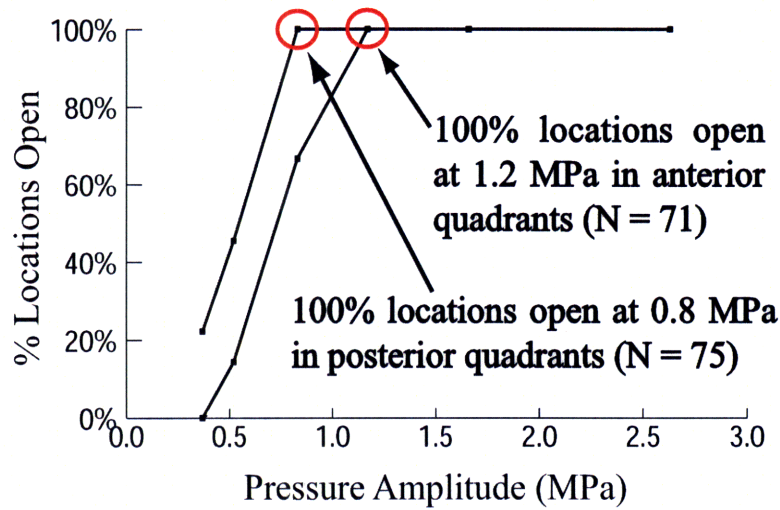


Figure 3-3: Location dependence of threshold for ultrasound-induced BBB disruption. Lower pressure amplitudes were required for consistent BBB disruption in posterior quadrants (e.g. thalamus, hippocampus, superior colliculus) than in anterior quadrants (e.g. caudate-putamen) of the rat brain.

3.1.4 MRI guidance of ultrasound-induced BBB disruption

Figure 3-4 shows the normalized MRI signal enhancement (mean \pm SD) in the sonicated region after injection of MR contrast agent as a function of peak rarefactional pressure amplitude. Signal enhancement increased with pressure, indicating that more MRI contrast agent was able to penetrate into the brain parenchyma when exposed to higher pressure amplitudes. These data indicate that MRI monitoring of ultrasound-induced BBB disruption could be useful in providing feedback on the extent of the permeability achieved during or immediately after the procedure.

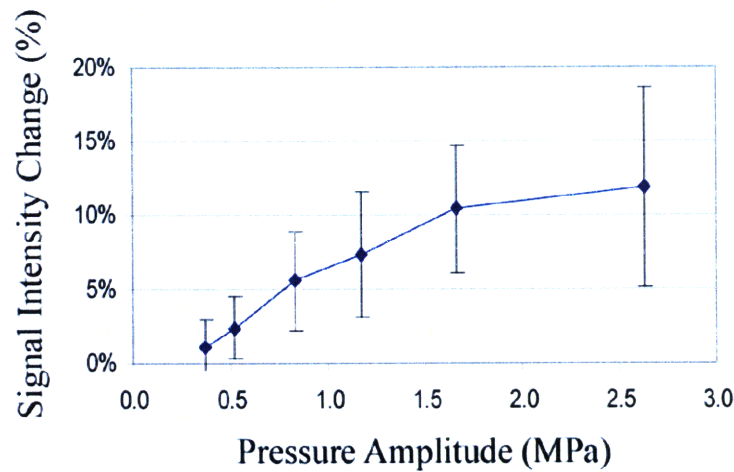


Figure 3-4: Normalized MRI signal enhancement (mean \pm SD) in the sonicated region after injection of MR contrast agent as a function of pressure amplitude. Increasing signal enhancement with pressure showed that greater BBB permeability was achieved at higher pressure amplitudes and that MRI could provide feedback on the extent of the ultrasound-induced BBB disruption.

3.1.5 Histologic results

For the single 30-s exposures used to detect the threshold of BBB disruption, no necrotic lesions were observed in eight representative locations exposed to focal pressure amplitudes from 0.5 to 1.7 MPa in two subjects administered 0.1 mL/kg Optison. The H&E-stained samples showed a few extravasated erythrocytes, too few to be characterized as hemorrhage. In a single location exposed to 1.2 MPa, two hyperchromatic neurons were identified, which could possibly indicate damage.

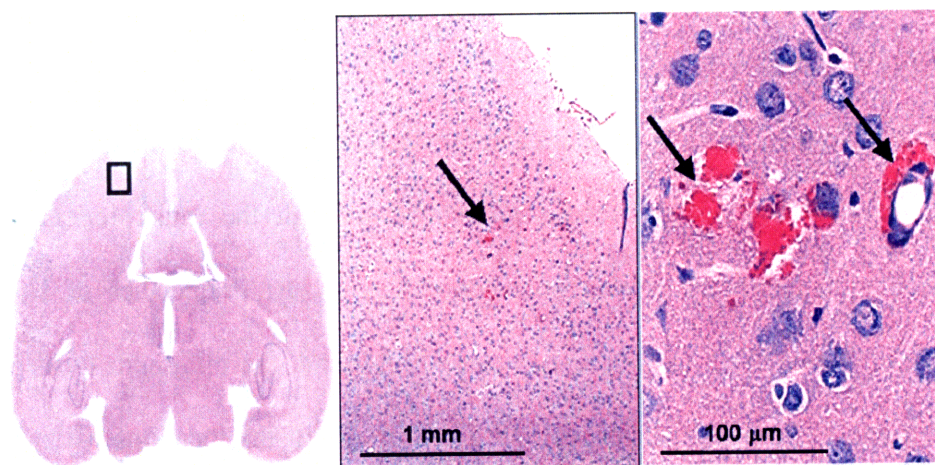


Figure 3-5: H&E-stained rat brain exposed in 4 focal locations to pressure amplitudes ranging from 0.5 MPa to 1.7 MPa. No gross or microscopic tissue damage was noted for pressure amplitudes between 0.5 to 1.2 MPa. In one location exposed to 1.7 MPa focal pressure amplitude, a few tiny extravasations of erythrocytes were noted, but too few to be characterized as hemorrhage.

3.2 Discussion

In this chapter, we demonstrated a noninvasive method for localized and transient disruption of the BBB using focused ultrasound through the intact rodent skull in combination with gas-filled microbubble contrast agent. At frequencies of 1.5 or 1.7 MHz with 30 cycles of 10-ms bursts of pulsed ultrasound, the minimum focal pressure amplitude required to consistently open the BBB in any of the locations we targeted in both the anterior and posterior quadrants of the rat brain was 1.2 MPa. These parameters formed the basis for the development of an ultrasound protocol for the targeted delivery of DOX through the BBB.

Similar to previous findings in rabbits (13), greater pressure amplitudes resulted in increased penetration of the MR contrast agent. Occasional neuronal damage was observed in histological analysis of tissue samples exposed to 1.2 MPa, whereas the lowest pressure amplitude observed to induce neuronal loss in rabbits was 2.3 MPa; rabbit data between 1.0 and 2.3 MPa were not available for comparison to rats. In the context of enhanced chemotherapy, the cell damage observed is most likely acceptable for tumor therapy since it appears minimal compared with alternative treatments such as surgical resection or ionizing radiation therapy.

The neuronal damage may be attributable, in part, to the higher microbubble concentration in the rat bloodstream (twice that in the rabbit). Alternatively, standing waves in the rat brain due to reflections between the base and the dorsal surface of the skull, which were not present in the rabbit brain after craniotomy, may have increased the actual *in vivo* pressure amplitudes beyond our estimated 1.2 MPa. Standing waves may also offer an explanation for the variation in sensitivity between sonicated locations in the

anterior and posterior brain, since the shape of the skull varies greatly between these regions. In the posterior brain, where the threshold for consistent BBB disruption was observed to be 0.8 MPa, standing waves between the virtually parallel base and dorsal surface of the skull may have rendered actual *in vivo* pressure amplitudes greater than the estimated 0.8 MPa; in the anterior brain, where the threshold for consistent BBB disruption was observed to be 1.2 MPa, the base and dorsal surface of the skull form an acute angle, so reflections off the base of the skull would be directed away from the incident direction.

We demonstrated that the distortion of the ultrasound beam by the rat skull was not significant enough to inhibit focal BBB opening. Subsequent experiments using MRI-guided focused ultrasound to aid in targeted drug delivery to brain tumors in a rodent model could thus be performed more efficiently without cranial surgery. Noninvasive transcranial application of focused ultrasound for BBB disruption would also be possible in humans with the use of a phased transducer array, which can be adjusted to compensate for the beam distortion caused by the skull, or other methods (see Section 1.3.2.1).

MRI guidance was used to target specific locations within the brain. Specifically, images in three planes provided information on the depth of the acoustic focus of our transducer relative to the dorsal surface of the brain, as well as its proximity to anatomical structures such as the lateral ventricles. The feedback provided by contrast-enhanced T1-weighted image data acquired immediately after the procedure showed that MRI signal enhancement increased with greater pressure amplitudes of applied focused ultrasound. Thus, MRI monitoring can provide important information on the extent of BBB permeability induced by focused ultrasound. In subsequent drug delivery

experiments, we explored the use of this tool to provide information on the amount of drug delivered to the brain.

4 Targeted delivery of doxorubicin to normal brain by ultrasound-mediated blood-brain barrier disruption⁶

In the previous chapter, we investigated the use of MRI-guided focused ultrasound, applied through the intact rodent skull, to achieve consistent and reproducible BBB disruption in a localized region of the brain. Once the ultrasound parameters were established for consistent BBB opening in rats with an intact cranium, we then adapted the technique to effectively deliver doxorubicin (DOX) across the BBB.

4.1 Results

4.1.1 Therapeutic Levels of Doxorubicin Delivered to the Rat Brain

After ultrasound-induced BBB disruption and intravenous administration of DOX, fluorometric measurements of DOX extracted from sonicated and contralateral control regions of harvested brains are summarized in Table 4-1 and illustrated in Figure 4-1.

⁶ Published in Treat *et al.* (2007) Int J Cancer and reproduced with permission from Wiley-Liss, Inc.

Optison dose (mL/kg)	N	Sonicated	SD	Control	SD
0.1	5	900	300	250	120
0.2	4	2400	900	230	80
0.5	4	5400	700	230	20

Table 4-1: Mean doxorubicin concentration (ng/g tissue) accumulated in sonicated and control brain tissue after ultrasound-mediated BBB disruption and i.v. chemotherapy.

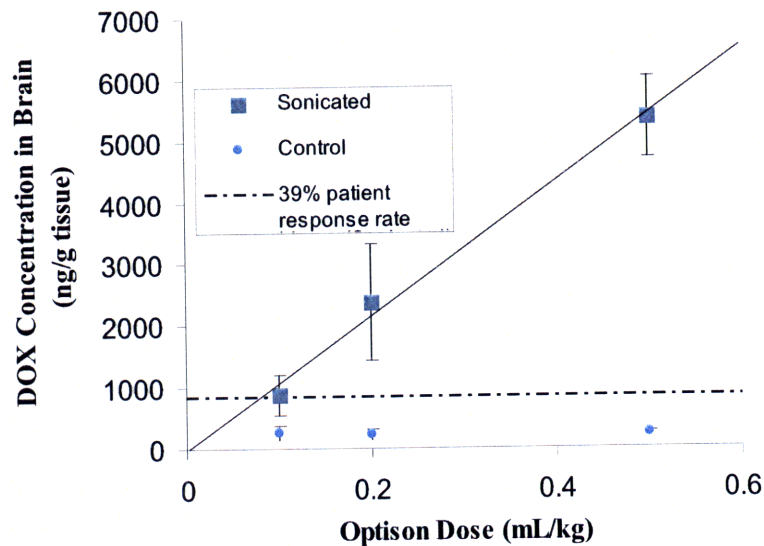


Figure 4-1: Concentration of DOX delivered to the brain as a function of Optison dose. DOX concentration (mean \pm SD) achieved in sonicated brain tissue met or exceeded the concentration shown to have a clinical response for human tumors *in vivo* (dotted line, see Cummings 1986). Note that the concentration of DOX delivered to the brain is linearly proportional to Optison dose ($r = 0.99$).

For the lowest Optison dose of 0.1 mL/kg, the DOX delivered to the brain parenchyma achieved a concentration of 900 ± 300 ng/g tissue. This concentration is within the therapeutic range of 800 ± 500 ng/g tumor *in vivo*, which was reported to correlate with a 39% clinical response rate in patients with breast carcinoma (222). At higher Optison doses of 0.2 and 0.5 mL/kg, greater DOX concentrations of 2400 ± 900 ng/g tissue and 5400 ± 700 ng/g tissue were delivered to the sonicated area, respectively.

DOX concentrations in control tissue samples remained at or below 250 ± 120 ng/g tissue for all Optison doses. Notably, the difference in DOX concentration was highly statistically significant ($p < 0.001$) for all paired sonicated and control tissue samples. In addition, the DOX concentration in sonicated tissue increased linearly with Optison dose ($r = 0.99$). All tissue DOX concentrations are reported as mean \pm SD.

4.1.2 Correlation of MRI signal enhancement and DOX delivery

As in the previous study, contrast-enhanced T1-weighted MR images acquired after ultrasound-mediated drug delivery showed localized signal enhancement in the brain due to the penetration of the MR contrast agent at the site of BBB disruption. To investigate the relationship between MRI signal enhancement and the concentration of DOX delivered to the sonicated brain tissue, the MRI signal enhancement data were fitted to a logarithmic curve as a function of tissue DOX concentration (Figure 4-2). A strong correlation ($r = 0.87$) was observed between MRI signal enhancement and the concentration of DOX delivered to the targeted site. As has been demonstrated between MRI signal intensity and concentration of contrast agent (241), the relationship between DOX concentration and MRI signal enhancement is nonlinear.

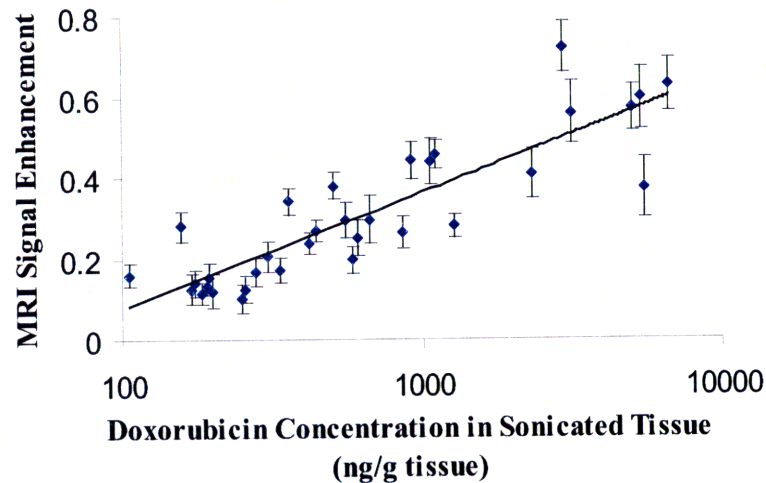


Figure 4-2: Correlation of MRI signal enhancement and DOX delivered to the targeted brain parenchyma by MRI-guided focused ultrasound (logarithmic fit; $r = 0.87$)

4.1.3 Histologic findings

For the brain samples examined which were subjected to the sonication parameters used for ultrasound-mediated DOX delivery, gross brain tissue integrity remained intact in rats administered 0.1 mL/kg Optison (Figure 4-3a). At the other extreme, severe macroscopic tissue damage was observed in rats administered 0.5 mL/kg Optison (Figure 4-3d). In rats administered the intermediate dose of 0.2 mL/kg Optison, one sample showed no macroscopic damage (Figure 4-3b), while another sample exhibited severe tissue damage (Figure 4-3c). Light microscopic examination of samples without gross damage (0.1 or 0.2 mL/kg Optison) revealed only a few extravasated erythrocytes around blood vessels (Figure 4-3e), while higher magnification of samples with gross damage (0.2 or 0.5 mL/kg Optison) showed injury characterized by pronounced vacuolation, local tissue necrosis, and neuronal and glial nuclear pyknosis (Figure 4-3f-h). The observed tissue damage was likely due to inertial cavitation (collapse of bubbles) induced by the interaction of the ultrasound and high concentration of

microbubbles; some damage may be due to the dramatic astrocytic swelling that is associated with increased BBB permeability in various models of brain injury (242, 243).

In the brains samples harvested and fixed in formalin one week after treatment with intravenous DOX and focused ultrasound accompanied by 0.1 mL/kg Optison injections, the treated and contralateral untreated hemispheres appeared comparable. There were no evident inflammatory cells, nor areas of necrosis or diminished neuronal presence, in the focal region. A few instances of increased perivascular space were observed (Figure 4-4).

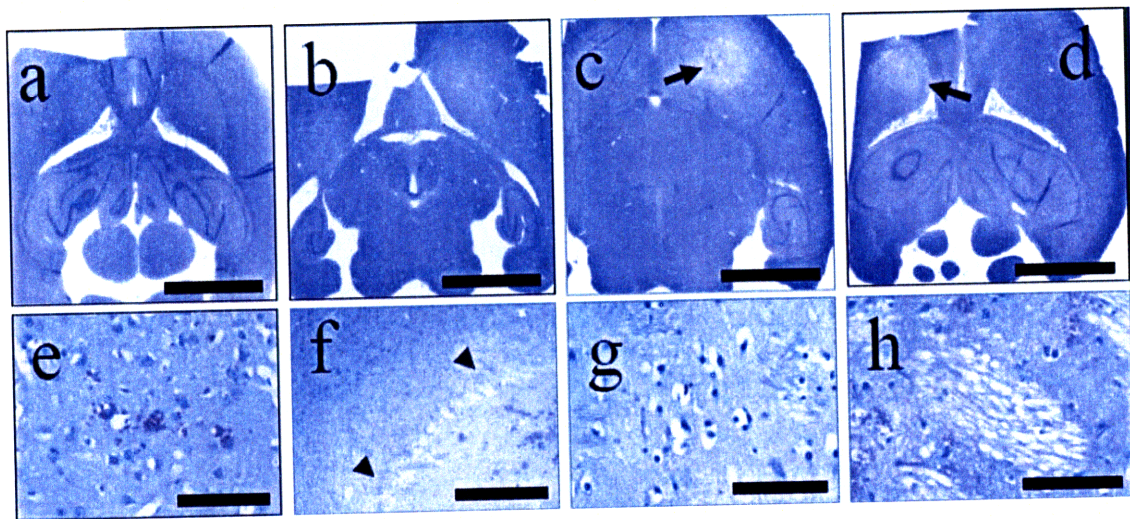


Figure 4-3: Transversal H&E-stained sections of rat brains harvested 4 h after sonication with 0.1, 0.2, or 0.5 mL/kg Optison injections (see Table I and text for parameters). (Top panel) (a) No gross tissue damage observed in sonicated brain of rats given 0.1 mL/kg Optison. In rats given 0.2 mL/kg Optison, brains (b) without and (c) with gross tissue damage were observed. (d) Severe tissue damage was observed in rats given 0.5 mL/kg Optison. (c, d) The lesion (arrow) is well-circumscribed and light-stained. (Lower panel) (e) Higher magnification of samples without macroscopic tissue damage showed extravasated erythrocytes near blood vessels. (f – h) Higher magnification of samples with macroscopic tissue damage. (f) Arrowheads indicate borders of the necrotic core surrounding the lesion. (g) Vacuolated neurons with pyknotic nuclei. (h) Separation of the myelinated nerve fibers. (g, h) Tissue in the sonicated region appears edematous. Scale bars: (a – d) 5 mm; (e) 100 μ m; (f) 0.5 mm; (g, h) 100 μ m.

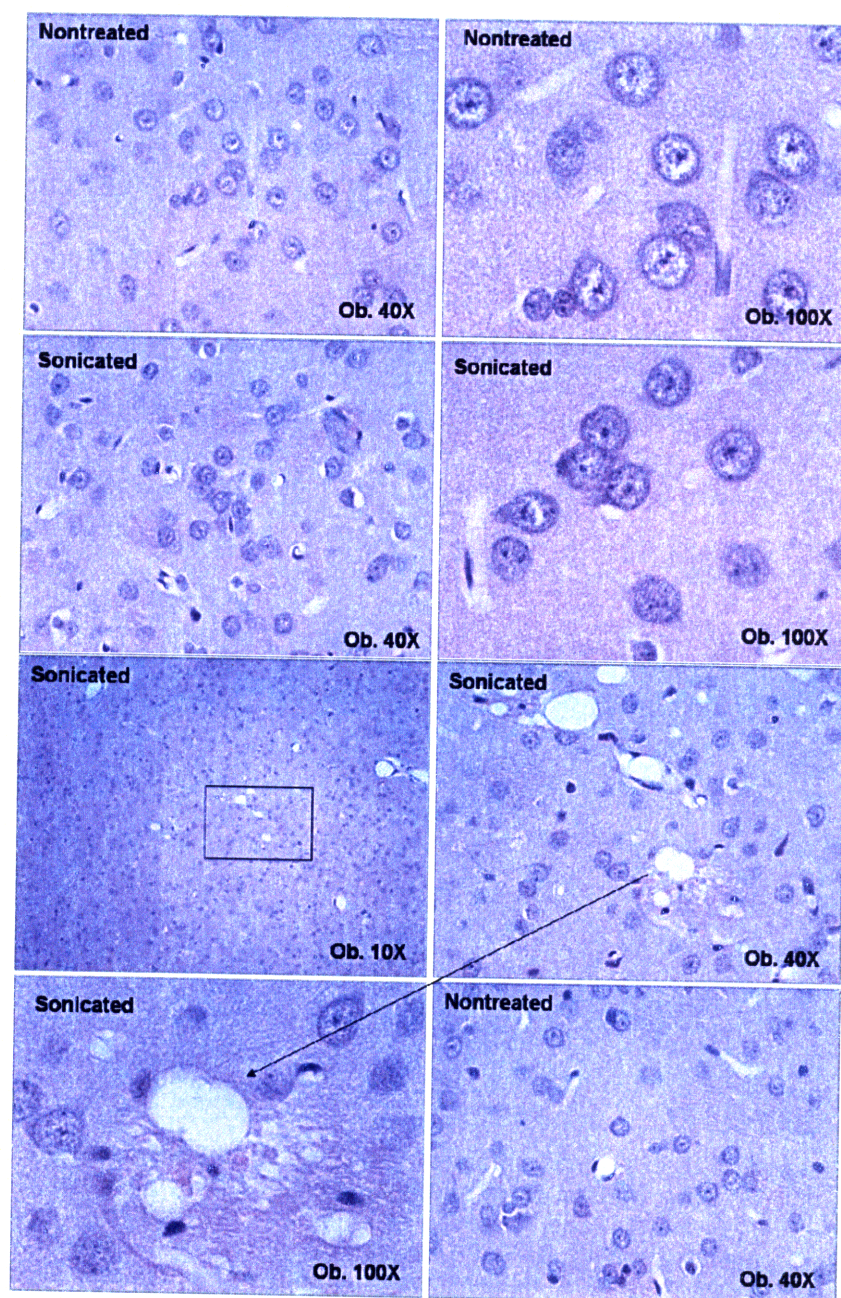


Figure 4-4: Transversal H&E-stained sections of brains of rats sacrificed 1 week after treatment with FUS+DOX using 0.1 mL/kg Optison. No inflammatory cells, nor areas of necrosis or diminished neuronal presence, were observed in the sonicated region, which was similar in appearance to the nontreated contralateral tissue, except for a few instances of increased perivascular space.

4.1.4 Distribution of DOX revealed by fluorescence images

Spectral unmixing of fluorescence images of whole rat brains (Figure 4-5) after treatment with ultrasound-induced focal BBB disruption (with 0.2 mL/kg Optison injections) and intravenous DOX administration confirmed targeted deposition of DOX in the sonicated region, further corroborating the focal contrast enhancement on T1-weighted MRI and focal trypan blue staining on histological sections. Additional diffuse DOX signal visible around the highly vascularized brainstem may indicate the presence of DOX remaining in the vasculature. In addition, spectrally unmixed images obtained by two-photon fluorescence microscopy under 25x magnification indicate that DOX co-localized in discrete areas which are likely cells. These data confirm the release of DOX from the liposomes, since the fluorescence signal of encapsulated DOX is quenched.

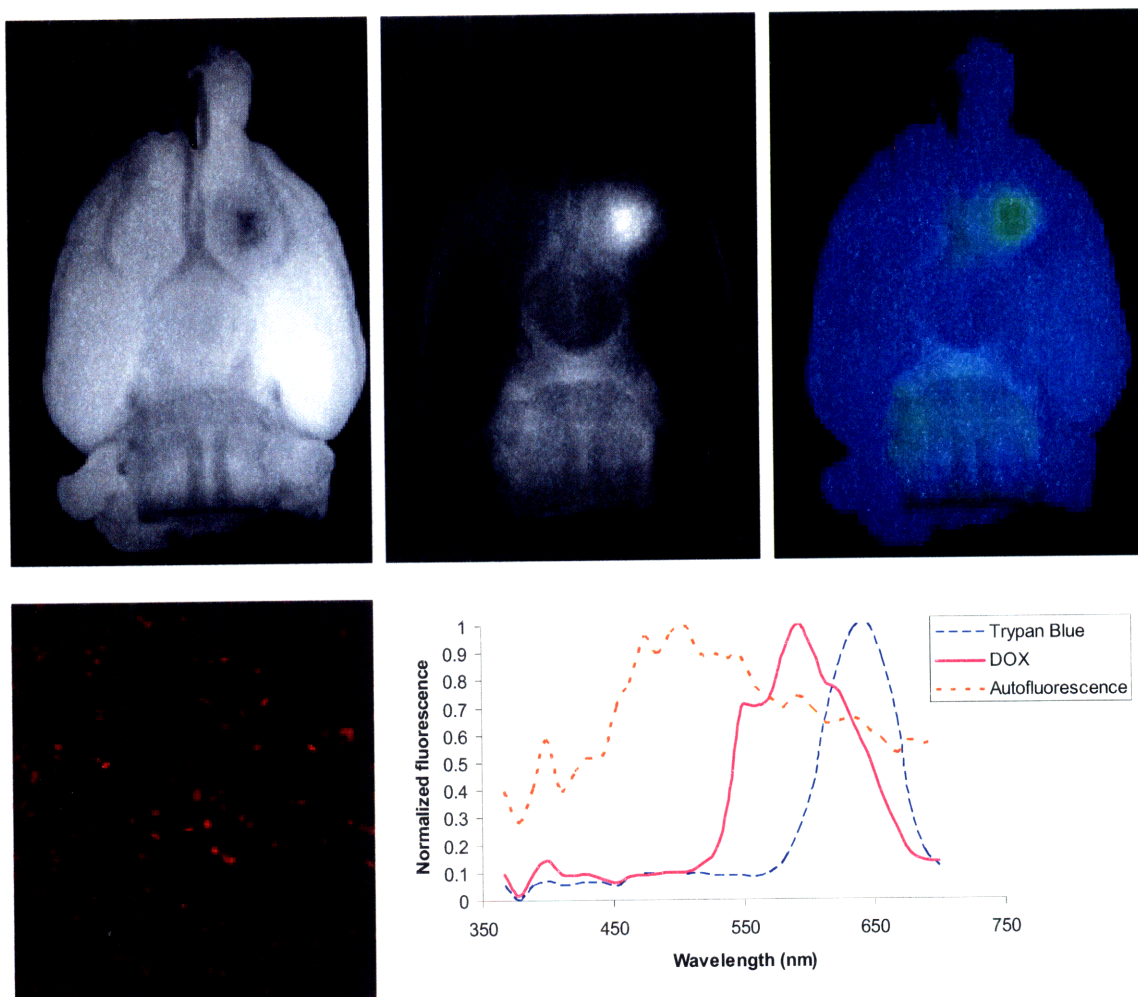


Figure 4-5: Fluorescence images showing localized distribution of DOX in sonicated region of rat brain after ultrasound-mediated BBB disruption with 0.2 mL/kg Optison and intravenous DOX administration. A–D, Spectrally unmixed fluorescence images of the rat brain showing (A) tissue autofluorescence, (B) DOX, and (C) combined tissue autofluorescence (blue) and DOX (green). D, Microscopic distribution of DOX (red) viewed with 25x objective. E, Normalized emission spectra of trypan blue, DOX, and brain tissue autofluorescence showing peaks at 645 nm, 592 nm, and 506 nm, respectively (Ex: 465 nm).

4.2 Discussion

Doxorubicin is one of the most actively used agents for systemic chemotherapy, either as a single agent or in combination therapy. However, because this Pgp substrate does not readily cross the BBB, the accumulation of DOX in brain tissue is typically insufficient to be clinically effective in the treatment of patients with primary or metastatic brain tumors (5). Although data on *in vivo* DOX concentration and cytotoxicity are difficult to obtain and largely underreported, intratumoral DOX concentrations of 819 ± 482 ng/g tumor (mean \pm SD) have been strongly correlated with partial or complete responses in 39% of breast cancer patients (222). These data further suggest that the DOX dose-response correlation (e.g. the exponential increase in percentage of patient responders with intratumoral DOX concentration) was valid for multiple human cancer types ($r = 0.90$), including breast, gastric, and colorectal carcinoma. To our knowledge, data on the relationship between DOX concentration in human glioma and patient response has not been reported.

We have demonstrated a noninvasive method for the targeted delivery of DOX through the BBB such that drug levels shown to be therapeutic in human tumors are achieved in the brain. Using MRI-guided focused ultrasound to locally disrupt the BBB and systemic administration of DOX, we achieved localized DOX concentrations in the targeted brain parenchyma in excess of reported clinical benchmarks. Importantly, MRI signal enhancement was strongly correlated with the DOX concentration in the sonicated brain, perhaps providing a means for on-line guidance of the procedure. The accumulation of DOX in non-targeted brain tissue remained low, reducing the risk of neurotoxic effects associated with DOX penetration through diffuse BBB opening by

osmotic methods (244, 245) or through attaching DOX to drugs designed to pass the barrier (75). Fluorescence microscopy results suggest that DOX colocalized with cells in the sonicated region, but it remains to be explored which cell types were involved and whether the agent gained intracellular penetration or remained on the cell membrane.

With an Optison dose of 0.1 mL/kg, the ultrasound protocol used for the delivery of therapeutic levels of DOX had only minimal vascular effects but no macroscopic tissue damage in the brain. These effects are certainly less than would be caused by the invasive procedures required for currently available methods of intratumoral delivery of chemotherapy agents (12, 55, 93). One week after treatment with ultrasound-enhanced DOX chemotherapy at this Optison dose, there was no evidence of inflammation, necrosis, or neuronal loss. Thus, our delivery of therapeutic levels of DOX by ultrasound-induced focal BBB disruption resulted in only minor acute vascular injury and did not appear to induce lasting delayed histological effects.

We delivered even greater concentrations of DOX to the brain with 0.2 and 0.5 mL/kg Optison, but the tissue damage was more significant and greater than previously seen in rabbits (13, 198), which may indicate the presence of inertial cavitation during BBB disruption (200). Direct comparisons are difficult, however, due to variations in Optison dose and in the duration of ultrasound exposure. Since macroscopic tissue damage was observed in some but not all of the rats sonicated with 0.2 mL Optison, we postulate that it would be possible to achieve comparable DOX delivery with lesser tissue effects by using lower acoustic power and prolonged exposure. Alternatively, these effects induced by greater Optison doses could be used to one's advantage in the treatment of the bulk of a solid tumor, where tissue destruction is desirable.

5 Therapeutic efficacy of ultrasound-enhanced chemotherapy in a rodent model of aggressive glioma

In the previous chapter, we confirmed that ultrasound-enhanced delivery of DOX to the normal rat brain makes it possible to achieve tissue drug concentrations at levels sufficient to have a therapeutic effect in humans. To demonstrate the therapeutic benefit of trans-BBB delivery by MRI-guided focused ultrasound *in vivo*, we examined the impact of focused-ultrasound enhanced chemotherapy on survival and on tumor growth rate in a rodent model of aggressive glioma.

5.1 Results

5.1.1 *Improved survival in rats with implanted glioma after treatment with ultrasound-enhanced chemotherapy*

We first investigated the therapeutic efficacy of ultrasound-enhanced chemotherapy by comparing the population survival curves between groups of rats with implanted 9L GL tumors which received different treatments. Figure 5-1 shows the Kaplan-Meier estimates of survival in rats which received (1) no treatment (N = 13; black solid line), (2) FUS only (N = 9; blue dotted line), (3) DOX only (N = 17; red dashed line), or (4) FUS+DOX (N = 24; purple dotted-dashed line). Six animals treated with FUS (either by itself or in combination with DOX) did not recover after treatment, possibly due to prolonged time under anesthesia; these animals are considered lost to follow-up (censored) after Day 8. Four animals treated with FUS+DOX, in which the tumor had resolved or stabilized, survived beyond 55 days. However, because such

resolution was also observed in two control animals, stable disease was considered a potential confounding factor; all six animals were excluded from the survival analysis.

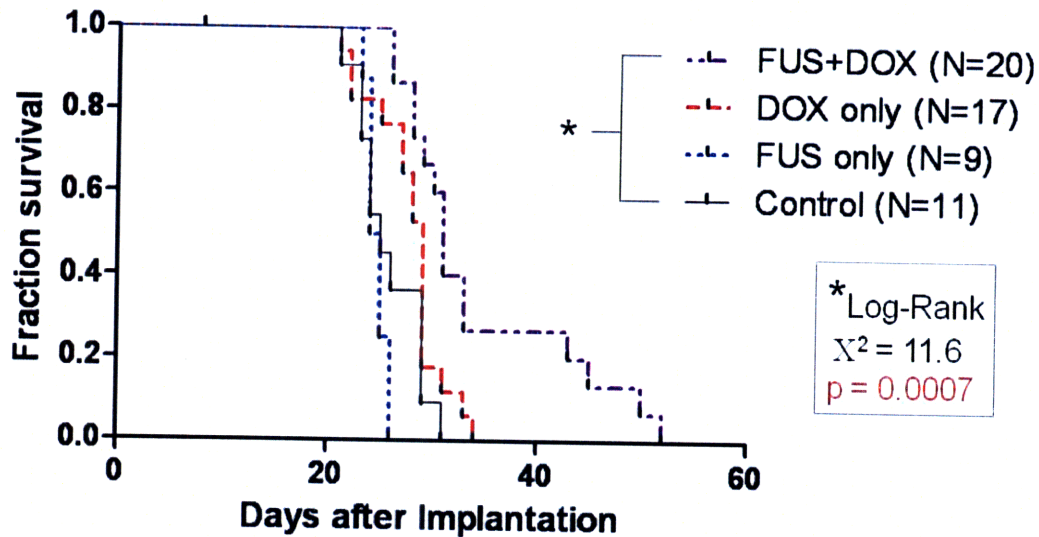


Figure 5-1: Fraction of survival (Kaplan-Meier plot) of rats with intracranially implanted 9L gliosarcoma after treatment on day 8 with one of the following: microbubble-enhanced focused ultrasound (FUS only), i.v. administration of 5.67 mg/kg liposomal doxorubicin (DOX only), or microbubble-enhanced focused ultrasound and i.v. administration of 5.67 mg/kg liposomal doxorubicin (FUS+DOX). Rats which received a single treatment of FUS+DOX had a 24% greater median survival time than nontreated rats (Log-Rank $X^2 = 11.61$; $p = 0.0007$) and a greater proportion in long-term survivors; the other treatment groups were not significantly different from the control group.

The median survival times for each group were 25, 25, 29, and 31 days, respectively. The Log-Rank test for the groups 2, 3, and 4 compared to the nontreated reference group yields $X^2 = 1.25$ ($p = 0.26$), 1.86 ($p = 0.17$), and 11.61 ($p = 0.0007$), respectively. Thus, rats which received a single treatment of FUS+DOX had a 24% greater median survival time than nontreated rats, and the difference was highly significant ($p = 0.0007$). In contrast, rats which received DOX only had a 16% greater median survival time than nontreated rats, but the difference was not statistically

significant ($p = 0.17$). In addition, the proportion of long-term (> 40 days) survivors in the FUS+DOX group was 26.7%, whereas no rats in the other three groups survived beyond 34 days. There was no significant difference in survival between animals treated with FUS only and nontreated controls.

5.1.2 Delayed tumor growth in rats with implanted glioma after treatment with ultrasound-enhanced chemotherapy

Images of the brain obtained weekly before and after treatment were used to compare the effects of each treatment on glioma growth rate. Figure 3 shows an example of T2-weighted MR images of the brain of a rat treated with FUS+DOX (top row) and of one treated with DOX only (bottom row). On a week-by-week basis, the rat treated with FUS+DOX seemed to exhibit a tumor growth pattern comparable to that of the rat treated with DOX only until two weeks after treatment, when noticeable differences in the growth patterns emerged. While the tumor in the DOX-only-treated rat continued to grow exponentially ($R^2 = 0.999$) even after treatment, tumor growth in the FUS+DOX-treated rat was visibly delayed, allowing the ultrasound-enhanced treated rat to survive longer.

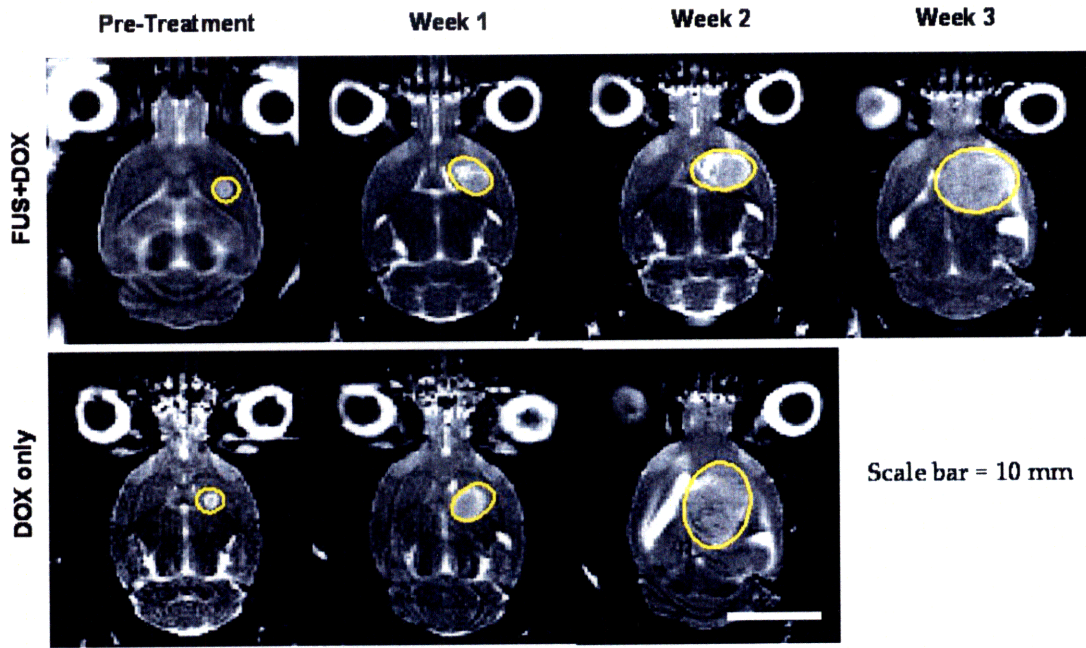


Figure 5-2: T2-weighted magnetic resonance images of a rat brain with implanted 9L gliosarcoma (outlined) before and 1, 2, and 3 weeks after treatment with focused ultrasound and i.v. liposomal doxorubicin (FUS+DOX; top row) or treatment with i.v. liposomal doxorubicin (DOX only; bottom row). While the tumor in the rat treated with DOX only continued to grow exponentially ($R^2 = 0.999$) even after treatment, tumor growth in the rat treated with FUS+DOX was visibly slowed in comparison.

To further investigate this anecdotal evidence, exponential growth time constants for each rat were calculated from least-squares regression analyses. Animals treated with FUS+DOX exhibited an average tumor volume doubling time ($T_{1/2} \pm \text{SD}$) of 3.7 ± 0.5 days, whereas those treated with DOX only had a doubling time $T_{1/2} = 2.7 \pm 0.4$ days. Animals who received FUS only or no treatment exhibited similar tumor growth rates as the latter group with $T_{1/2} = 2.2 \pm 0.3$ days and $T_{1/2} = 2.3 \pm 0.3$ days, respectively. These results confirmed that rats treated with FUS+DOX had longer average tumor volume doubling times than any other group (Figure 5-3). In all cases except one, the coefficient of determination R^2 of the exponential fit exceeded 0.94. One animal treated with

FUS+DOX was excluded from the calculation of the average doubling time ($T_{1/2} = 7.9$ days) because its tumor growth pattern after FUS+DOX treatment was not well described by an exponential fit ($R^2 = 0.44$). Thus, ultrasound-enhanced delivery of DOX appeared to slow the growth of the glioma compared to standard intravenous administration of the agent without concurrent BBB disruption.

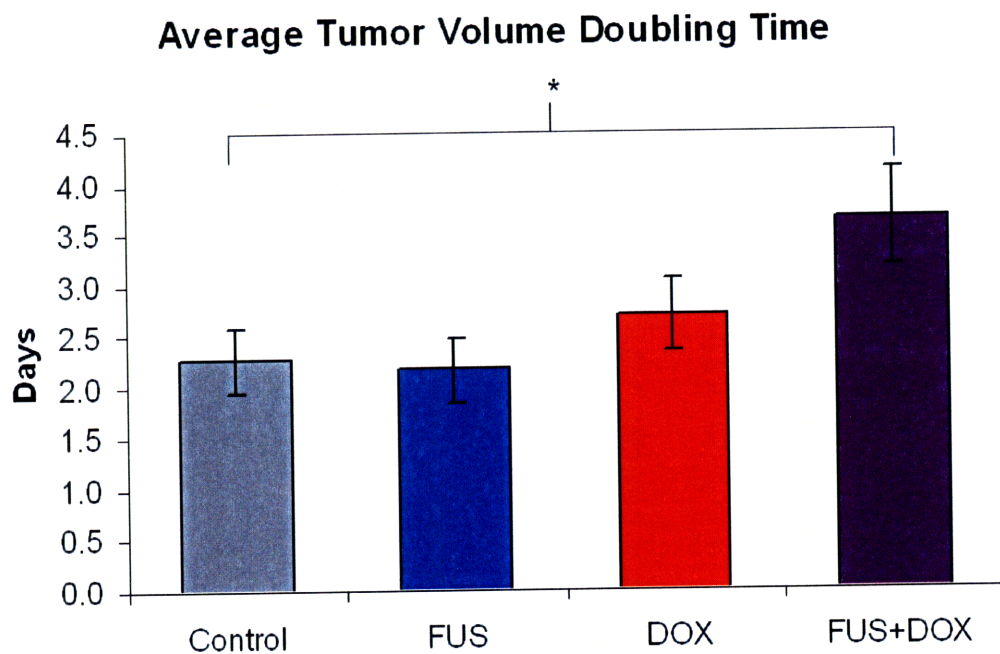


Figure 5-3: Average tumor volume doubling time in rats with intracranially implanted 9L gliosarcoma after treatment with one of preparations listed in Figure 5-1. Doubling time was calculated from exponential growth time constants determined from least-squares regression analyses. Rats treated with FUS+DOX had longer average tumor volume doubling times (3.7 ± 0.5 days) than any other group.

5.1.3 Histologic findings

Figure 5-4 shows the results of the preliminary histologic evaluation of brains from animals with implanted 9L GL tumors. At their centers, the tumors from the rat treated with DOX only and from that treated with FUS+DOX (Figure 5-4A) showed little

difference from the nontreated tumor. Tightly packed tumor cells with a few sparse necrotic foci were visible in the central regions of all samples (Figure 5-4B, arrow). Greater differences were visible at the tumor edges. The edge of the tumor treated with FUS+DOX was characterized by parenchymal vacuolation and damaged tumor cells (Figure 5-4C), unlike the tumor edges in the nontreated control animal and that treated with DOX only (Figure 5-4D), which remained intact. Damage was also noted in the tissue beyond the solid tumor in the latter sample (Figure 5-4A, arrow). Notably, in the animal treated with DOX only, undamaged infiltrating tumor cells were visible in the tissue beyond the solid tumor (Figure 5-4D, arrow) and surrounding an intact blood vessel.

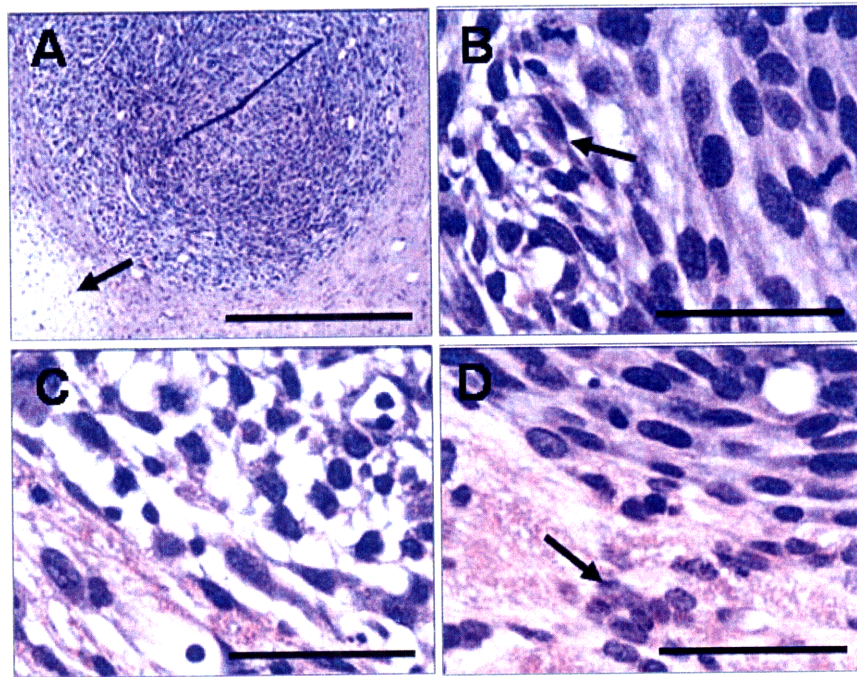


Figure 5-4: H&E-stained histologic sections of rat brains implanted with 9L gliosarcoma, harvested 48 h after treatment. **A**, Highly cellular malignant 9L gliosarcoma in an animal treated with FUS+DOX on day 8. Damage was noted in the peripheral region of the tumor and in the tissue beyond the tumor boundary (arrow). **B**, Detail of central region of **A**, showing densely packed undamaged tumor cells adjacent to focal necroses (arrow), similar to those found in the rat treated with DOX only and in the nontreated control rat. **C**, Detail of peripheral region of **A**, showing parenchymal vacuolation and damaged tumor cells. **D**, Detail of a similar tumor in a rat treated with DOX only, showing intact tissue at the tumor edge and undamaged infiltrating tumor cells in the tissue beyond the solid tumor (arrow). Scale bars: **A**, 500 μm ; **B-D**, 50 μm .

5.2 Discussion

In the previous chapter on drug quantification, we demonstrated that it is possible to achieve therapeutic levels of doxorubicin in localized areas of the brain by using MRI-guided focused ultrasound to induce transient BBB disruption in rats (17). In the present study of therapeutic impact, we have shown that targeted delivery of doxorubicin by ultrasound-induced BBB disruption significantly improves survival and slows disease progression in rats with aggressive glioma. Rats who received ultrasound-enhanced chemotherapy showed a modest but highly significant increase in median survival time, as well as an increase in the proportion of long-term survivors, compared to those who received stand-alone chemotherapy. In addition, follow-up MRI confirmed that rats who received the combined treatment experienced slower tumor growth with increased tumor volume doubling times.

Not surprisingly, rats treated with only intravenous doxorubicin exhibited no significant difference in survival from those who did not receive any treatment. This finding is consistent with previous studies which show that systemically administered doxorubicin has minimal impact against aggressive glioma due to poor BBB penetration (5). Similarly, rats treated with only microbubble-enhanced focused ultrasound showed no significant difference in survival from the control group. Thus, neither ultrasound nor intravenous chemotherapy was sufficient on its own to achieve the improved survival benefit observed when the two treatments were combined.

The enhanced therapeutic efficacy of the combined treatment is attributable to the augmented penetration of doxorubicin through the ultrasound-induced BBB disruption. The interaction of low-power focused ultrasound with intravascular microbubbles is

thought induce mechanical stresses on the brain microvascular endothelial wall, which can be exploited to induce focal and transient BBB opening (13). It is arguable that the histologic effects of the ultrasound at the tumor margins may have contributed to the slowed tumor growth and increased survival times observed in rats treated with ultrasound-enhanced chemotherapy. Vacuolation in the tumor margin may have inhibited growth at its proliferative edge. However, since animals who received ultrasound without chemotherapy exhibited no significant difference in survival from nontreated control animals, we believe that the ultrasound in itself would be an unlikely explanation of the improved survival effect that we observed. It is more likely that the therapeutic benefit of the ultrasound-enhanced treatment resulted primarily from the increased penetration of doxorubicin across the BBB and its accumulation in and around the tumor, thus improving the antitumoral efficacy of the systemic agent, while histologic effects may have played a secondary role, if any.

Furthermore, previous studies of focused ultrasound with Optison microbubble contrast agent in normal brain tissue have shown that it is possible to achieve BBB disruption without significant histologic effects up to one month after sonication (198, 200). In these studies, BBB disruption could be achieved without tissue destruction or capillary extravasation of erythrocytes in the absence of wideband emission, a signature of inertial cavitation *in vivo* (150); when BBB disruption was accompanied by wideband emission, minor capillary extravasation of erythrocytes after acute exposure was observed (200). Although the histologic effects observed in the current study were more severe than in previous studies, it should be noted that the ultrasound protocol used in this study of therapeutic efficacy has not yet been optimized for drug delivery. In addition,

extensive parametric studies on the threshold for tissue damage using focused ultrasound and Definity microbubble contrast agent have not yet been performed. It remains to be explored whether and how the effects of microbubble-enhanced focused ultrasound in neoplastic tissue differs from its effects in normal brain tissue.

While previous studies have illustrated the feasibility of drug delivery across the BBB using MRI-guided focused ultrasound, this study is the first to demonstrate its therapeutic benefit *in vivo*. Although the increase in survival time is modest, it should be noted that it was achieved here with only a single treatment with ultrasound and a single dose of doxorubicin, whereas a typical chemotherapy regimen consists of multiple doses over time. We postulate that the therapeutic benefit of MRI-guided focused ultrasound-enhanced chemotherapy could be increased with repeated administration. Since the BBB disruption induced by focused ultrasound has been shown to be transient and reversible (195), repeated use of this technique in the clinical setting should be possible.

6 Conclusions and recommendations for future work

6.1 Conclusions

The central nervous system is highly sensitive to changes in the extracellular environment. Because the interstitial concentrations of ions and other molecules must be carefully controlled, capillary walls in the CNS are much less permeable than elsewhere in the body. Their specialized endothelium, which separates the brain from its blood supply, performs the very important function of policing what can and cannot enter the brain from systemic circulation. While this blood-brain barrier maintains the stable chemical environment necessary for normal brain function, it also poses a nontrivial obstacle to neuropharmacological interventions. Only drugs less than 400-500 Daltons with high lipid solubility are able to cross the intact BBB, which precludes the use of virtually all large-molecule drugs and greater than 98% of small-molecule drugs (246). Thus, a method to overcome this obstacle in a safe, reliable, and cost-effective manner could radically alter the way we treat patients with CNS disorders today.

Doxorubicin is one such antineoplastic agent whose use in the CNS is stymied by its inability to cross the intact BBB. It is widely used in both single-agent and combination chemotherapy to treat extracranial cancers, but the BBB renders it ineffective against malignancies within the brain. Although it has been shown to be effective against malignant glioma both *in vitro* (223) and *in vivo* when injected directly into the tumor (92, 247), standard systemic administration of this potent cytotoxic agent results in poor accumulation in glioma tissue (5). The evidence suggests that if the agent had a means of penetrating the BBB and if its accumulation in the brain could be

increased to therapeutic levels, then its clinical use could have a profound impact on survival in patients afflicted with malignant brain tumors of either primary or metastatic origin.

In this thesis, we have developed a technique to enable trans-BBB localized drug delivery using MRI-guided focused ultrasound and demonstrated its potential for impact using doxorubicin as our agent of interest. Previous studies in rabbits have demonstrated that low-intensity pulsed ultrasound, in combination with an ultrasonographic contrast agent containing gas-filled microbubbles, could be used to reliably induce focal disruption of the BBB to allow the passage of molecules which would not otherwise penetrate into the brain (13). To further develop this technique for drug delivery applications in a pre-clinical rodent model, we investigated the ultrasonic parameters needed to achieve consistent, localized disruption of the BBB in rats with an intact cranium. Using frequencies of 1.5 or 1.7 MHz with 30 repetitions of one 10-ms pulse per second, we determined that focal BBB opening was consistently achieved with transcranial focal pressures of 1.2 MPa or greater; locations in the posterior brain exhibited consistent BBB disruption with applied focal pressures of 0.8 MPa or greater. In addition, we demonstrated an association between applied pressure amplitude and MRI signal enhancement in sonicated locations in the brain, which provides evidence of the expediency of MR image guidance and monitoring. Furthermore, the study described in Chapter 2 confirmed our ability to focus the acoustic energy through the intact rat skull despite its attenuating effects. These findings helped to establish the framework for subsequent drug delivery experiments and allowed us to proceed without the additional step of performing an invasive and time-consuming craniotomy for each animal.

Based on the parameters determined for transcranial ultrasound-induced BBB disruption, we developed a protocol for the targeted delivery of doxorubicin to the brain in normal, healthy rats. Combined with systemic administration of liposome-encapsulated doxorubicin, the ultrasound protocol was adapted to increase the local penetration of the agent through the BBB until its accumulation in the brain was within the range of *in vivo* drug concentrations shown to elicit a clinical response (222). We achieved local drug concentrations of 886 ± 327 ng/g tissue in the brain with minimal tissue effects, and up to 5366 ± 659 ng/g tissue with more significant tissue damage. Given that doxorubicin concentrations of 819 ± 482 ng/g tumor were measured in the excised tumors of patients with breast carcinoma and that such concentrations were shown to correlate with a 39% clinical response rate (222), our achievement of doxorubicin concentrations in the brain in excess of those achieved in patient responders reaffirms that our ultrasound-enhanced technique for trans-BBB drug delivery has real potential for clinical significance.

Importantly, the distribution of doxorubicin in the brain remained localized to the area targeted by the acoustic focus. Drug accumulation in non-targeted contralateral brain tissue was shown to be no greater than 251 ± 119 ng/g tissue and significantly lower than in areas of focal BBB disruption ($p < 0.001$). These results indicate that the accumulation of doxorubicin was concentrated in the sonicated area and that drug penetration to non-targeted areas of the brain was minimal, which would greatly reduce the risk of neurotoxic effects in patients. In addition, by showing that the MRI signal enhancement in the sonicated region correlated strongly with doxorubicin concentration in tissue ($r = 0.87$), we demonstrated the significance of combining the ultrasound technique with contrast-enhanced MRI guidance and its implications for feedback with

respect to drug penetration in the brain. Taken together, the results of Chapter 4 provide evidence that our ultrasound-enhanced drug delivery technique has the potential to enable the practical use of doxorubicin in the brain, despite its inability to penetrate the intact BBB.

In the final component of this thesis, we demonstrated that ultrasound-enhanced trans-BBB delivery of doxorubicin significantly improves the antineoplastic efficacy of the agent in a rodent model of aggressive glioma. After a single treatment with ultrasound-induced BBB opening and systemic administration of liposomal doxorubicin, glioma-bearing rats exhibited significantly longer median survival times (31 versus 25 days; $p = 0.0007$) and slower tumor growth (average tumor volume doubling time, 3.7 ± 0.5 days, versus 2.3 ± 0.3 days) than nontreated rats. In contrast, rats which received a single dose of standard intravenous liposomal doxorubicin showed no significant difference in survival or tumor growth rate. Additionally, the proportion of long-term (>40 days) survivors among rats which did not exhibit stable disease substantially increased to 26.7% after ultrasound-enhanced chemotherapy, compared to zero in both nontreated rats and in rats which received standard chemotherapy. As could be expected of our first examination of ultrasound-enhanced chemotherapy in a disease model, these preliminary survival benefits were realized in the context of severe histologic damage.

Our results described in Chapter 5 clearly show that neither ultrasound nor standard intravenous chemotherapy was sufficient on its own to achieve the improved survival benefit observed when the two treatments were combined. Since doxorubicin had little effect in the absence of ultrasound-induced BBB disruption and vice versa, the therapeutic benefit of the ultrasound-enhanced combination treatment likely resulted

from the increased penetration of doxorubicin across the BBB and its accumulation in and around the tumor. These results are particularly notable because the survival benefit was demonstrated with only a single treatment of ultrasound-enhanced chemotherapy. Repeated treatments, as typically required for clinical chemotherapy regimens, may further augment the therapeutic benefit of ultrasound-enhanced drug delivery demonstrated in this thesis. Moreover, since the protocol has not yet been optimized for drug delivery, even greater gains in therapeutic efficacy with lesser histologic sequelae should be possible. Thus, our *in vivo* demonstration of the increased antitumoral efficacy of doxorubicin resulting from ultrasound-mediated delivery across the BBB represents a major milestone in the development of this technique for neuropharmacological applications.

The advantages of using focused ultrasound to induce BBB disruption as a technique for drug delivery to the brain are numerous. The resultant opening of the BBB is temporary, completely noninvasive, spatially resolved, and generically applicable for the delivery of agents of a wide range of molecular size (up to ~150 kDa) (16, 19, 210). Its combination with MRI for guidance and monitoring allows the spatially confined delivery of the agent to be steered to a targeted region of the brain and may provide an important means of on-line feedback during drug delivery. Because the BBB presents a significant barrier in the treatment of many neurological conditions, the development of this technique for the delivery of agents across the BBB and other blood-CNS barriers would have innumerable clinical applications, including but not limited to malignant glioma.

The role of chemotherapy in the treatment of patients with brain tumors has been controversial. Individual randomized controlled clinical trials of the use of single-agent or multi-agent chemotherapy in addition to cranial irradiation have failed to demonstrate any significant improvement in median survival. However, meta-analysis has shown a significant difference in median survival in brain tumor patients who receive chemotherapy (248). Although the effect of chemotherapy on median survival is controversial, there is little doubt that chemotherapy significantly increases the proportion of long-term survivors from less than 5 percent to approximately 15-20 percent (249). This finding has been consistent across trials (1) and is consistent with our current results.

Recent developments in the identification of genetic markers linked to chemotherapeutic response (250, 251) have renewed interest in the use of chemotherapy for brain tumors with agents which can cross the BBB, such as temozolomide (252). The development of focused ultrasound-induced BBB disruption as a noninvasive method for targeted drug delivery to the brain could further reinvigorate the field by opening the door to a wide spectrum of potential neurotherapeutics which may otherwise be ruled out based on their current inability to penetrate the BBB.

The need for a safe, effective, and reliable method to deliver drugs to the brain is great. In addition to those with brain malignancies, patients afflicted with neurological or neurodegenerative conditions, such as Alzheimer's disease, Parkinson's disease, Huntington's disease, multiple sclerosis, epilepsy, stroke, aphasia, autism, chronic pain, schizophrenia, bipolar disorder, or clinical depression, are among those who could benefit from a technique to surmount the BBB. Not only could such a method render usable

many existing agents with known potency, it could also accelerate the pre-clinical screening process for new drugs and imaging probes. Thus, the development of our technique for trans-BBB drug delivery has potential for impact at multiple levels, including the basic understanding, early diagnosis, and treatment of disorders of the CNS. By confirming the significant impact of ultrasound-induced BBB disruption on the antitumoral efficacy of systemic doxorubicin, the pre-clinical data presented in this thesis provide justification for the continued development of MRI-guided focused ultrasound for trans-BBB drug delivery applications toward clinical trials.

6.2 Recommendations for future work

The long-term goal of this research is to develop a clinically viable technique for ultrasound-mediated drug delivery applications so that we may significantly improve diagnostic capabilities and therapeutic options for patients with disorders of the CNS. Much work remains before this technology will be practical for clinical use. Further quantitative studies are needed to optimize the ultrasound parameters for maximum efficiency, to optimize the dose delivery schedule for any given application, and to ensure the safety of the application. In addition, a better understanding of the physiological response of the brain to ultrasound exposure would enable us to refine the technique for improved efficacy and advance its development toward clinical trials.

Chapter 5 of this thesis presents some of the earliest data on the *in vivo* therapeutic efficacy of ultrasound-mediated BBB disruption and CNS drug delivery in a tumor model. However, because it is one of the first investigations using ultrasound in live tumors, a comprehensive study of any differences in the physical and biological effects of focused ultrasound in tumors and normal brain tissue has not yet been conducted. The extensive investigations on the effects of microbubble-enhanced focused ultrasound on normal brain tissue and vasculature may not necessarily be translatable to pathological tissue and vasculature. Since tumor vasculature is known to be abnormal and leaky (253), the interaction of ultrasound and microbubbles at the blood vessel wall may result in different effects in the so-called blood-tumor barrier than in the normal blood-brain barrier. To improve our ability to apply focused ultrasound to the brain in a safe and efficacious manner, future work should seek to reveal any such differences, which may significantly alter the established parameters for ultrasound-induced BBB disruption.

MRI has proven to be a useful tool to guide the focal BBB disruption to a desired location, to verify the status of the BBB disruption by the penetration or exclusion of MR contrast agents in the brain, and to monitor the impact of the treatment on tumor growth. The relationship between MRI signal enhancement and applied pressure amplitudes demonstrated in Chapter 3 and that of MRI signal enhancement and DOX concentration in brain tissue demonstrated in Chapter 4 indicate that MRI has the potential to provide useful feedback on the extent of ultrasound-induced BBB disruption, the resultant drug penetration in the brain, and the eventual restoration of the BBB. MRI has also been demonstrated to provide noninvasive image characterization of cerebral blood flow, cerebral blood volume, and vascular permeability (254-263) and could perhaps be further exploited to provide information on the time-variant neurovascular permeability induced by ultrasound. Most current MRI-based models of BBB breakdown are based on an assumption of constant neurovascular permeability, as is the case in chronic neurological diseases such as multiple sclerosis and tumors (258). Since the BBB opening induced by ultrasound is a transient effect that reverses with time (13), the assumption of constant neurovascular permeability is not valid for our application. To improve these models and their practical use for patient treatment, the vascular permeability of the sonicated location could be quantified by MRI over the time course of the induced focal BBB disruption (4-6 hours) to obtain information that could be useful in determining the ideal window for drug delivery. These data could then be used to develop more sophisticated models of BBB permeability which take into account the time-variant nature of the opening of the BBB induced by focused ultrasound.

Finally, the preliminary fluorescence imaging results present in Chapter 4 offer interesting findings on the likely cellular colocalization of DOX in the brain after ultrasound-enhanced chemotherapy but are not conclusive. To better understand the biophysics of the ultrasound-induced BBB disruption, longitudinal fluorescence imaging studies could be used to shed light on the distribution (intracellular versus extracellular, neuronal versus glial) of an agent over time following ultrasound-mediated delivery. Fluorescence markers could also be used to track cellular activity and distribution. Microglia, the macrophages of the brain, have been identified as the first responders to CNS injury (264-266). They release and respond to several cytokines as well as neurotoxic substances, including nitric oxide (267), which itself has been implicated in modulation of microvascular permeability (47, 268). Thus, it is likely that microglia play an active role in the physiological response of the brain to focal stimulation with microbubble-enhanced ultrasound, leading to localized and transient disruption of the blood-brain barrier. Because microglia perform a vast number of immune-related roles (269), it is also likely that they would act as the primary players in mounting the brain's immune response to the entry of exogenous agents into the brain parenchyma following ultrasound-induced BBB disruption and thus reduce the potency of therapeutic agents. Therefore, a better understanding of the behavior of microglia in response to ultrasound-mediated CNS drug delivery may help in the development of more effective techniques for targeted drug delivery to the brain.

7 References

1. DeAngelis LM. Brain tumors. *N Engl J Med* 2001;344:114-23.
2. Kroll RA, Neuwelt EA. Outwitting the blood-brain barrier for therapeutic purposes: osmotic opening and other means. 1998;42:1083-99.
3. Pardridge WM. Targeting neurotherapeutic agents through the blood-brain barrier. *Arch Neurol* 2002;59:35-40.
4. Banerjee S, Bhat MA. Neuron-glial interactions in blood-brain barrier formation. *Annu Rev Neurosci* 2007;30:235-58.
5. von Holst H, Knochenhauer E, Blomgren H, *et al.* Uptake of adriamycin in tumour and surrounding brain tissue in patients with malignant gliomas. *Acta Neurochir (Wien)* 1990;104:13-6.
6. Fukumura D, Jain RK. Tumor microenvironment abnormalities: causes, consequences, and strategies to normalize. *J Cell Biochem* 2007;101:937-49.
7. Hochberg FH, Pruitt A. Assumptions in the radiotherapy of glioblastoma. *Neurology* 1980;30:907-11.
8. Wallner KE, Galicich JH, Krol G, Arbit E, Malkin MG. Patterns of failure following treatment for glioblastoma multiforme and anaplastic astrocytoma. *Int J Radiat Oncol Biol Phys* 1989;16:1405-9.
9. Walker MD, Alexander E, Jr., Hunt WE, *et al.* Evaluation of BCNU and/or radiotherapy in the treatment of anaplastic gliomas. A cooperative clinical trial. *J Neurosurg* 1978;49:333-43.
10. Pardridge WM. Drug and gene delivery to the brain: the vascular route. *Neuron* 2002;36:555-8.
11. Bobo RH, Laske DW, Akbasak A, Morrison PF, Dedrick RL, Oldfield EH. Convection-enhanced delivery of macromolecules in the brain. *Proc Natl Acad Sci U S A* 1994;91:2076-80.
12. Westphal M, Hilt DC, Bortey E, *et al.* A phase 3 trial of local chemotherapy with biodegradable carmustine (BCNU) wafers (Gliadel wafers) in patients with primary malignant glioma. *Neuro Oncol* 2003;5:79-88.
13. Hynynen K, McDannold N, Vykhodtseva N, Jolesz FA. Noninvasive MR imaging-guided focal opening of the blood-brain barrier in rabbits. *Radiology* 2001;220:640-6.
14. Sheikov N, McDannold N, Vykhodtseva N, Jolesz F, Hynynen K. Cellular mechanisms of the blood-brain barrier opening induced by ultrasound in presence of microbubbles. *Ultrasound Med Biol* 2004;30:979-89.
15. Sheikov N, McDannold N, Sharma S, Hynynen K. Effect of Focused Ultrasound Applied With an Ultrasound Contrast Agent on the Tight Junctional Integrity of the Brain Microvascular Endothelium. *Ultrasound Med Biol* 2008.
16. Kinoshita M, McDannold N, Jolesz FA, Hynynen K. Noninvasive localized delivery of Herceptin to the mouse brain by MRI-guided focused ultrasound-induced blood-brain barrier disruption. *Proc Natl Acad Sci U S A* 2006;103:11719-23.

17. Treat LH, McDannold N, Vykhodtseva N, Zhang Y, Tam K, Hynynen K. Targeted delivery of doxorubicin to the rat brain at therapeutic levels using MRI-guided focused ultrasound. *Int J Cancer* 2007;121:901-7.
18. Choi JJ, Pernot M, Small SA, Konofagou EE. Noninvasive, transcranial and localized opening of the blood-brain barrier using focused ultrasound in mice. *Ultrasound Med Biol* 2007;33:95-104.
19. Raymond SB, Skoch J, Hynynen K, Bacskai BJ. Multiphoton imaging of ultrasound/Optison mediated cerebrovascular effects in vivo. *J Cereb Blood Flow Metab* 2006.
20. Raymond SB, Treat LH, Dewey JD, McDannold NJ, Hynynen K, Bacskai BJ. Ultrasound enhanced delivery of molecular imaging and therapeutic agents in Alzheimer's disease mouse models. *PLoS ONE* 2008;3:e2175
doi:10.1371/journal.pone.0002175.
21. Kinoshita M, McDannold N, Jolesz FA, Hynynen K. Targeted delivery of antibodies through the blood-brain barrier by MRI-guided focused ultrasound. *Biochem Biophys Res Commun* 2006;340:1085-90.
22. Abbott NJ, Romero IA. Transporting therapeutics across the blood-brain barrier. *1996*;2:106-13.
23. Wells WA, Bonetta L. Endothelial tight junctions form the blood-brain barrier. *J Cell Biol* 2005;169:378.
24. Vein AA. Science and fate: Lina Stern (1878-1968), a neurophysiologist and biochemist. *J Hist Neurosci* 2008;17:195-206.
25. Reese TS, Karnovsky MJ. Fine structural localization of a blood-brain barrier to exogenous peroxidase. *1967*;34:207-17.
26. Strazielle N, Khuth ST, Gherzi-Egea JF. Detoxification systems, passive and specific transport for drugs at the blood-CSF barrier in normal and pathological situations. *Adv Drug Deliv Rev* 2004;56:1717-40.
27. Chi C, Carlson SD. The perineurium of the adult housefly: ultrastructure and permeability to lanthanum. *Cell Tissue Res* 1981;217:373-86.
28. Pardridge WM. Brain drug targeting and gene technologies. *Jpn J Pharmacol* 2001;87:97-103.
29. Risau W, Wolburg H. Development of the blood-brain barrier. *Trends Neurosci* 1990;13:174-8.
30. Martin-Padura I, Lostaglio S, Schneemann M, *et al.* Junctional adhesion molecule, a novel member of the immunoglobulin superfamily that distributes at intercellular junctions and modulates monocyte transmigration. *J Cell Biol* 1998;142:117-27.
31. Furuse M, Hirase T, Itoh M, Nagafuchi A, Yonemura S, Tsukita S. Occludin: a novel integral membrane protein localizing at tight junctions. *J Cell Biol* 1993;123:1777-88.
32. Morita K, Furuse M, Fujimoto K, Tsukita S. Claudin multigene family encoding four-transmembrane domain protein components of tight junction strands. *Proc Natl Acad Sci U S A* 1999;96:511-6.
33. Butt AM, Jones HC, Abbott NJ. Electrical resistance across the blood-brain barrier in anaesthetized rats: a developmental study. *J Physiol* 1990;429:47-62.

34. Misra A, Ganesh S, Shahiwala A, Shah SP. Drug delivery to the central nervous system: a review. *J Pharm Pharm Sci* 2003;6:252-73.
35. Minn A, Gherzi-Egea JF, Perrin R, Leininger B, Siest G. Drug metabolizing enzymes in the brain and cerebral microvessels. *Brain Res Brain Res Rev* 1991;16:65-82.
36. Witt KA, Gillespie TJ, Huber JD, Eggleton RD, Davis TP. Peptide drug modifications to enhance bioavailability and blood-brain barrier permeability. *Peptides* 2001;22:2329-43.
37. Fricker G, Miller DS. Modulation of drug transporters at the blood-brain barrier. *Pharmacology* 2004;70:169-76.
38. Juliano RL, Ling V. A surface glycoprotein modulating drug permeability in Chinese hamster ovary cell mutants. *Biochim Biophys Acta* 1976;455:152-62.
39. Seymour L, Bezwoda WR, Dansey RD. P-glycoprotein immunostaining correlates with ER and with high Ki67 expression but fails to predict anthracycline resistance in patients with advanced breast cancer. *Breast Cancer Res Treat* 1995;36:61-9.
40. Siegal T, Zylber-Katz E. Strategies for increasing drug delivery to the brain: focus on brain lymphoma. *Clin Pharmacokinet* 2002;41:171-86.
41. Hall WA, Doolittle ND, Daman M, *et al.* Osmotic blood-brain barrier disruption chemotherapy for diffuse pontine gliomas. *J Neurooncol* 2006;77:279-84.
42. Doolittle ND, Miner ME, Hall WA, *et al.* Safety and efficacy of a multicenter study using intraarterial chemotherapy in conjunction with osmotic opening of the blood-brain barrier for the treatment of patients with malignant brain tumors. 2000;88:637-47.
43. Neuwelt EA, Barnett PA, McCormick CI, Frenkel EP, Minna JD. Osmotic blood-brain barrier modification: monoclonal antibody, albumin, and methotrexate delivery to cerebrospinal fluid and brain. *Neurosurgery* 1985;17:419-23.
44. Kemper EM, Boogerd W, Thuis I, Beijnen JH, van Tellingen O. Modulation of the blood-brain barrier in oncology: therapeutic opportunities for the treatment of brain tumours? *Cancer Treat Rev* 2004;30:415-23.
45. Haluska M, Anthony ML. Osmotic blood-brain barrier modification for the treatment of malignant brain tumors. *Clin J Oncol Nurs* 2004;8:263-7.
46. Nadal A, Fuentes E, Pastor J, McNaughton PA. Plasma albumin is a potent trigger of calcium signals and DNA synthesis in astrocytes. *Proc Natl Acad Sci U S A* 1995;92:1426-30.
47. Mayhan WG. Nitric oxide donor-induced increase in permeability of the blood-brain barrier. *Brain Res* 2000;866:101-8.
48. Nakano S, Matsukado K, Black KL. Increased brain tumor microvessel permeability after intracarotid bradykinin infusion is mediated by nitric oxide. *Cancer Res* 1996;56:4027-31.
49. Chio CC, Baba T, Black KL. Selective blood-tumor barrier disruption by leukotrienes. *J Neurosurg* 1992;77:407-10.
50. Black KL, Baba T, Pardridge WM. Enzymatic barrier protects brain capillaries from leukotriene C4. *J Neurosurg* 1994;81:745-51.
51. Emerich DF, Dean RL, Osborn C, Bartus RT. The development of the bradykinin agonist labradimil as a means to increase the permeability of the blood-brain barrier: from concept to clinical evaluation. *Clin Pharmacokinet* 2001;40:105-23.

52. Matsukado K, Inamura T, Nakano S, Fukui M, Bartus RT, Black KL. Enhanced tumor uptake of carboplatin and survival in glioma-bearing rats by intracarotid infusion of bradykinin analog, RMP-7. *Neurosurgery* 1996;39:125-33; discussion 33-4.
53. Miller G. Drug targeting. Breaking down barriers. *Science* 2002;297:1116-8.
54. Grondin R, Zhang Z, Ai Y, Gash DM, Gerhardt GA. Intracranial delivery of proteins and peptides as a therapy for neurodegenerative diseases. *Prog Drug Res* 2003;61:101-23.
55. Mardor Y, Rahav O, Zauberman Y, *et al.* Convection-enhanced drug delivery: increased efficacy and magnetic resonance image monitoring. *Cancer Res* 2005;65:6858-63.
56. Ferguson S, Lesniak MS. Convection enhanced drug delivery of novel therapeutic agents to malignant brain tumors. *Curr Drug Deliv* 2007;4:169-80.
57. Lieberman DM, Laske DW, Morrison PF, Bankiewicz KS, Oldfield EH. Convection-enhanced distribution of large molecules in gray matter during interstitial drug infusion. *J Neurosurg* 1995;82:1021-9.
58. Kroll RA, Pagel MA, Muldoon LL, Roman-Goldstein S, Neuwelt EA. Increasing volume of distribution to the brain with interstitial infusion: dose, rather than convection, might be the most important factor. *Neurosurgery* 1996;38:746-52; discussion 52-4.
59. Saito R, Bringas JR, McKnight TR, *et al.* Distribution of liposomes into brain and rat brain tumor models by convection-enhanced delivery monitored with magnetic resonance imaging. *Cancer Res* 2004;64:2572-9.
60. Kawakami M, Kawakami K, Puri RK. Interleukin-4-Pseudomonas exotoxin chimeric fusion protein for malignant glioma therapy. *J Neurooncol* 2003;65:15-25.
61. Lidar Z, Mardor Y, Jonas T, *et al.* Convection-enhanced delivery of paclitaxel for the treatment of recurrent malignant glioma: a phase I/II clinical study. *J Neurosurg* 2004;100:472-9.
62. Sampson JH, Akabani G, Archer GE, *et al.* Progress report of a Phase I study of the intracerebral microinfusion of a recombinant chimeric protein composed of transforming growth factor (TGF)-alpha and a mutated form of the Pseudomonas exotoxin termed PE-38 (TP-38) for the treatment of malignant brain tumors. *J Neurooncol* 2003;65:27-35.
63. Voges J, Reszka R, Gossmann A, *et al.* Imaging-guided convection-enhanced delivery and gene therapy of glioblastoma. *Ann Neurol* 2003;54:479-87.
64. Salvatore MF, Ai Y, Fischer B, *et al.* Point source concentration of GDNF may explain failure of phase II clinical trial. *Exp Neurol* 2006;202:497-505.
65. Ai Y, Markesbery W, Zhang Z, *et al.* Intraputamenal infusion of GDNF in aged rhesus monkeys: distribution and dopaminergic effects. *J Comp Neurol* 2003;461:250-61.
66. Huwyler J, Drewe J, Gutmann H, Thole M, Fricker G. Modulation of morphine-6-glucuronide penetration into the brain by P-glycoprotein. *Int J Clin Pharmacol Ther* 1998;36:69-70.
67. Huwyler J, Wu D, Pardridge WM. Brain drug delivery of small molecules using immunoliposomes. *Proc Natl Acad Sci U S A* 1996;93:14164-9.
68. Lee HJ, Pardridge WM. Pharmacokinetics and delivery of tat and tat-protein conjugates to tissues in vivo. *Bioconj Chem* 2001;12:995-9.
69. Bickel U, Yoshikawa T, Pardridge WM. Delivery of peptides and proteins through the blood-brain barrier. *Adv Drug Deliv Rev* 2001;46:247-79.

70. Pardridge WM. Non-invasive drug delivery to the human brain using endogenous blood-brain barrier transport systems. *Pharm Sci Technol Today* 1999;2:49-59.
71. Pardridge WM, Kang YS, Buciak JL. Transport of human recombinant brain-derived neurotrophic factor (BDNF) through the rat blood-brain barrier in vivo using vector-mediated peptide drug delivery. *Pharm Res* 1994;11:738-46.
72. Pardridge WM. Molecular Trojan horses for blood-brain barrier drug delivery. *Curr Opin Pharmacol* 2006;6:494-500.
73. Pardridge WM. Drug and gene targeting to the brain with molecular Trojan horses. *Nat Rev Drug Discov* 2002;1:131-9.
74. Dietz GP, Bahr M. Delivery of bioactive molecules into the cell: the Trojan horse approach. *Mol Cell Neurosci* 2004;27:85-131.
75. Penas-Prado M, Gilbert MR. Molecularly targeted therapies for malignant gliomas: advances and challenges. *Expert Rev Anticancer Ther* 2007;7:641-61.
76. Kreuter J. Nanoparticulate systems for brain delivery of drugs. *Adv Drug Deliv Rev* 2001;47:65-81.
77. Gulyaev AE, Gelperina SE, Skidan IN, Antropov AS, Kivman GY, Kreuter J. Significant transport of doxorubicin into the brain with polysorbate 80-coated nanoparticles. *Pharm Res* 1999;16:1564-9.
78. Fattal E, Vauthier C, Aynie I, *et al.* Biodegradable polyalkylcyanoacrylate nanoparticles for the delivery of oligonucleotides. *J Control Release* 1998;53:137-43.
79. Stolnik S, Dunn SE, Garnett MC, *et al.* Surface modification of poly(lactide-co-glycolide) nanospheres by biodegradable poly(lactide)-poly(ethylene glycol) copolymers. *Pharm Res* 1994;11:1800-8.
80. Gref R, Minamitake Y, Peracchia MT, Trubetskoy V, Torchilin V, Langer R. Biodegradable long-circulating polymeric nanospheres. *Science* 1994;263:1600-3.
81. Amrite AC, Kompella UB. Size-dependent disposition of nanoparticles and microparticles following subconjunctival administration. *J Pharm Pharmacol* 2005;57:1555-63.
82. Reddy LH, Sharma RK, Murthy RS. Enhanced tumour uptake of doxorubicin loaded poly(butyl cyanoacrylate) nanoparticles in mice bearing Dalton's lymphoma tumour. *J Drug Target* 2004;12:443-51.
83. Calvo P, Gouritin B, Chacun H, *et al.* Long-circulating PEGylated polycyanoacrylate nanoparticles as new drug carrier for brain delivery. *Pharm Res* 2001;18:1157-66.
84. Steiniger SC, Kreuter J, Khalansky AS, *et al.* Chemotherapy of glioblastoma in rats using doxorubicin-loaded nanoparticles. *Int J Cancer* 2004;109:759-67.
85. Kabanov AV, Batrakova EV. New technologies for drug delivery across the blood brain barrier. *Curr Pharm Des* 2004;10:1355-63.
86. Batrakova EV, Li S, Li Y, Alakhov VY, Kabanov AV. Effect of pluronic P85 on ATPase activity of drug efflux transporters. *Pharm Res* 2004;21:2226-33.
87. Batrakova EV, Zhang Y, Li Y, *et al.* Effects of pluronic P85 on GLUT1 and MCT1 transporters in the blood-brain barrier. *Pharm Res* 2004;21:1993-2000.
88. Miller DW, Batrakova EV, Kabanov AV. Inhibition of multidrug resistance-associated protein (MRP) functional activity with pluronic block copolymers. *Pharm Res* 1999;16:396-401.

89. Batrakova EV, Miller DW, Li S, Alakhov VY, Kabanov AV, Elmquist WF. Pluronic P85 enhances the delivery of digoxin to the brain: in vitro and in vivo studies. *J Pharmacol Exp Ther* 2001;296:551-7.
90. Newcomb R, Abbruscato TJ, Singh T, Nadasdi L, Davis TP, Miljanich G. Bioavailability of Ziconotide in brain: influx from blood, stability, and diffusion. *Peptides* 2000;21:491-501.
91. Krewson CE, Klarman ML, Saltzman WM. Distribution of nerve growth factor following direct delivery to brain interstitium. *Brain Res* 1995;680:196-206.
92. Walter KA, Tamargo RJ, Olivi A, Burger PC, Brem H. Intratumoral chemotherapy. *Neurosurgery* 1995;37:1128-45.
93. Hamstra DA, Moffat BA, Hall DE, *et al.* Intratumoral injection of BCNU in ethanol (DTI-015) results in enhanced delivery to tumor--a pharmacokinetic study. *J Neurooncol* 2005;73:225-38.
94. Fung LK, Ewend MG, Sills A, *et al.* Pharmacokinetics of interstitial delivery of carmustine, 4-hydroperoxycyclophosphamide, and paclitaxel from a biodegradable polymer implant in the monkey brain. *Cancer Res* 1998;58:672-84.
95. Brem H, Gabikian P. Biodegradable polymer implants to treat brain tumors. *J Control Release* 2001;74:63-7.
96. Benoit JP, Faisant N, Venier-Julienne MC, Menei P. Development of microspheres for neurological disorders: from basics to clinical applications. *J Control Release* 2000;65:285-96.
97. Westphal M, Ram Z, Riddle V, Hilt D, Bortey E. Gliadel wafer in initial surgery for malignant glioma: long-term follow-up of a multicenter controlled trial. *Acta Neurochir (Wien)* 2006;148:269-75; discussion 75.
98. Hynynen K. Ultrasound for drug and gene delivery to the brain. *Adv Drug Deliv Rev* 2008;60:1209-17.
99. Vykhodtseva N, McDannold N, Hynynen K. Progress and problems in the application of focused ultrasound for blood-brain barrier disruption. *Ultrasonics* 2008;48:279-96.
100. Hynynen K. Focused ultrasound for blood-brain disruption and delivery of therapeutic molecules into the brain. *Expert Opin Drug Deliv* 2007;4:27-35.
101. Hynynen K, Clement G. Clinical applications of focused ultrasound-the brain. *Int J Hyperthermia* 2007;23:193-202.
102. Clement GT, Hynynen K. A non-invasive method for focusing ultrasound through the human skull. *Phys Med Biol* 2002;47:1219-36.
103. Clement GT, Sun J, Giesecke T, Hynynen K. A hemisphere array for non-invasive ultrasound brain therapy and surgery. *Phys Med Biol* 2000;45:3707-19.
104. Hynynen K, Lulu BA. Hyperthermia in cancer treatment. *InvestRadiol* 1990;25:824-34.
105. Hynynen K. Biophysics and technology of ultrasound hyperthermia. In: Gautherie M, editor. *Methods of External Hyperthermic Heating*. New York: Springer-Verlag; 1990. p. 61-115.
106. Duck FA, Baker AC, Starritt HC. *Ultrasound in medicine*. Bristol ; Philadelphia, Pa.: Institute of Physics Pub.; 1998.
107. Leighton TG. *The Acoustic Bubble*. San Diego, CA: Academic Press Limited; 1994.

108. Fry FJ, Johnson LK. Tumor irradiation with intense ultrasound. *Ultrasound Med Biol* 1978;4:337-41.
109. Algan O, Fosmire H, Hynynen K, *et al.* External beam radiotherapy and hyperthermia in the treatment of patients with locally advanced prostate carcinoma. *Cancer* 2000;89:399-403.
110. Beerlage HP, Thuroff S, Debruyne FM, Chaussy C, de la Rosette JJ. Transrectal high-intensity focused ultrasound using the Ablatherm device in the treatment of localized prostate carcinoma. 1999;54:273-7.
111. Chaussy C, Thuroff S. High-intensity focused ultrasound in prostate cancer: results after 3 years. 2000;4:179-82.
112. Diederich CJ, Stafford RJ, Nau WH, Burdette EC, Price RE, Hazle JD. Transurethral ultrasound applicators with directional heating patterns for prostate thermal therapy: in vivo evaluation using magnetic resonance thermometry. 2004;31:405-13.
113. Hegarty NJ, Fitzpatrick JM. High intensity focused ultrasound in benign prostatic hyperplasia. *EurJUltrasound* 1999;9:55-60.
114. Fennessy FM, Tempany CM, McDannold NJ, *et al.* Uterine leiomyomas: MR imaging-guided focused ultrasound surgery--results of different treatment protocols. *Radiology* 2007;243:885-93.
115. Jolesz FA, Hynynen K, McDannold N, Tempany C. MR imaging-controlled focused ultrasound ablation: a noninvasive image-guided surgery. *Magn Reson Imaging Clin N Am* 2005;13:545-60.
116. McDannold N, Tempany CM, Fennessy FM, *et al.* Uterine leiomyomas: MR imaging-based thermometry and thermal dosimetry during focused ultrasound thermal ablation. *Radiology* 2006;240:263-72.
117. Stewart EA, Gedroyc WMH, Tempany CMC, *et al.* Focused ultrasound treatment of uterine fibroids: safety and feasibility of a noninvasive thermoablative technique. *AmJObstetGynecol* 2003;189:48-54.
118. Tempany CM, Stewart EA, McDannold N, Quade BJ, Jolesz FA, Hynynen K. MR imaging-guided focused ultrasound surgery of uterine leiomyomas: a feasibility study. *Radiology* 2003;226:897-905.
119. Vaezy S, Fujimoto VY, Walker C, Martin RW, Chi EY, Crum LA. Treatment of uterine fibroid tumors in a nude mouse model using high-intensity focused ultrasound. *AmJObstetGynecol* 2000;183:6-11.
120. Malcolm AL, ter Haar GR. Ablation of tissue volumes using high intensity focused ultrasound. *UltrasoundMedBiol J1 - UMB* 1996;22:659-69.
121. ter Haar GR. High intensity focused ultrasound for the treatment of tumors. *Echocardiography* 2001;18:317-22.
122. Vaezy S, Martin R, Crum L. High intensity focused ultrasound: a method of hemostasis. *Echocardiography* 2001;18:309-15.
123. Brentnall MD, Martin RW, Vaezy S, Kaczowski P, Forster F, Crum L. A new high intensity focused ultrasound applicator for surgical applications. 2001;48:53-63.
124. Diehl KA, Crawford E, Shinko PD, Tallman RD, Jr., Oglesbee MJ. Alterations in hemostasis associated with hyperthermia in a canine model. 2000;64:262-70.
125. Vaezy S, Martin R, Schmiedl U, *et al.* Liver hemostasis using high-intensity focused ultrasound. *Ultrasound Med Biol* 1997;23:1413-20.

126. Delon-Martin C, Vogt C, Chignier E, Guers C, Chapelon JY, Cathignol D. Venous thrombosis generation by means of high-intensity focused ultrasound. *Ultrasound Med Biol* 1995;21:113-9.
127. Rivens IH, Rowland IJ, Denbow M, Fisk NM, ter Haar GR, Leach MO. Vascular occlusion using focused ultrasound surgery for use in fetal medicine. *EurJUltrasound* 1999;9:89-97.
128. Hynynen K, Colucci V, Chung A, Jolesz F. Noninvasive arterial occlusion using MRI-guided focused ultrasound. *Ultrasound Med Biol* 1996;22:1071-7.
129. Francis CW. Ultrasound-enhanced thrombolysis. *Echocardiography* 2001;18:239-46.
130. Harpaz D, Chen X, Francis CW, Marder VJ, Meltzer RS. Ultrasound enhancement of thrombolysis and reperfusion in vitro. 1993;21:1507-11.
131. Riggs PN, Francis CW, Bartos SR, Penney DP. Ultrasound enhancement of rabbit femoral artery thrombolysis. *Cardiovasc Surg* 1997;5:201-7.
132. Suchkova V, Carstensen EL, Francis CW. Ultrasound enhancement of fibrinolysis at frequencies of 27 to 100 kHz. 2002;28:377-82.
133. Wu Y, Unger EC, McCreery TP, *et al.* Binding and lysing of blood clots using MRX-408. *InvestRadiol* 1998;33:880-5.
134. Porter TR, LeVeen RF, Fox R, Kricsfeld A, Xie F. Thrombolytic enhancement with perfluorocarbon-exposed sonicated dextrose albumin microbubbles. *AmHeart J* 1996;132:964-8.
135. Patrick JT, Nolting MN, Goss SA, *et al.* Ultrasound and the blood-brain barrier. *Adv Exp Med Biol* 1990;267:369-81.
136. Kim HJ, Greenleaf JF, Kinnick RR, Bronk JT, Bolander ME. Ultrasound-mediated transfection of mammalian cells. *HumGene Ther* 1996;7:1339-46.
137. Greenleaf WJ, Bolander ME, Sarkar G, Goldring MB, Greenleaf JF. Artificial cavitation nuclei significantly enhance acoustically induced cell transfection. *UltrasoundMedBiol J1 - UMB* 1998;24:587-95.
138. Unger EC, McCreery TP, Sweitzer RH. Ultrasound enhances gene expression of liposomal transfection. *InvestRadiol* 1997;32:723-7.
139. Silcox CE, Smith RC, King R, *et al.* MRI-guided ultrasonic heating allows spatial control of exogenous luciferase in canine prostate. *Ultrasound Med Biol* 2005;31:965-70.
140. Raymond SB, Treat LH, Dewey JD, McDannold NJ, Hynynen K, Bacskaï BJ. Ultrasound enhanced delivery of molecular imaging and therapeutic agents in Alzheimer's disease mouse models. *PLoS ONE* 2008;3:e2175.
141. Wood RW, Loomis AL. The physical and biological effects of high frequency sound waves of greater intensity. *The London, Edinburgh, and Dublin Philosophical Magazine and Journal of Science* 1927;4:417-36.
142. Lynn JG, Putnam TJ. Histology of cerebral lesions produced by focused ultrasound. *Am J Path* 1944;20:637-52.
143. Lynn JG, Zwemer RL, Chick AJ, Miller AE. A new method for the generation and use of focused ultrasound in experimental biology. *J Gen Physiol* 1942;26:179-93.
144. Barnard JW, Fry WJ, Fry FJ, Brennan JF. Small localized ultrasonic lesions in the white and gray matter of the cat brain. *Arch Neurol Psychiatry* 1956;75:15-35.
145. Barnard JW, Fry WJ, Fry FJ, Krumins RF. Effects of high intensity ultrasound on the central nervous system of the cat. *J Comp Neurol* 1955;103:459-84.

146. Fry WJ, Barnard JW, Fry FJ. Ultrasonically produced localized selective lesions in the central nervous system. *AmJPhysMed* 1955;34:413-23.
147. Fry WJ, Barnard JW, Fry FJ, Krumins RF, Brennan JF. Ultrasonic lesions in the mammalian central nervous system. *Science* 1955;122:517-8.
148. Fry WJ, Mosberg W, Barnard JW, Fry FJ. Production of focal destructive lesions in the central nervous system with ultrasound. *Journal of Neurosurgery* 1954;11:471-8.
149. Wall PD, Fry WJ, Stephens R, Tucker D, Lettvin JY. Changes produced in the central nervous system by ultrasound. *Science* 1951;114:686-7.
150. Lele PP. Effects of ultrasound on "solid" mammalian tissues and tumors in vivo. In: Repacholi MH, Grondolfo M, Rindi A, editors. *Ultrasound: Medical Applications, Biological Effects and Hazard Potential*. New York: Plenum Pub. Corp.; 1987. p. 275-306.
151. Lele PP. Thresholds and mechanisms of ultrasonic damage to "organized" animal tissues. In: Hazzard DG, Litz ML, editors. *Symposium on biological effects and characterizations of ultrasound sources: DHEW Publ. FDA 78-8048*; 1977. p. 224-39.
152. Lele PP. Production of deep focal lesions by focused ultrasound--current status. *1967*;5:105-12.
153. Lele PP. A simple method for production of trackless focal lesions with focused ultrasound: physical factors. *J Physiol* 1962;160:494-512.
154. Robinson TC, Lele PP. An analysis of lesion development in the brain and in plastics by high- intensity focused ultrasound at low-megahertz frequencies. *JAcoustSocAm J1 - JASA* 1972;51:1333-51.
155. Bakay L, Ballantine HT, Jr., Hueter TF, Sosa D. Ultrasonically produced changes in the blood-brain barrier. *AMA Arch Neurol Psychiatry* 1956;76:457-67.
156. Haude W. [Influence of ultrasonics on permeability of blood-brain barrier.]. *Acta Biol Med Ger* 1959;2:185-95.
157. Ballantine HT, Bell E, Manlapaz J. Progress and problems in the neurological applications of focused ultrasound. *J Neurosurg* 1960;17:858-76.
158. Diederich CJ, Hynynen K. Induction of hyperthermia using an intracavitary multielement ultrasonic applicator. *IEEE Trans Biomed Eng* 1989;36:432-8.
159. Ebbini ES, Cain CA. A spherical-section ultrasound phased array applicator for deep localized hyperthermia. *IEEE TransBiomedEng* 1991;38:634-43.
160. Diederich CJ, Hynynen K. Ultrasound technology for hyperthermia. *Ultrasound Med Biol* 1999;25:871-87.
161. Hynynen K, Watmough DJ, Mallard JR, Fuller M. Local hyperthermia induced by focussed and overlapping ultrasonic fields--an in vivo demonstration. *Ultrasound Med Biol* 1983;9:621-7.
162. Hynynen K, Watmough DJ, Mallard JR. Design of ultrasonic transducers for local hyperthermia. *Ultrasound Med Biol* 1981;7:397-402.
163. Dunn F, Lohnes JE, Fry FJ. Frequency dependence of threshold ultrasonic dosages for irreversible structural changes in mammalian brain. *JAcoustSocAm J1 - JASA* 1975;58:512-4.
164. Fry WJ, Fry FJ. Fundamental neurological research and human neurosurgery using intense ultrasound. *IRE Trans Med Electron* 1960;ME-7:166-81.
165. Fry FJ, Kossoff G, Eggleton RC, Dunn F. Threshold ultrasonic dosages for structural changes in the mammalian brain. *JAcoustSocAm J1 - JASA* 1970;48:1413-7.

166. Heimburger RF. Ultrasound augmentation of central nervous system tumor therapy. *Indiana Med* 1985;78:469-76.
167. Fry FJ, Goss SA, Patrick JT. Transkull focal lesions in cat brain produced by ultrasound. *J Neurosurg* 1981;54:659-63.
168. Fry FJ, Goss SA. Further studies of the transkull transmission of an intense focused ultrasonic beam: lesion production at 500 kHz. *Ultrasound Med Biol* 1980;6:33-8.
169. Fry FJ. Transkull transmission of an intense focused ultrasonic beam. *Ultrasound Med Biol* 1977;3:179-84.
170. Hynynen K, Jolesz FA. Demonstration of potential noninvasive ultrasound brain therapy through an intact skull. *Ultrasound Med Biol* 1998;24:275-83.
171. Sun J, Hynynen K. Focusing of therapeutic ultrasound through a human skull: a numerical study. *J Acoust Soc Am* 1998;104:1705-15.
172. Sun J, Hynynen K. The potential of transskull ultrasound therapy and surgery using the maximum available skull surface area. *J Acoust Soc Am* 1999;105:2519-27.
173. Aubry JF, Tanter M, Pernot M, Thomas JL, Fink M. Experimental demonstration of noninvasive transskull adaptive focusing based on prior computed tomography scans. *J Acoust Soc Am* 2003;113:84-93.
174. Hynynen K, Clement GT, McDannold N, *et al.* 500-element ultrasound phased array system for noninvasive focal surgery of the brain: a preliminary rabbit study with ex vivo human skulls. *Magn Reson Med* 2004;52:100-7.
175. Hynynen K, McDannold N, Clement G, *et al.* Pre-clinical testing of a phased array ultrasound system for MRI-guided noninvasive surgery of the brain-A primate study. *Eur J Radiol* 2006;59:149-56.
176. Yin X, Hynynen K. A numerical study of transcranial focused ultrasound beam propagation at low frequency. *Phys Med Biol* 2005;50:1821-36.
177. Clement GT, White PJ, Hynynen K. Enhanced ultrasound transmission through the human skull using shear mode conversion. *J Acoust Soc Am* 2004;115:1356-64.
178. White PJ, Clement GT, Hynynen K. Longitudinal and shear mode ultrasound propagation in human skull bone. *Ultrasound Med Biol* 2006;32:1085-96.
179. Fry FJ, Sanghvi NT, Morris RF, *et al.* A focused ultrasound system for tissue volume ablation in deep seated brain sites. *Proceedings of the IEEE Ultrasonics Symposium*; 1986; 1986. p. 1001.
180. Hynynen K, Darkazanli A, Unger E, Schenck JF. MRI-guided noninvasive ultrasound surgery. *Med Phys* 1993;20:107-15.
181. Hynynen K, Vykhodtseva NI, Chung AH, Sorrentino V, Colucci V, Jolesz FA. Thermal effects of focused ultrasound on the brain: determination with MR imaging. *Radiology* 1997;204:247-53.
182. Darkazanli A, Hynynen K, Unger EC, Schenck JF. On-line monitoring of ultrasonic surgery with MR imaging. *J Magn Reson Imaging* 1993;3:509-14.
183. Cline HE, Schenck JF, Hynynen K, Watkins RD, Souza SP, Jolesz FA. MR-guided focused ultrasound surgery. *J Comput Assist Tomogr* 1992;16:956-65.
184. Cline HE, Hynynen K, Watkins RD, *et al.* Focused US system for MR imaging-guided tumor ablation. *Radiology* 1995;194:731-7.
185. Cline HE, Hynynen K, Hardy CJ, Watkins RD, Schenck JF, Jolesz FA. MR temperature mapping of focused ultrasound surgery. *Magn Reson Med* 1994;31:628-36.

186. Chung AH, Hynynen K, Colucci V, Oshio K, Cline HE, Jolesz FA. Optimization of spoiled gradient-echo phase imaging for in vivo localization of a focused ultrasound beam. *MagnResonMed* 1996;36:745-52.
187. McDannold N, King RL, Jolesz FA, Hynynen K. The use of quantitative temperature images to predict the optimal power for focused ultrasound surgery: in vivo verification in rabbit muscle and brain. *Med Phys* 2002;29:356-65.
188. Ishihara Y, Calderon A, Watanabe H, Okamoto K, Suzuki Y, Kuroda K. A precise and fast temperature mapping using water proton chemical shift. *MagnResonMed* 1995;34:814-23.
189. FDA Approves New Device to Treat Uterine Fibroids. October 22, 2004 [cited; October 22, 2004:[Available from: <http://www.fda.gov/bbs/topics/ANSWERS/2004/ANS01319.html>
190. McDannold N, Vykhodtseva N, Jolesz FA, Hynynen K. MRI investigation of the threshold for thermally induced blood-brain barrier disruption and brain tissue damage in the rabbit brain. *Magn Reson Med* 2004;51:913-23.
191. Vykhodtseva NI, Hynynen K, Damianou C. Histologic effects of high intensity pulsed ultrasound exposure with subharmonic emission in rabbit brain in vivo. *UltrasoundMedBiol J1 - UMB* 1995;21:969-79.
192. Mesiwala AH, Farrell L, Wenzel HJ, *et al.* High-intensity focused ultrasound selectively disrupts the blood-brain barrier in vivo. *Ultrasound Med Biol* 2002;28:389-400.
193. Vykhodtseva NI, Sorrentino V, Jolesz FA, Bronson RT, Hynynen K. MRI detection of the thermal effects of focused ultrasound on the brain. *Ultrasound Med Biol* 2000;26:871-80.
194. Hynynen K, McDannold N, Vykhodtseva N, *et al.* Focal disruption of the blood-brain barrier due to 260-kHz ultrasound bursts: a method for molecular imaging and targeted drug delivery. *J Neurosurg* 2006;105:445-54.
195. Hynynen K, McDannold N, Sheikov NA, Jolesz FA, Vykhodtseva N. Local and reversible blood-brain barrier disruption by noninvasive focused ultrasound at frequencies suitable for trans-skull sonications. *Neuroimage* 2005;24:12-20.
196. McDannold N, Vykhodtseva N, Hynynen K. Blood-brain barrier disruption induced by focused ultrasound and circulating preformed microbubbles appears to be characterized by the mechanical index. *Ultrasound Med Biol* 2008;34:834-40.
197. Hynynen K, McDannold N, Josphson L, Vykhodtseva N, Weisleder R, Jolesz FA. Noninvasive MRI-guided focal opening of the blood brain barrier: Demonstration of large particle penetration. *Proceedings of the Tenth Meeting of the International Society for Magnetic Resonance in MedicineHonolulu, HI; 2002; 2002.* p. 332.
198. McDannold N, Vykhodtseva N, Raymond S, Jolesz FA, Hynynen K. MRI-guided targeted blood-brain barrier disruption with focused ultrasound: histological findings in rabbits. *Ultrasound Med Biol* 2005;31:1527-37.
199. McDannold N, Vykhodtseva N, Hynynen K. Effects of acoustic parameters and ultrasound contrast agent dose on focused-ultrasound induced blood-brain barrier disruption. *Ultrasound Med Biol* 2008;34:930-7.
200. McDannold N, Vykhodtseva N, Hynynen K. Targeted disruption of the blood-brain barrier with focused ultrasound: association with cavitation activity. *Phys Med Biol* 2006;51:793-807.

201. Yang FY, Fu WM, Yang RS, Liou HC, Kang KH, Lin WL. Quantitative evaluation of focused ultrasound with a contrast agent on blood-brain barrier disruption. *Ultrasound Med Biol* 2007;33:1421-7.
202. Nyborg WL, Carson PL, Carstensen EL, *et al*. Exposure criteria for medical diagnostic ultrasound: II. Criteria based on all known mechanisms (NCRP Report No. 140). Bethesda, Maryland: National Council on Radiation Protection and Measurements; 2002.
203. Crum LA, Hansen GM. Growth of air bubbles in tissue by rectified diffusion. *Phys Med Biol* 1982;27:413-7.
204. Edmonds PD, Sancier KM. Evidence for free radical production by ultrasonic cavitation in biological media. *Ultrasound Med Biol* 1983;9:635-9.
205. Apfel RE. Acoustic cavitation: a possible consequence of biomedical uses of ultrasound. *Br J Cancer Suppl* 1982;45:140-6.
206. Flynn HG. Generation of transient cavities in liquids by microsecond pulses of ultrasound. *J Acoust Soc Am* 1982;72:1926-32.
207. Crum LA, Roy RA, Dinno MA, *et al*. Acoustic cavitation produced by microsecond pulses of ultrasound: a discussion of some selected results. *J Acoust Soc Am* 1992;91:1113-9.
208. Miller DL. Particle gathering and microstreaming near ultrasonically activated gas-filled micropores. *J Acoust Soc Am* 1988;84:1378-87.
209. Dayton P, Klibanov A, Brandenburger G, Ferrara K. Acoustic radiation force in vivo: a mechanism to assist targeting of microbubbles. *Ultrasound Med Biol* 1999;25:1195-201.
210. Sheikov N, McDannold N, Jolesz F, Zhang YZ, Tam K, Hynynen K. Brain arterioles show more active vesicular transport of blood-borne tracer molecules than capillaries and venules after focused ultrasound-evoked opening of the blood-brain barrier. *Ultrasound Med Biol* 2006;32:1399-409.
211. Bristol IJ, Buchholz TA. Inflammatory breast cancer: current concepts in local management. *Breast Dis* 2005;22:75-83.
212. Thigpen JT, Aghajanian CA, Alberts DS, *et al*. Role of pegylated liposomal doxorubicin in ovarian cancer. *Gynecol Oncol* 2005;96:10-8.
213. Hawkins DS, Arndt CA. Pattern of disease recurrence and prognostic factors in patients with osteosarcoma treated with contemporary chemotherapy. *Cancer* 2003;98:2447-56.
214. Ardizzoni A, Tjan-Heijnen VC, Postmus PE, *et al*. Standard versus intensified chemotherapy with granulocyte colony-stimulating factor support in small-cell lung cancer: a prospective European Organization for Research and Treatment of Cancer-Lung Cancer Group Phase III Trial-08923. *J Clin Oncol* 2002;20:3947-55.
215. Gilliam LK, Kohn AD, Lalani T, *et al*. Capecitabine therapy for refractory metastatic thyroid carcinoma: a case series. *Thyroid* 2006;16:801-10.
216. Wang X, Pang L, Feng J. A phase II study of etoposide, doxorubicin, and carboplatin in the treatment of advanced gastric cancer. *Am J Clin Oncol* 2002;25:71-5.
217. Child JA, Morgan GJ, Davies FE, *et al*. High-dose chemotherapy with hematopoietic stem-cell rescue for multiple myeloma. *N Engl J Med* 2003;348:1875-83.

218. Laskar S, Gupta T, Vimal S, *et al.* Consolidation radiation after complete remission in Hodgkin's disease following six cycles of doxorubicin, bleomycin, vinblastine, and dacarbazine chemotherapy: is there a need? *J Clin Oncol* 2004;22:62-8.
219. Palmieri C, Treibel T, Large O, Bower M. AIDS-related non-Hodgkin's lymphoma in the first decade of highly active antiretroviral therapy. *Qjm* 2006;99:811-26.
220. Grobmyer SR, Maki RG, Demetri GD, *et al.* Neo-adjuvant chemotherapy for primary high-grade extremity soft tissue sarcoma. *Ann Oncol* 2004;15:1667-72.
221. Benjamin RS, Wiernik PH, Bachur NR. Adriamycin chemotherapy--efficacy, safety, and pharmacologic basis of an intermittent single high-dosage schedule. *Cancer* 1974;33:19-27.
222. Cummings J, McArdle CS. Studies on the in vivo disposition of adriamycin in human tumours which exhibit different responses to the drug. *Br J Cancer* 1986;53:835-8.
223. Stan AC, Casares S, Radu D, Walter GF, Brumeanu TD. Doxorubicin-induced cell death in highly invasive human gliomas. *Anticancer Res* 1999;19:941-50.
224. Aubel-Sadron G, Londos-Gagliardi D. Daunorubicin and doxorubicin, anthracycline antibiotics, a physicochemical and biological review. *Biochimie* 1984;66:333-52.
225. Working PK, Dayan AD. Pharmacological-toxicological expert report. CAELYX. (Stealth liposomal doxorubicin HCl). *Hum Exp Toxicol* 1996;15:751-85.
226. Gewirtz DA. A critical evaluation of the mechanisms of action proposed for the antitumor effects of the anthracycline antibiotics adriamycin and daunorubicin. *Biochem Pharmacol* 1999;57:727-41.
227. Bachur NR, Gee MV, Friedman RD. Nuclear catalyzed antibiotic free radical formation. *Cancer Res* 1982;42:1078-81.
228. Sinha BK. Free radicals in anticancer drug pharmacology. *Chem Biol Interact* 1989;69:293-317.
229. Ferreira AL, Salvadori DM, Nascimento MC, *et al.* Tomato-oleoresin supplement prevents doxorubicin-induced cardiac myocyte oxidative DNA damage in rats. *Mutat Res* 2007;631:26-35.
230. Tokarska-Schlattner M, Zaugg M, Zuppinger C, Wallimann T, Schlattner U. New insights into doxorubicin-induced cardiotoxicity: the critical role of cellular energetics. *J Mol Cell Cardiol* 2006;41:389-405.
231. Kalyanaraman B, Morehouse KM, Mason RP. An electron paramagnetic resonance study of the interactions between the adriamycin semiquinone, hydrogen peroxide, iron-chelators, and radical scavengers. *Arch Biochem Biophys* 1991;286:164-70.
232. Park JW. Liposome-based drug delivery in breast cancer treatment. *Breast Cancer Res* 2002;4:95-9.
233. Gabizon A, Martin F. Polyethylene glycol-coated (pegylated) liposomal doxorubicin. Rationale for use in solid tumours. *Drugs* 1997;54 Suppl 4:15-21.
234. Karukstis KK, Thompson EH, Whiles JA, Rosenfeld RJ. Deciphering the fluorescence signature of daunomycin and doxorubicin. *Biophys Chem* 1998;73:249-63.
235. Hodgson E, Bend JR, Philpot RM, editors. *Reviews in biochemical toxicology*. New York; Elsevier Biomedical; 1984.

236. Stewart HF. Ultrasonic Measurement Techniques and Equipment Output Levels. In: Repacholi MH, Benwell DA, editors. *Essentials of Medical Ultrasound: A Practical Introduction to the Principles, Techniques, and Biomedical Applications*. Clifton, NJ: Humana Press; 1982. p. 77-116.
237. Goss SA, Frizzell LA, Dunn F. Ultrasonic absorption and attenuation in mammalian tissues. *UltrasoundMedBiol J1 - UMB* 1979;5:181-6.
238. Htun T. A negative deviation from stern-volmer equation in fluorescence quenching. *J Fluoresc* 2004;14:217-22.
239. Kaplan EL, Meier P. Nonparametric estimation from incomplete observations. *J Am Stat Assoc* 1958;53:457-81.
240. Bland JM, Altman DG. Multiple significance tests: the Bonferroni method. *BMJ* 1995;310:170.
241. Runge VM, Clanton JA, Herzer WA, *et al.* Intravascular contrast agents suitable for magnetic resonance imaging. *Radiology* 1984;153:171-6.
242. Dietrich WD, Prado R, Halley M, Watson BD. Microvascular and neuronal consequences of common carotid artery thrombosis and platelet embolization in rats. *J Neuropathol Exp Neurol* 1993;52:351-60.
243. Kaur C, Sivakumar V, Zhang Y, Ling EA. Hypoxia-induced astrocytic reaction and increased vascular permeability in the rat cerebellum. *Glia* 2006;54:826-39.
244. Kondo A, Inoue T, Nagara H, Tateishi J, Fukui M. Neurotoxicity of adriamycin passed through the transiently disrupted blood-brain barrier by mannitol in the rat brain. *Brain Res* 1987;412:73-83.
245. Neuwelt EA, Pagel M, Barnett P, Glassberg M, Frenkel EP. Pharmacology and toxicity of intracarotid adriamycin administration following osmotic blood-brain barrier modification. *Cancer Res* 1981;41:4466-70.
246. Pardridge WM. Blood-brain barrier drug targeting: the future of brain drug development. *Mol Interv* 2003;3:90-105, 51.
247. Voulgaris S, Partheni M, Karamouzis M, Dimopoulos P, Papadakis N, Kalofonos HP. Intratumoral doxorubicin in patients with malignant brain gliomas. *Am J Clin Oncol* 2002;25:60-4.
248. Fine HA, Dear KB, Loeffler JS, Black PM, Canellos GP. Meta-analysis of radiation therapy with and without adjuvant chemotherapy for malignant gliomas in adults. *Cancer* 1993;71:2585-97.
249. DeAngelis LM, Burger PC, Green SB, Cairncross JG. Malignant glioma: who benefits from adjuvant chemotherapy? *Ann Neurol* 1998;44:691-5.
250. Cairncross JG, Ueki K, Zlatescu MC, *et al.* Specific genetic predictors of chemotherapeutic response and survival in patients with anaplastic oligodendrogliomas. *J Natl Cancer Inst* 1998;90:1473-9.
251. van den Bent MJ, Hegi ME, Stupp R. Recent developments in the use of chemotherapy in brain tumours. *Eur J Cancer* 2006;42:582-8.
252. Caraglia M, Addeo R, Costanzo R, *et al.* Phase II study of temozolomide plus pegylated liposomal doxorubicin in the treatment of brain metastases from solid tumours. *Cancer Chemother Pharmacol* 2006;57:34-9.
253. Jain RK. Barriers to drug delivery in solid tumors. *Sci Am* 1994;271:58-65.

254. Tofts PS. Optimal detection of blood-brain barrier defects with Gd-DTPA MRI- the influences of delayed imaging and optimised repetition time. *MagnResonImaging* 1996;14:373-80.
255. Tofts PS. Modeling tracer kinetics in dynamic Gd-DTPA MR imaging. *J Magn Reson Imaging* 1997;7:91-101.
256. Tofts PS. Standardisation and optimisation of magnetic resonance techniques for multicentre studies. *J Neurol Neurosurg Psychiatry* 1998;64 Suppl 1:S37-43.
257. Tofts PS, Brix G, Buckley DL, *et al.* Estimating kinetic parameters from dynamic contrast-enhanced T(1)-weighted MRI of a diffusable tracer: standardized quantities and symbols. *J Magn Reson Imaging* 1999;10:223-32.
258. Tofts PS, Kermode AG. Measurement of the blood-brain barrier permeability and leakage space using dynamic MR imaging. 1. Fundamental concepts. *Magn Reson Med* 1991;17:357-67.
259. St Lawrence KS, Lee TY. An adiabatic approximation to the tissue homogeneity model for water exchange in the brain: I. Theoretical derivation. *J Cereb Blood Flow Metab* 1998;18:1365-77.
260. St Lawrence KS, Lee TY. An adiabatic approximation to the tissue homogeneity model for water exchange in the brain: II. Experimental validation. *J Cereb Blood Flow Metab* 1998;18:1378-85.
261. Brubaker LM, Smith JK, Lee YZ, Lin W, Castillo M. Hemodynamic and permeability changes in posterior reversible encephalopathy syndrome measured by dynamic susceptibility perfusion-weighted MR imaging. *AJNR Am J Neuroradiol* 2005;26:825-30.
262. Cao Y, Shen Z, Chenevert TL, Ewing JR. Estimate of vascular permeability and cerebral blood volume using Gd-DTPA contrast enhancement and dynamic T2*-weighted MRI. *J Magn Reson Imaging* 2006;24:288-96.
263. Law M, Young R, Babb J, *et al.* Comparing perfusion metrics obtained from a single compartment versus pharmacokinetic modeling methods using dynamic susceptibility contrast-enhanced perfusion MR imaging with glioma grade. *AJNR Am J Neuroradiol* 2006;27:1975-82.
264. Kreutzberg GW. Microglia: a sensor for pathological events in the CNS. *Trends Neurosci* 1996;19:312-8.
265. Hanisch UK, Kettenmann H. Microglia: active sensor and versatile effector cells in the normal and pathologic brain. *Nat Neurosci* 2007;10:1387-94.
266. Abbott NJ. Inflammatory mediators and modulation of blood-brain barrier permeability. *Cell Mol Neurobiol* 2000;20:131-47.
267. Romero-Sandoval EA, Horvath RJ, DeLeo JA. Neuroimmune interactions and pain: focus on glial-modulating targets. *Curr Opin Investig Drugs* 2008;9:726-34.
268. Arnhold S, Antoine D, Blaser H, Bloch W, Andressen C, Addicks K. Nitric oxide decreases microvascular permeability in bradykinin stimulated and nonstimulated conditions. *J Cardiovasc Pharmacol* 1999;33:938-47.
269. Hickey WF, Kimura H. Perivascular microglial cells of the CNS are bone marrow-derived and present antigen in vivo. *Science* 1988;239:290-2.